eman ta zabal zazu

Universidad del País Vasco
Euskal Herriko Unibertsitatea

Complex systems in quantum technologies

Antonio Mezzacapo

Supervisor:
Prof. Enrique Solano

Departamento de Química Física
Facultad de Ciencia y Tecnología
Universidad del País Vasco UPV/EHU

Leioa, May 2015

(cc)2015 Antonio Mezzacapo (cc by-nc 4.0)

All of science is nothing more than the refinement of everyday thinking.

Albert Einstein

Abstract

Controlled quantum platforms have become in the last years a major tool for the implementation of quantum information protocols of increasing complexity. At the same time, the technology needed to control and scale up these devices is becoming more demanding, and the physics behind this progress is limited by deep fundamental constraints. Some decades ago, the experimental difficulties to build better quantum platforms, on one hand, and the intellectual efforts to develop more efficient and sophisticated quantum protocols, on the other hand, were two roads that did not cross frequently.

Nowadays, we have realized that a profound understanding of both the current technology and fundamental physical processes has to be combined with an increased flexibility in designing quantum information processes. In this context, quantum simulations play a special role: they have been proposed as a first application of quantum computers, and it is believed that they will soon bring new results that are unaccessible by classical computers.

In this Thesis, we propose a series of quantum information and simulation protocols, analyzing their feasibility using current technology, in both trapped-ion and circuit quantum electrodynamics platforms. We find that the proposed protocols have to be adapted to the advantages and drawbacks of specific platforms. For example, we prove that a protected qubit, based on a dual representation of the topological fermionic chain, can be encoded in an ion-trap system due to its specific properties. We analyze the quantum simulation of fermions, finding an increased efficiency due to collective gates that are realizable with ion-trap technology. Within this spirit, we benchmark the possibilities of circuit quantum electrodynamics setups in hosting quantum simulations of spins, fermionic and fermionic-bosonic systems. Finally, we extend these concepts to the quantum simulation of classical dynamical systems, finding that a simulation of lattice-Boltzmann dynamics can be encoded in coupled pseudospin-bosonic systems. These are the first steps to unravel the unexplored area of simulations of fluid dynamics on a quantum computer.

We believe that this Thesis will contribute to enforce the connections between complex systems in quantum information and their direct experimental implementations in quantum technologies.

Resumen

En esta Tesis, se considera la realización práctica de varios protocolos de información cuántica en diferentes plataformas cuánticas, considerando principalmente experimentos basados en iones atrapados y arquitecturas superconductoras. Los límites de tiempos de coherencia, control cuántico, fuentes de errores, y los tipos de interacciones cuánticas son analizados en cada plataforma cuántica específica. Las distintas ideas presentadas en el texto son propuestas para plataforma experimentales específicas, explotando cada vez los recursos disponibles.

Creemos que los resultados aquí obtenidos servirán para fortalecer la conexión entre la física teórica y experimental, orientada a la información cuántica, cuando se trata de aplicaciones prácticas. Se espera que el trabajo aquí realizado contribuya, en un futuro próximo, a traer nuevos conocimientos en el campo de la materia condensada, física de alta energía, química cuántica y dinámica de fluidos clásicos, dependiendo de como como las plataformas cuánticas disponibles vayan escalando en términos de tamaño y de control.

En el Capítulo 2, hemos demostrado que cadenas de iones atrapados pueden albergar un qubit protegido, basado en una representación dual de una cadena fermiónica topológica. Nos enfrentamos al problema desde un enfoque de primeros principios, preguntándonos cual es el conjunto mínimo de requisitos experimentales para construir, en un sistema de iones atrapados, un qubit lógico, incluyendo con control cuántico, y con tiempos de coherencia superiores a las de un qubit físico. Hemos predicho que el qubit propuesto puede superar la coherencia estándar de los qubit basados en iones atrapados en más de un orden de magnitud, produciendo una memoria cuántica eficiente. Rotaciones locales lógicas sobre el qubit se pueden realizar por medio de interacciones globales y locales sobre los iones. Por otra parte, una interfaz cuántica con estados

fotónicos se puede implementar, para la realización de puertas de dos qubits entre diferentes qubits protegidos. Estos qubits de paridad representan un primer ejemplo práctico, realizable con los recursos mínimos cuántica, de un qubit lógico con puertas lógicas asociadas.

En los Capítulos 3, 4 y 5 hemos desarrollado un protocolo para la simulación cuántica digital de sistemas acoplados de fermiones y bosones, en plataformas de iones atrapados. Este protocolo ha sido aplicado primero a la simulación de modelos fermionicos interactuantes. Hemos propuesto que las interacciones colectivas entre un conjunto de muchos iones pueden implementar interacciones fermionicas eficientemente, hasta altos ordenes en las interacciones. Estas puertas colectivas también dan cuenta de una mayor eficiencia en la simulación de sistemas fermiónicos en dos y tres dimensiones, en comparación con los protocolos de simulación basados en puertas de dos qubits locales. La dinámica total del modelo fermiónico simulado se recupera a continuación por medio de una digitalización y mapeo de Jordan-Wigner. Con la tecnología de iones atrapados actuales, más de 100 puertas se han realizado en un solo experimento. De hecho, sin corrección de errores, uno esperaría la realización de cientos de puertas en tiempos más cortos que el tiempo de decoherencia de 30 ms. El simulador puede ser útil en la realización de una amplia gama de cálculos de la materia condensada, incluidos los relacionados con la interacción de muchos cuerpos como la de los modelos de Kondo, Fermi-Hubbard, o Fröhlich. Además, las simulaciones cuánticas nos permitirán reproducir la dinámica completa de estos sistemas, evitando aproximaciones de campo medio como Hartree-Fock para simplificar las interacciones no lineales. La velocidad a la que los sistemas de ion-trap realmente mejorar, combinada con el aumento de la eficiencia de nuestra propuesta, hacen que estos resultados son relevantes, por ejemplo, para las simulaciones cuánticas de sistemas de materia condensada, o para sondear la física de alta energía en no regímenes non perturbativos.

En el Capítulo 4, hemos extendido el protocolo simulación presentada en el Capítulo 3 a sistemas acoplados de bosónes y fermióne, explicando en detalle la forma en que se puede realizar el modelo de Holstein. La simulación de estos sistemas tiene una mayor complejidad con respecto a los sistemas puramente fermionicos, debido al crecimiento rápido del espacio de Hilbert, con el crecimiento de la población bosonica. Vale la pena mencionar que nuestra simulación cuántica superaría los límites de los ordenadores clásicos solo con 10 iones y 5 fonones por ion. Esto permitirías estudiar la formación de polarones en un régimen de parámetros muy amplio. Los futuros experimentos que involucran 20 a 30 iones permitirán abordar el estudio de dinámica más complejas, incluyendo correlaciones electrón-electrón mediadas por fonones.

En el Capítulo 5, utilizando el modelo desarrollado para los sistemas fermiónicos, hemos propuesto un protocolo de simulación cuántica híbrido para la química cuántica, realizable con iones atrapados. Este paradigma en las simulaciones cuánticas tiene varias ventajas: una simulación eficiente electrónica, la posibilidad de simular interacciones entre grados libres electrónicos y vibracionales, y la escalabilidad creciente que ofrecen los sistemas de iones atrapados. Este enfoque para la solución de problemas de química cuántica pretende combinar lo mejor de la computación clásica y cuántica, para una mayor eficiencia computacional.

En los Capítulos 6, 7 y 8, nos hemos ocupado de los sistemas de circuitos superconductores. A través de circuitos superconductores se pueden realizar átomos artificiales, que pueden ser acoplados a los resonadores de microondas. Un acoplamiento dispersivo de los resonadores permite realizar lectura de qubits superconductores. Además, puertas qubit individuales se pueden realizar con las señales de microondas enviados a través de los resonadores. Configuraciones con qubit transmon estándar acoplados a resonadores de microondas pueden tener tiempos de coherencia de decenas de microsegundos, mientras que las puertas cuánticas pueden tener tiempos de ejecución de unos pocos a decenas de nanosegundos, en el caso de las rotaciones individuales, y decenas a cientos de nanosegundos para operaciones entre dos qubits.

En el Capítulo 6, hemos propuesto una simulación cuántica digital de los modelos de cadenas de espines en los circuitos superconductores. Hemos considerado modelos prototípicos como Heisenberg y Ising con frustración. Hemos demostrado la viabilidad de la simulación con la tecnología de transmon qubits acoplados a resonadores de microondas. Los tres elementos básicos de los cuales están hechos los átomos artificiales superconductivos, es decir, inductancias, capacitancias y uniones Josephson, pueden ser fabricados y utilizados en diferentes regímenes de parámetros para obtener diferentes comportamientos. Los tipos básicos de qubits superconductores son qubit de carga, de flujo y de fase. Una modificación de las capacidades en el diseño original de los qubits de carga ha originado los transmon qubits, que utilizamos en larga parte de esta Tesis.

Los modelos propuestos se han realizado por el *Quantum Device Lab* del Prof. Andreas Wallraff en la universidad ETH Zürich en Suiza. Estos protocolos pueden extenderse a modelos de espines entre muchos qubits, hasta la simulación cuántica universal de la dinámica de espines.

En el Capítulo 7, hemos demostrado que una plataforma hecha de qubits de tres islas superconductoras, con acoplamiento ajustable a una guía de microondas coplanario, puede generar de forma efectiva puertas colectivas e interacciones de muchos cuerpos entre los qubits. Hemos mostrado que actuando dinámicamente con flujos magneticos sobre dos SQUIDs presentes en los dispositivos de tres islas, es posible llevar a cabo las transiciones *red* y *blue sidebands* simultáneas sobre muchos qubits. Esto conduce a las puertas de entrelazamiento colectivas que se pueden utilizar para obtener de manera eficiente los operadores de muchas partículas. Se demuestra que el tercer nivel de los qubits se puede descartar de la dinámica. Validamos la propuesta con simulaciones numéricas de la dinámica del sistema, teniendo en cuenta un modelo de decoherencia realista. Estas interacciones, similares a aquellas analizadas en el Capítulo 3 para sistemas de iones atrapados, pueden utilizarse para implementar códigos topológicos y simular eficientemente dinámica fermionica.

En el Capítulo 8, hemos demostrado que la dinámica de los modelos cuánticos Rabi y Dicke pueden ser codificados en circuitos superconductores utilizando tecnicas digital-analógicas. Mostramos cómo las contribuciones de rotación y contra-rotación de un modelo Jaynes-Cummings pueden simular digitalmente un modelo de Rabi. En concreto, mediante la aplicación intercalada de rotaciónes locales y interaciones de los qubits con un modo bosonico, la dinámica de los modelos cuánticos Rabi y Dicke pueden ser simulada para todos los regímenes de parámetros con error despreciable. Por último, se muestra cómo una dinámica relativista de Dirac se puede recuperar en el límite donde se cancela la frecuencia del modo bosonico. Estas simulaciones cuánticas contribuirán a la observación de la dinámica cuántica de estos modelos, en regímenes no accesibles en los experimentos actuales.

En la última parte de esta Tesis hemos analizado simulaciones cuánticas para los sistemas clásicos. En el Capítulo 9, se ha desarrollado un protocolo para reproducir la dinámica de los fenómenos de transporte de fluidos en un experimento de mecánica cuántica, utilizando pseudo espines acoplados a modos bosónicos, que se pueden implementar en diferentes plataformas cuántica. Nos acercamos a la simulación de dinámica de fluidos utilizando un simulador cuántico, adecuado para la codificación de problemas de dinámica de fluidos dentro de un formalismo cinético de Boltzmann. Este simulador cuántico se obtiene por la explotación de las analogías entre la ecuación de Dirac y las ecuaciones discretas de Boltzmann. Se muestra que tanto la transmisión como la colisión de los procesos de dinámica de Boltzmann pueden implementarse con operaciones cuántica controladas, utilizando un protocolo cuántico con un qubit auxiliar para codificar los procesos de dispersión no unitarios. El simulador propuesto es realizable en plataformas cuántica controladas, como los ordenadores cuánticos de iones atrapados o procesadores basados en superconductores. Esta propuesta abre el camino a la simulación cuántica y la recuperación de la dinámica de fluidos clásica complejos en los sistemas cuánticos controladas. Evoluciones de este trabajo incluirán la posibilidad de simular el comportamiento no lineal, y modelos mas complejos de dinámica de fluidos.

En las Apéndices, se presenta el material complementario a los Capítulos, que ayuda a una mejor comprensión de los resultados que se muestran en esta Tesis.

Creemos que los resultados científicos presentados en esta Tesis representan una contribución importante para el éxito y el desarrollo de la tecnología cuántica en un futuro próximo.

Acknowledgements

I would like first to thank my PhD supervisor Prof. Enrique Solano, who has guided me into the scientific community and advised me on how to pursue original research. His guidance has been invaluable for the work done in this Thesis and for all the great scientific and human experiences accumulated during my PhD studies.

I would also like to thank all members of the QUTIS research group, for all the great time spent together, both inside and outside the UPV/EHU campus. Special thanks go to Dr. Lucas Lamata, who has been co-supervising and guiding me directly through most of the work done in this Thesis.

I have also had the pleasure to interact and collaborate with several scientists from other institutions. Among them, I would like to mention Prof. Alán Aspuru-Guzik from Harvard University, for inviting me to Cambridge, MA, together with his group members Man-Hong Yung and Jarrod McClean. Warm thanks go to Prof. Andreas Wallraff and Dr. Stefan Filipp from ETH Zürich, for the great work done together on both theoretical and experimental sides; it has been a real pleasure to interact with them, and they have been patient enough to introduce me to the details of their experiments. Many thanks also go to all people at ETH Zürich, particularly to Yves Salathé and Dr. Mintu Mondal, for all the great time spent together to design the quantum simulation experiments. I would like to express my gratitude to Prof. Leonardo DiCarlo at TU Delft, together with his group members Dr. Nathan Langford and Marios Kounalakis, for the nice discussions on implementations of some of the results of this Thesis. Many thanks go also to Prof. Miguel Ángel Martín-Delgado for inviting me at the Complutense University in Madrid. It has been a pleasure to learn from his great knowledge; acknowledgments go also to Dr. Markus Müller, with whom I shared enlightening conversations. I would like to thank again my M. Sc. advisors Prof. Arturo Tagliacozzo and Dr. Procolo Lucignano from Naples University, for helping me producing relevant scientific material out of some of the results of my Master Thesis. Special thanks go also to Dr. Sauro Succi, at CNR in Rome and Harvard University, for influencing me with his energy and great passion for research, and for introducing me to the physics of fluid dynamics. I acknowledge discussions with Prof. Massimiliano Di Ventra from University of San Diego, it has been a pleasure to learn from his ideas. I thank Prof. Steven Girvin at Yale University for inviting me in New Haven and giving me the opportunity to discuss physics with him, also

enjoying a visit to the labs of Prof. Michel Devoret and Prof. Robert Shoelkopf. I thank Dr. Luigi Frunzio for the kind invitation and the nice conversations we had together. Warm thanks go to Prof. William Oliver at Massachusetts Institute of Technology, for showing me his interesting projects carried in his laboratory. Special thanks go to Dr. Jay Gambetta, from IBM T. J. Watson Research Center, for introducing me to top-class research in private companies. I have profited hugely from the hospitality and enlightening conversations with Prof. Frank Wilhelm-Mauch at Saarbrücken University, together with his group members, especially Dr. Bruno Taketani and Dr. Daniel Egger.

A warm thanks goes to my close friends and my family. Without their support I would not have make it through: I owe them things that cannot be given back.

Contents

Abstract **iv**

Acknowledgements **v**

List of Figures **xi**

List of publications **xvii**

1 Introduction **1**
- 1.1 Complexity in quantum technologies . . . 1
  - 1.1.1 Trapped ions . . . 2
  - 1.1.2 Circuit quantum electrodynamics . . . 4
- 1.2 Quantum simulations . . . 5
  - 1.2.1 Analog quantum simulators . . . 5
  - 1.2.2 Digital quantum simulators . . . 6
- 1.3 This Thesis . . . 7

I Complex systems in trapped ions **11**

2 Protected Majorana parity qubits in trapped ions **13**
- 2.1 Introduction . . . 13
- 2.2 Trapped-ion implementation . . . 14
- 2.3 Quantum Interface . . . 17
- 2.4 Local operations and measurement . . . 17
- 2.5 Errors and decoherence protection . . . 18

3 Interacting fermion lattice models in trapped ions **21**
- 3.1 Introduction . . . 21
- 3.2 Digital quantum simulation of fermionic dynamics . . . 22
- 3.3 Fermionic models in condensed matter . . . 24
- 3.4 The n-dimensional case . . . 25
- 3.5 Numerical simulations . . . 26
- 3.6 Analysis of Trotter errors . . . 28

4 Quantum simulation of the Holstein model **31**
4.1 Introduction 31
4.2 Trotter decomposition 32
4.3 Proposal for ion-trap systems 34
4.4 Digital quantum simulation analysis 37
4.5 Numerical simulations 39

5 Quantum-classical simulator for quantum chemistry **43**
5.1 Introduction 43
5.2 Trapped ions for quantum chemistry 46
5.3 Quantum-assisted optimization 48
5.4 Unitary coupled-cluster (UCC) ansatz 48
5.5 Implementation issues of UCC with trapped-ions 50
5.6 Measurement of arbitrarily-nonlocal spin operators 50
5.7 Numerical analysis 51

II Complex systems in superconducting circuits **55**

6 Interacting spin models using superconducting circuits **57**
6.1 Introduction 57
6.2 Heisenberg interaction with digital methods 59
6.3 Ising interaction with digital methods 62
6.4 Feasibility in current architectures 63

7 Collective gates and many-body interactions in circuit QED **67**
7.1 Introduction 67
7.2 Three-island devices for many-body interactions 68
7.3 Collective dynamics 69
7.4 Analysis of parameters of circuit QED 73

8 Quantum Rabi and Dicke models in superconducting circuits **77**
8.1 Introduction 77
8.2 Digital-analog decomposition of the Rabi model 79
8.3 Circuit QED implementation 81
8.4 Numerical analysis 81
8.5 Dicke model and furher developments 83

III Quantum simulations of complex classical systems **85**

9 A quantum simulator for fluid dynamics **87**
9.1 Introduction 87
9.2 Lattice Boltzmann equation 88
9.3 Streaming and collision dynamics in a quantum simulator 90
9.4 Four-speed lattice 93

IV Conclusions **97**

V Appendices **103**

A An upper bound for the norm of the Holstein Hamiltonian **105**

B Estimation of non-nearest-neighbor coupling strenght **107**

C Derivation of effective models for collective gates **109**

D Many-body operators **113**

Bibliography **115**

List of Figures

2.1 (a) Array of 1D ion crystals inside K optical cavities for the quantum interface between a multiqubit entangled photonic state and a MF qubit multipartite state. The shaded region denotes a single MF qubit. (b) Fidelity loss $1 - F = 1 - |\langle\Psi_0|\psi(t)\rangle|^2$ for the evolved state $|\psi(t)\rangle$ from the initial state $|\Psi_0^{\text{init}}\rangle$ using the adiabatic transfer protocol with H_s in Eq. (2.3), for $N = 3$. The diabatic error for the ideal protocol (black solid line) is plotted against the diabatic error (red dotted line), obtained including a constant magnetic field in the Z direction of magnitude $\delta h_z = 10^{-3}J$ [14], a 1% error on the relative coupling magnitude J_{12}/J_{23} and a NNN coupling $J_{13} = J_{12}/8$ 16

2.2 (a) Energy splitting Γ between $|\Psi_0\rangle$ and $|\Psi_1\rangle$ as a function of number of sites N, in units of $J = 1$, computed numerically for $\delta h_z = 10^{-3}J$ and 1% error on the relative magnitude J_{12}/J_{23}. (b) Survival probability $F = |\langle\Psi_0|\psi(t)\rangle|^2$ for the evolved state $|\psi(t)\rangle$ from $|\Psi_0\rangle$ under the dynamics of Hamiltonian (2.3) (with $h_z = 0$) (solid) or without it, i.e. free evolution of the state (dashed), plus constant local operators of modulus $10^{-3}J$, proportional to σ_i^z, for $N = 3$. The topological Hamiltonian provides protection against the σ_i^z noise. 19

3.1 (a) Mapping of a fermionic Hamiltonian onto an ion string. The couplings between fermions 1 and 4 (resp., 1 and 10) are nonlocal when applying the Jordan-Wigner transformation. (b) Efficient mapping of the tunneling coupling $b_1^\dagger b_{10} + b_{10}^\dagger b_1$ in trapped ions. This highly nonlocal coupling can be implemented with Mølmer-Sørensen gates (dark blue and green), local $\exp(i\phi'\sigma_2^y)$ gates (red), $\exp[\pm i(\pi/4)\sum_i \sigma_i^y]$ (yellow) and $\exp[\pm i(\pi/4)\sum_i \sigma_i^x]$ (cyan) gates. 26

3.2 (a) $\langle b_{2\downarrow}^\dagger b_{2\downarrow}\rangle(t)$ (dashed, blue), and $\langle b_{3\uparrow}^\dagger b_{3\uparrow}\rangle(t)$ (solid, red) as a function of Ut, for a number of Trotter steps $n_T = 15$, and (b) fidelity $|\langle\psi(t_F)|\psi(t_F)_T\rangle|^2$ as a function of n_T, for $Ut_F = 10$, where $|\psi(t)\rangle$ is the state evolved with exact diagonalization, and $|\psi(t)_T\rangle$ is the Trotter-evolved state, for $|\psi(0)\rangle = |\psi_T(0)\rangle = b_{1\uparrow}^\dagger b_{1\downarrow}^\dagger|0\rangle$, for $|w|/U = 0.1$. (c) $\langle b_{2\downarrow}^\dagger b_{2\downarrow}\rangle(t)$ (dashed, blue), and $\langle b_{3\uparrow}^\dagger b_{3\uparrow}\rangle(t)$ (solid, red), for $n_T = 15$, and (d) fidelity $|\langle\psi(t_F)|\psi(t_F)_T\rangle|^2$, for $Ut_F = 2.5$, where $|\psi(t)\rangle$ is the state evolved with exact diagonalization, and $|\psi(t)_T\rangle$ is the Trotter-evolved state, for $|\psi(0)\rangle = |\psi_T(0)\rangle = b_{1\uparrow}^\dagger b_{1\downarrow}^\dagger|0\rangle$, for $|w|/U = 4$. In (a) and (c), the lines are obtained with exact diagonalization and the dots with Trotter expansion. 27

3.3 We plot $\langle b^\dagger_{2\downarrow} b_{2\downarrow}\rangle(t)$ (dashed, blue), and $\langle b^\dagger_{3\uparrow} b_{3\uparrow}\rangle(t)$ (solid, red) as a function of Ut, for $|\psi(0)\rangle = |\psi_T(0)\rangle = b^\dagger_{1\uparrow} b^\dagger_{1\downarrow}|0\rangle$, $|w|/U = 4$, and a number of Trotter steps $n_T = 30$ (a), 45 (b), and 60 (c). In (a), (b), and (c) the lines are obtained with exact diagonalization and the dots are obtained with Trotter expansion. We also plot (d) the fidelity $|\langle\psi(t_F)|\psi(t_F)_T\rangle|^2$ as a function of n_T, for $Ut_F = 2.5$, where $|\psi(t)\rangle$ is the state evolved with exact diagonalization, and $|\psi(t)_T\rangle$ is the Trotter-evolved state, for $|\psi(0)\rangle = |\psi_T(0)\rangle = b^\dagger_{1\uparrow} b^\dagger_{1\downarrow}|0\rangle$, and for $|w|/U = 4$. We show the numerical results with Trotter (dots) and a fit to the function $1 - C/n_T^2$ (line), where C is a free parameter. . . . 29

4.1 (a) Behavior of the fidelity loss $1 - F(t) = 1 - |\langle\Psi_E(t)|\Psi_S(t)\rangle|^2$, for a two site configuration, as a function of the electron-phonon coupling strength g, for $\omega_0 = h/4$. As the coupling g increases, more phonons are created, the Hilbert space describing the dynamics enlarges and the fidelity decreases for a fixed number of approximant gates ($r = 10$ here). (b) Dependence of the fidelity loss in the number of sites. Here $g = 0.3\ h$, $\omega_0 = 0.5\ h$, and ten symmetric steps are considered ($r = 10$). The initial state of both plots corresponds to a configuration in which an electron is injected in the site $N/2$ (N even) or $(N+1)/2$ (N odd), and there are no phonons. . . . 34

4.2 Dynamics for the $3+1$ ions configuration of the NN XX Hamiltonian. Dotted curves stand for $\langle\sigma_z^i\rangle_E$ for the exact dynamics, and solid curves stand for $\langle\sigma_z^i\rangle_I$ for realistic ion interactions ($i = 1, 2, 3$ for the first, second and third ion). The parameters are chosen in order to have maxima in the fidelity $F(t) = |\langle\Psi_E(t)|\Psi_I(t)\rangle|^2$ of ~ 0.995 (top black curve) at time steps of $\sim 333\ \nu_1 t$. These time steps can be chosen as Trotter steps. . . . 35

4.3 Fidelity loss for 3+1 ion configuration, involving Trotter simulation with perfect gates and realistic ion interactions, for two and three symmetric Trotter steps. . . . 38

4.4 Dynamics for the 2+1 ions configuration of the NN XX Ising Hamiltonian. Dotted curves stand for $\langle\sigma_z^i\rangle_E$ for the exact dynamics, and solid curves stand for $\langle\sigma_z^i\rangle_I$ for realistic ion interactions ($i = 1, 2$ for the first and second ion). The parameters are chosen in order to have fidelity losses of $1 - F(t) = 1 - |\langle\Psi_E(t)|\Psi_I(t)\rangle|^2 \sim 10^{-4}$ (top black curve) at time steps of $\sim 500/\nu_1$. . . . 40

4.5 Fidelity loss for a 2+1 ions configuration as a function of time and Trotter steps. The simulated Holstein interaction has parameters $g = h/10$, $\omega_0 = h/4$. Dotted and solid lines stand respectively for a simulation with one and two symmetric Trotter steps. Single points stand for the error in the simulation protocol using ion gates. . . . 41

4.6 Mean number of phonons inside a Trotter protocol for a 2+1 ions configuration, for the Hamiltonian $H = H_1 + H_3$, where H_1 is a spin spin XX interaction and H_3 is a spin-phonon coupling interaction. The phonons are excited within the time for the H_3 steps (solid black line), and excited and released to their initial value within the H_1 interactions (dotted red lines), with the typical oscillations for this kind of gates. . . . 41

5.1 Simulating quantum chemistry with trapped ions. (a) Scheme of a trapped-ion setup for quantum simulation, which contains a linear chain of trapped ions confined by a harmonic potential, and external lasers that couple the motional and internal degrees of freedom. (b) Transitions between internal and motional degrees of freedom of the ions in the trap. (c) The normal modes of the trapped ions can simulate the vibrational degrees of freedom of molecules. (d) The internal states of two ions can simulate all four possible configurations of a molecular orbital. 44

5.2 Outline of the quantum-assisted optimization method. (a) The key steps for quantum assisted optimization, which starts from classical solutions. For each new set of parameters λ's, determined by a classical optimization algorithm, the expectation value $\langle H \rangle$ is calculated. The potential energy surface is then obtained by quantum phase estimation. (b) Quantum measurements are performed for the individual terms in H, and the sum is obtained classically. (c) The same procedure is applied for each nuclear configuration $\mathbf{R}$ to probe the energy surface. 45

5.3 Digital error $1 - F$ (curves) along with the accumulated gate error (horizontal lines) versus time in h_{11} energy units, for $n = 1, 2, 3$ Trotter steps in each plot, considering a protocol with an error per Trotter step of $\epsilon = 10^{-3}$ (a), $\epsilon = 10^{-4}$ (b) and $\epsilon = 10^{-5}$ (c). The initial state considered is $|\uparrow\uparrow\downarrow\downarrow\rangle$, in the qubit representation of the Hartree-Fock state in a molecular orbital basis with one electron on the first and second orbital. Vertical lines and arrows define the time domain in which the dominant part of the error is due to the digital approximation. d) Energy of the system, in h_{11} units, for the initial state $|\uparrow\uparrow\downarrow\downarrow\rangle$ for the exact dynamics, versus the digitized one. For a protocol with three Trotter steps the energy is recovered up to a negligible error. 52

6.1 Protocols for digital quantum simulations with transmon qubits. a) Heisenberg model of two qubits. b) Heisenberg model of three qubits. c) Frustrated Ising model of three qubits. Here $R_{x(y)} \equiv R^{x(y)}(\pi/4)$ and $\overline{R}_x \equiv R^x(\pi/2)$. 60

6.2 Fidelity loss for simulated Hamiltonians for three qubits, in the interval $\theta = [0, \pi/4]$, $\theta \equiv Jt$. Curved lines show digital errors, while horizontal lines show the accumulated error due to a single step error of ϵ. Red solid (black dotted) lines stand for higher (lower) digital approximations l. a) Heisenberg model, with $\epsilon = 10^{-2}$, $l = 3, 5$, and b) $\epsilon = 5 \times 10^{-2}$, $l = 2, 3$. c) Transverse field Ising model, with $\epsilon = 10^{-2}$, $l = 3, 5$ and d) $\epsilon = 5 \times 10^{-2}$, $l = 2, 3$. 61

6.3 Dynamics for the simulated Heisenberg model for two transmon qubits, which are initialized in the state $1/\sqrt{5}(|\uparrow\rangle + 2\,|\downarrow\rangle) \otimes |\downarrow\rangle$. Fidelity $F = \mathrm{Tr}(\rho |\Psi_I\rangle\langle\Psi_I|)$ shows the behavior of the protocol for a given simulated phase θ. The ideal spin dynamics $\langle\sigma_i^x\rangle$ for both qubits is plotted versus mean values $\langle\sigma_i^x\rangle_\rho$ obtained with the qubit Hamiltonian H_{t}. 65

7.1 a) Scheme of a setup composed of four TCQs capacitively coupled to a coplanar resonator. The SQUID loops labeled with + and − can be threaded by external magnetic fluxes. b) Generation of many-particle operator $\sigma_1^y\sigma_2^y\sigma_3^y\sigma_4^y$, between the first, second, third and fourth qubits, see Appendix B. Selectivity is obtained by setting the coupling of the other qubits to the resonator to zero. The qubit logical levels $|0\rangle$ and $|1\rangle$ are the first levels of the TCQ, $|00\rangle$ and $|\tilde{01}\rangle$. 70

7.2 a) Transition frequency between the first two levels of the TCQ and b) between the ground state and the third level, as a function of the magnetic fluxes Φ_+ and Φ_-. c) Matrix element $\langle 1|\hat{n}|0\rangle$. d) Variation of $\langle 1|\hat{n}|0\rangle$ along γ. e) The magnetic flux is varied in time to obtain the time dependence $g_+(t) = g_+^s + g_+^d[\cos(\omega_g t) + \cos(\omega_g' t)]$. 72

7.3 a) Numerical power spectrum of the magnetic signal $\Phi_+(t)$, used to obtain $g_+(t)$. b) Power spectrum of $g_+(t)$, obtained by plugging the signal $\Phi_+(t)$. The spectrum has two resonances at ω_g, ω_g', close to the two sidebands at $\omega_r - \tilde{\omega}_+ = 5.5$ GHz and $\omega_r + \tilde{\omega}_+ = 14.5$ GHz (red dotted lines). c) Power spectrum of $g_-(t)$, with the sidebands $\omega_r - \tilde{\omega}_- = 3$ GHz and $\omega_r + \tilde{\omega}_- = 17$ GHz (red dotted lines). 72

7.4 a) Collective entanglement between four TCQs, intialized in their ground states. The ideal state $|\Psi_I\rangle$ follows the dynamics regulated by the Hamiltonian of Eq. (7.1), with $\xi = (g_+^d)^2/4\delta$. The fidelity $F = \mathrm{Tr}[\rho|\Psi_I\rangle\langle\Psi_I|]$ of the TCQ dynamics is plotted, along with mean number of photons $\langle a^\dagger a\rangle$. The ideal mean value of the collective spin oscillation $\langle J_z\rangle$, $J_z = 1/4\sum_{i=1}^4 \sigma_i^z$, is compared with the TCQ one $\langle J_z\rangle_\rho$. b) Fidelities for different resonator frequencies. The fidelity improves as the qubit-resonator detuning increases. The first two peaks have values $F \approx 0.97, 0.93$. . . . 75

8.1 Frequency scheme of the stepwise implementation for the quantum Rabi Hamiltonian. A transmon qubit of frequency ω_q is interacting with a microwave resonator, whose transition frequency is ω_r. The interactions $H_{1,2}$ in Eq. (8.3) are simulated respectively with a Jaynes-Cummings interaction (step 1), and another one with different detuning, anticipated and followed by π pulses (step 2). 78

8.2 A transmon qubit and microwave resonator simulating the quantum Rabi Hamiltonian in the regime $g^R = \omega_r^R$, $\omega_q^R = 0$. The ideal dynamics, plotted in the inset, shows collapses and revivals of the photon and qubit population. The latter are recovered via sequential qubit-resonator interactions and qubit flips. The photon population is pumped to the expected value at the time marked by the arrow. Note that the simulating time $\tilde{t}$ is different from the simulated time t. 80

8.3 Time evolution of the fidelity $F = |\langle\Psi_S|\Psi_R\rangle|^2$ of state $|\Psi_S\rangle$ evolving according to the digitized protocol, to the ideal state $|\Psi_R\rangle$ evolving according to the quantum Rabi dynamics, with a) $g^R = \omega_r^R/2 = \omega_q^R/2$, b) $g^R = \omega_r^R = \omega_q^R$, c) $g^R = 2\omega_r^R = \omega_q^R$, and d) $g^R = 2\omega_r^R = 1.5\omega_q^R$. The simulation is performed for different number n of Trotter steps. Black curves in the insets show the overlap of the ideal evolved state with the one at time $t = 0$, $|\langle\Psi_R|\Psi_0\rangle|^2$, initialized with a fully excited qubit and the resonator in the vacuum state. 82

9.1 (a) The distribution of the fluid density on a 2-dimensional lattice can be simulated, for example, via normal motional modes and internal levels of a set of trapped ions (b). (c) Superposition of two motional modes entangled with pseudo spin states can encode velocity distributions in different lattice directions. 89

9.2 (a) Probability of success P_s per time step of simulating real symmetric random matrices as a function of the number of ancillary measurements N (solid lines), together with accumulated probabilities for the whole protocol (dashed lines) (b) Probability of succes of a single step as a function of γ/γ_0, when $N = 10$. 91

9.3 Spectrum of a collision operator (solid red line) for advection-diffusion process of a four-speed lattice as a function of the evolution time step Δt, in units of $1/\omega_4$. The allowed region for γ is bounded by dashed blue lines using Eq. (9.7) and shadowed in the picture. 94

D.1 a) Scheme of the generation of many-particle operator among four TCQs. The coupling of the four qubits to the resonator is shown as a function of time. Collective gates as in Eq. (C.8) are performed in the initial and final time regions, while a standard phase gate is performed upon the first qubit between the two collective operations. The effective interaction can be mapped on an arbitrary stabilizer operator on a spin lattice with generic topology, due to the non-local nature of the quantum bus. With an additional ancillary qubit, the system state can be mapped on the ground states of topological codes, via stabilizer pumping. 114

List of publications

I) The results of this Thesis are based on the following articles

Published Articles

1. A. Mezzacapo, J. Casanova, L. Lamata, and E. Solano
   Topological qubits with Majorana fermions in trapped ions
   New J. Phys. **15**, 033005 (2013).

2. J. Casanova, L. Lamata, A. Mezzacapo, and E. Solano
   Quantum simulation of interacting fermion lattice models in trapped ions
   Phys. Rev. Lett. **108**, 190502 (2012).

3. A. Mezzacapo, J. Casanova, L. Lamata, and E. Solano
   Digital quantum simulation of the Holstein model in trapped ions
   Phys. Rev. Lett. **109**, 200501 (2012).

4. M.-H. Yung, J. Casanova, J. McClean, A. Mezzacapo, L. Lamata, A. Aspuru-Guzik, and E. Solano
   From transistor to trapped-ion computers for quantum chemistry
   Sci. Rep. **4**, 3589 (2013).

5. U. Las Heras, A. Mezzacapo, L. Lamata, S. Filipp, A. Wallraff, and E. Solano
   Digital quantum simulation of spin systems in superconducting circuits
   Phys. Rev. Lett. **112**, 200501 (2014).

6. A. Mezzacapo, L. Lamata, S. Filipp, and E. Solano
   Many-body interactions with tunable-coupling transmon qubits
   Phys. Rev. Lett. **113**, 050501 (2014).

7. A. Mezzacapo, U. Las Heras, J. S. Pedernales, L. DiCarlo, E. Solano, and L. Lamata
   Digital Quantum Rabi and Dicke models in superconducting circuits
   Sci. Rep. **4**, 7482 (2014).

Submitted Articles

8. A. Mezzacapo, M. Sanz, L. Lamata, I. L. Egusquiza, S. Succi, and E. Solano
   Quantum simulator for transport phenomena in fluid flows
   e-print arXiv:1502.00515, submitted for publication.

II) Other articles produced during the Thesis period and not included

Published Articles

9. P. Lucignano, A. Mezzacapo, F. Tafuri, and A. Tagliacozzo
   Advantages of using high-temperature cuprate superconductor heterostructures in the search for Majorana fermions
   Phys. Rev. B **86**, 144513 (2012).

10. L. Lamata, A. Mezzacapo, J. Casanova, and E. Solano
    Efficient quantum simulation of fermionic and bosonic models in trapped ions
    EPJ Quantum Technology **1**, 9 (2014).

11. L. García Álvarez, J. Casanova, A. Mezzacapo, I. L. Egusquiza, L. Lamata, G. Romero, and E. Solano
    Fermion-fermion scattering in quantum field theory with superconducting circuits
    Phys. Rev. Lett. **114**, 070502 (2015).

12. U. Las Heras, L. García-Álvarez, A. Mezzacapo, E. Solano, and L. Lamata
    Fermionic models with superconducting circuits
    EPJ Quantum Technology **2**, 8 (2015).

Submitted Articles

13. Y. Salathé, M. Mondal, M. Oppliger, J. Heinsoo, P. Kurpiers, A. Potoĉnik, A. Mezzacapo, U. Las Heras, L. Lamata, E. Solano, S. Filipp, and A. Wallraff
Digital quantum simulation of spin models in circuit quantum electrodynamics
e-print arXiv:1502.06778, submitted for publication.

14. A. Mezzacapo, E. Rico, C. Sabín, I. L. Egusquiza, L. Lamata, and E. Solano
Non-Abelian $SU(2)$ *lattice gauge theories in superconducting qubits*
submitted for publication.

Chapter 1

Introduction

1.1 Complexity in quantum technologies

Since its early days, the theory of quantum mechanics has been successfully used to explain a large variety of phenomena at very different energy scales. The theoretical predictions based on the present theory of quantum mechanics have been able to explain experiments in very different contexts, ranging from molecular to solid state and high energy physics. The complementary developments in understanding quantum mechanics, on both theoretical and experimental sides, have led to a set of sophisticated controlled quantum platforms, which are able to host and control quantum mechanical effects with increasing effectiveness. This increased ability to control quantum mechanical effects led in turn to the idea that quantum mechanics can be used to assist convenient tasks, which otherwise would be very hard to perform with classical devices.

In the second half of the twentieth century, scientists started to realize that two of the most successful theoretical machineries been known at that time, namely quantum mechanics and the theory of information processing, could be combined together. Richard Feynman was the first to envision in 1960 the computational power of nanoscale quantum systems in his speech “There’s Plenty of Room at the Bottom” [1] and then finally defined the idea of a *quantum computer* in 1982 [2, 3], a device that makes explicit use of its quantum mechanical nature to carry out computations that can be used for external purposes. His first proposal for such devices was the quantum simulation of quantum mechanical problems. Standard numerical methods have intrinsic difficulties when it comes to compute efficiently quantum many-body problems, while a quantum device with controllable parameters could give insights on the behaviour of many-body hard problems in an efficient way. Therefore, the first version of a quantum computer was indeed closer to the idea of a *quantum simulator*. Nowadays we define a quantum simulator as a quantum device with strong control on a set of quantum degrees of freedom, which can be used to intentionally recover the unaccessible dynamics of another, less controllable, quantum system.

Motivations oriented towards quantum computing and quantum simulations have started a race to the realization of diverse experimental versions of controllable quantum platforms. These platforms must possess great control over a set of manipulable quantum parameters, scalability to large sizes, and isolation to the external environment, in order to address and solve quantum information problems. The search for a quantum platform with all these features has generated complex experimental and theoretical challenges. Such challenges do neither belong to the exploration of the most fundamental aspects of quantum mechanics, nor to the basic mechanisms of a particular working quantum platform. They rather resemble complex engineering and technological design problems, and their advances can be considered as *Quantum Technology*. On the other hand, once the challenges to scalability and controllability have been solved, the attention is conveyed to the set of problems that can be encoded in actual quantum devices, in order to unravel all their computational power.

To date, the most advanced experimental setups, in terms of controllability and scalability to large sizes, are trapped-ion setups, optical lattices made of cold atoms, photonic devices, and superconducting circuit architectures. These systems can host interesting quantum simulation experiments at current stage of technology [4–7].

1.1.1 Trapped ions

Experimental setups based on trapped ions have reached a level of control that makes them to be considered as one of the most promising technologies for hosting quantum information protocols. In general, atomic systems such as ion traps have the advantage of long coherence times, because it is easy to isolate them from the environment. Furthermore, their properties (e.g. atomic transition frequencies) are stable and defined by nature.

Typical qubits are encoded into hyperfine or Zeeman states [8]. The sensitivity and quantum coherence of ion-trap qubits depend strongly on the coupling mechanisms of the qubit ground-excited transition with the external electromagnetic noise, ranging from milliseconds up to seconds. Quantum operations between these levels are driven with lasers, whose intensity controls the Rabi frequency of the qubit transition. Qubit readout is performed through fluorescence measurements [9], in which one of the two states of the qubit is coupled to an excited level that decays fast. Two-point correlation functions between distant qubits can be obtained by spatially resolved fluorescence.

The ions are trapped via electromagnetic fields, and the residual motional modes that survive the trapping can be cooled down with sideband cooling [10, 11]. The idea to realize two-qubit gates for quantum computing between different ions came up in 1995 [12], and was later improved in different manners, including one insensitive to motional temperature [13]. In these works, it was anticipated that the quantum degrees of freedom of the motional modes of the ion chain could be used as a quantum bus to transport information between distant ions. This approach, combined with single ion laser addressing, can in principle generate any nonlocal two-qubit gate between any pair of ions in a Paul trap. The quantum control in state preparation, readout and single and two-qubit gates has reached nowadays impressive levels [14, 15].

The toolbox of interactions available in ion-trap experiments allows for a variety of quantum simulation experiments that have shown already a great complexity. Quantum Ising Hamiltonians have been generated following an adiabatic protocol between two ions [16]. In these protocols, a pair of counter-propagating laser beams detuned to red and blue sideband transitions can take into account the simulation of the spin-spin interaction, while another laser beam is used to simulate the magnetic field. These ideas have been implemented in Penning traps, up to hundreds of ions [17]. These kinds of quantum simulation experiments may challenge classical computers, if long-range and arbitrary spin-spin interactions are implemented [18]. The versatility of the ion-trap quantum simulator has been used to make internal ion levels behave like relativistic particles [19–21], by coupling a motional mode to four internal levels of a single ion with red and blue sideband transitions and Stark shifts obtained by laser detuning. The free relativistic model can be complemented with the addition of linear and quadratic potentials [22], giving the possibility of simulating purely relativistic effects such as Klein tunnelling [23].

The ability of generating high fidelity quantum gates in a consecutive way has allowed for the realization of a reliable digital quantum simulator [24, 25]. The ion-trap digital simulator works for a variety of time-independent and time-dependent Ising spin models, being able to implement many-body terms up to six-qubit interactions.

The ion-trap quantum computer at the state-of-the-art quantum technology has been proved to be a extraordinary and reliable platform, and future challenges are in the scalability and adressability at the single-ion level of these devices. The race to scalability of atomic devices has to face the flexibility and the engineering possibilities of the artificial atoms of circuit quantum electrodynamics, which will be briefly introduced in the next section.

1.1.2 Circuit quantum electrodynamics

The advent of circuit quantum electrodynamics (cQED) has changed the previous common belief that solid-state macroscopic devices cannot host quantum computational purposes. Superconducting quantum circuits are devices based mainly on LC oscillators and Josephson junctions. They work at cryogenic temperatures below their superconducting transition of the material, which is usually aluminium.

The three basic elements of which superconducting artificial atoms are made of, i.e. inductances, capacitances and Josephson junctions, can be manufactured and used in different parameter regimes to obtain different behaviors. The basic types of superconducting qubits were originally the charge [26, 27], flux [28] and phase [29] qubits. A modification to the capacitances in the original design of the charge qubits has brought to the so called *transmon* qubits [30]. In fact, one of the main drawbacks of using a charge qubit for quantum information protocols is its sensitivity with respect to external electromagnetic fluctuations. This is due to the quantum spectrum of this device, which is very sensitive to charge fluctuations. In a transmon qubit, the dephasing noise due to charge fluctuations is suppressed because of the flattened charge dispersion relation, obtained with an increased shunt capacitance. In this Thesis, we will mostly deal with charge-based qubits, being the type of qubit used at the present time in most cQED labs.

These artificial atoms made of superconducting circuits can be coupled to microwave resonators [31, 32]. A dispersive coupling with the resonators allows to perform non-demolition readout of superconducting qubits. Furthermore, single qubit gates can be performed with microwave signals sent through the resonators. Standard transmon qubit setups coupled to microwave resonators can have coherence times of about tens of microseconds, while quantum gates can have execution times from few to tens of nanoseconds, in the case of single qubit rotations, and tens to hundreds of nanoseconds for two-qubit operations. This allows for hundreds of operations within the coherence time of the device [33]. These long coherence times are the current expression of the *Moore law* for the scaling of coherence in superconducting devices [34]. The hope that this law will stand in the future, due to technological improvements and better circuit designs, makes cQED architectures strong candidates for encoding complex quantum protocols.

Lattices of microwave resonators coupled to on-site qubits can simulate arrays of coupled bosonic systems. The fabrication of such arrays is indeed not a hard task [7], and these systems may predict new discoveries in strongly correlated bosonic systems. The easiness of the fabrication of these devices, due to the lithographical techniques, could allow for scaling these lattices to many sites and recover, for example, a superfluid to Mott insulator transition [35]. The presence of photonic losses in these setups can be viewed both as a drawback when trying to simulate unitary dynamics and as an advantage when the simulation of open quantum systems is considered.

Summarizing, cQED stand as one of the most reliable and promising platforms for quantum information processing, and by far the system that has shown the fastest progress in the last years.

1.2 Quantum simulations

The prediction of the behavior of quantum mechanical systems is one of the hardest known problems. Understanding and solving quantum systems has profound implications in both fundamental knowledge and applied technology, ranging from high-energy physics to material science, from chemistry to computer science. Unfortunately, this challenge is hard, due to problems that cannot in general be addressed by standard mathematical and numerical techniques. To overcome this fundamental adversity, Feynman proposed to use directly a quantum simulator to make predictions on quantum systems [2, 3]. The idea to use such devices to predict the behavior of quantum systems was later formalized into the concept of a universal quantum simulator [24].

Nowadays quantum simulators are well known to the physics community [36]. They can be classified into two main families, *analog* and *digital* quantum simulators.

1.2.1 Analog quantum simulators

An analog quantum simulator is a device that can *continuously* mimic the quantum dynamics of another quantum system. The unitary dynamics of a closed quantum system S can be encoded in its quantum state $|\Psi(t)\rangle$, and determined at all times by specifying a Hamiltonian H and the state at $t = 0$, $|\Psi(0)\rangle$. An analog quantum simulator is a device that can predict total or partial information about $|\Psi(t)\rangle$, by performing measurements on a quantum system S', whose state dynamics is represented by $|\Psi'(t)\rangle$ and regulated by a Hamiltonian H'. The predictions on S are given by defining a mapping $\mathcal{M}$ between the two quantum dynamics. In most cases this mapping is the identity, i.e. $\mathcal{M}(H) = H'$, $\mathcal{M}(|\Psi(t)\rangle) = |\Psi'(t)\rangle$, and the quantum systems have the same representation. Indeed, the controllability and readability of S' allow for reliable and non-trivial predictions over S. Typically, S can be a high-energy or condensed matter system, whose behavior is unknown, while S' stands for a controlled quantum platform, such as cold atom or trapped-ion setups.

Due to the natural presence of the interaction Hamiltonian H' at all times t, analog quantum simulations are most suitable to encode ground state searching problems, and obtain phase diagrams. In general, analog simulators are quantum devices with large sizes, with few degrees of freedom and quantum control [7, 16, 17, 37, 38]. The reduced flexibility of the interactions that may be implemented, together with the difficulties in state preparation, make this class of simulators less suitable for encoding and retrieving dynamical quantities. Usually the efforts in simulating real-time dynamics in these devices go in the direction of quenching a few system parameters, and observing interesting properties of the physical system, like relaxation times, response functions and thermalization. These quantities may be very hard to simulate classically, and some analog quantum simulators are already at the frontier of the classical computational devices [39].

One of the main open challenges of analog quantum simulators is to certify their predictions, i.e. to give error bars on the measurements produced. Ideally, a quantum simulator is a device that makes predictions that are very hard to retrieve classically. Therefore, certifying the output of such experiments is a tough problem. This drawback may be overcome by a digital approach to quantum simulations, in that in this case one can implement error corrected simulations, at the expense of simulation efficiency. In fact, in an analog approach time efficiency of the simulation is maximized, because one has to prepare the initial state of the simulation and wait for a certain evolution time t. On the other hand, in a digital approach, the total dynamics is decomposed into a set of quantum gates: while time efficiency may be worse, a digital protocol can be universal, and is more suitable for quantum error correction protocols.

1.2.2 Digital quantum simulators

While in analog simulations one establishes a direct mapping between two quantum dynamics, in the digital approach the dynamics of the simulated system is decomposed in a set of quantum interactions. These interactions are typically easier to implement in a specific quantum platform with respect to the total dynamics H'. In this case, one can approximate the simulated dynamics as a series of m quantum gates

$$e^{-iHt} \approx \prod_{i=1}^{m} e^{-ih_i\tau_i}. \tag{1.1}$$

Usually one considers that $H = \sum_{i=1}^{m} H_i$, and uses Suzuki-Lie-Trotter decompositions [40]. The basic instance of a Suzuki-Lie-Trotter decomposition is the Trotter approximation [41],

$$e^{-iHt} = \left(e^{-iH_1 t/l} \cdots e^{-iH_m t/l}\right)^l + \sum_{i<j} \frac{[H_i, H_j]t^2}{2l} + \sum_{k=3}^{\infty} E(k), \tag{1.2}$$

where $l||Ht/l||^k_{\text{sup}}/k! \geq ||E(k)||_{\text{sup}}$ is an upper bound on the higher order approximant. In this kind of approximations the exact dynamics e^{-iHt} is exactly recovered as the number of repetitions l increases. Any unitary operator $U = e^{iHt}$ can be in principle written in terms of a universal set of quantum gates: this fact makes the digital quantum simulator universal [24]. Furthermore, the possibility of performing error correction protocols on the single gates can be taken into account for the problem of certifying the simulation. On the other hand, finding the exact sequence of approximants as in Eq. (1.1) can be a hard task [42]. Also, the number of quantum gates required to retrieve the simulation with good accuracy for long times can be very high, requiring quantum devices with very large coherence times and high gate fidelities.

The prediction of any digital quantum simulator will be affected by errors associated to each quantum gate. Typically, by using more gates one reduces the digital error on the simulated dynamics. On the other hand, using many quantum gates will affect the fidelity of the simulation. Therefore, one has to employ a tradeoff between the improved fidelity obtained by using large sequences of approximants and the accumulated experimental error coming from a large sequence of gates. Recent experiments [33, 43] have proved that the total error in a digital quantum simulation accumulates linearly, certifying that any effort to improve gate fidelity will be rewarded with a linear gain on the total simulation fidelity. To avoid the error accumulation, a quantum simulator based on error-corrected gates may override this tradeoff in the future.

1.3 This Thesis

In this Thesis, we consider the practical realization of several quantum protocols in different quantum platforms, mostly trapped-ion setups and cQED architectures. We are particularly concerned with the limits of each specific quantum platform, being in coherence times, scalability, sources of errors, and types of quantum interactions. We justify how each of the ideas presented here can be best adapted to a certain experimental platform, exploiting specific tasks.

Quantum simulations are the most natural tasks for a quantum architecture, being straightforward to think in correspondences between two quantum systems: the simulating and the simulated one, respectively. In this sense, mapping a quantum dynamics onto a non-quantum problem (e.g. factoring of large numbers) is indeed less natural and cumbersome. A quantum simulation requires great control over the quantum degrees of freedom of a certain device, but this is not always possible. Carefully benchmarking of the realistic possibilities and drawbacks of each specific quantum platform is mandatory, in order to study the simulation complexity addressable in an experiment. The analysis of this complexity is the leitmotiv of this Thesis.

For example, besides benchmarking several quantum simulation protocols versus current state-of-the-art technology, in the first part of the Thesis we propose the implementation of a protected qubit [44], made up of internal levels of several ions. This can be viewed as a quantum simulation of a topologically protected Kitaev chain, which hosts Majorana fermions. The simulation, besides implementing a mapping between two quantum models, also conserves some *properties* beyond state dynamics, such as the protection of the ground state versus local errors. In the quantum simulation of fermionic, coupled bosonic-fermionic, and quantum chemistry systems a particular emphasis is given on the efficiency of the protocols. We prove that by using collective gates such systems can be simulated more efficiently. The use of the collective gates, being only available to ion-trap systems, is a paradigmatic example of a quantum protocol specifically designed for a certain quantum platform that cannot be reproduced elsewhere. We believe that this approach to quantum information and simulation is paradigmatic, and systematic study of each experimental device is mandatory in order to design more efficient protocols.

This Thesis contains an introductory Chapter 1, followed by three Parts, each of them containing several Chapters, with links to various Appendices at the end of the Thesis:

I **Trapped ions**

In the first part of this Thesis, we address various ideas of using high-end quantum information protocols, specifically designed for current state-of-the-art ion-trap setups. In Chapter 2, we present a minimal instance of a passively protected qubit that can be encoded in actual ion-trap platform. The parity-based protected qubit is based on a spin-dual representation of unpaired Majorana fermions in a topological fermionic wire. In Chapter 3, we consider the simulation of fermionic models in trapped ion devices, and find that high-order fermionic operators could be efficiently implemented in current experiments, by means of collective entangling gates. The use of this gates reduces drastically the quantum resources for the simulation of fermionic dynamics in previous algorithms. In Chapter 4 we will present a digital quantum simulation of a coupled bosonic-fermionic model, namely the Holstein model. We analyze to which extent current ion-trap technology allows for the simulation of this model. Finally, in Chapter 5 we present a hybrid classical-quantum simulator for quantum chemistry problems in a ion-trap platform. The simulator uses quantum resources to perform a phase estimation algorithm that can allow for the retrieval of molecular energies.

II **Superconducting circuits**

In the second part of the Thesis, we will focus on superconducting circuits, and the possibility of hosting complex dynamics with current chip designs. In Chapter 6, a universal digital quantum simulator for generic spin dynamics is presented. By using standard dispersive two-qubit interactions between pairs of transmon qubits and single qubit rotations, we demonstrate that a variety of interacting spin dynamics can be simulated, including paradigmatic Heisenberg and Ising interactions. In Chapter 7, we show that many-body operators can be dynamically encoded in a cQED setup, by using sequences of collective gates and single-qubit rotations. The collective gates are realized by fast driving of two SQUID loops embedded in three-island transmon qubits. This dynamics is equivalent to a collective gate in ion-trap systems [13] obtained by simultaneous red and blue detuned sidebands upon the ions. The Chapter 8 is dedicated to the proposal of the simulation of a quantum Rabi interaction in cQED setup. The interaction is simulated digitally by using Jaynes-Cummings and anti Jaynes-Cummings digital steps. The anti Jaynes-Cummings step is simulated with local rotations and the standard qubit-resonator interacions.

III **Quantum simulation of classical systems**

In the last part of this Thesis, Chapter 9, we describe how quantum simulators are devices capable of solving complex classical problems. As an example, we consider the simulation of transport phenomena in fluid flows. The quantum simulation of such phenomena is encoded in a generic coupled pseudospin-bosonic system. The fluid dynamics is first described in a kinetic lattice formalism. Then, once the problem is set within a lattice Boltzmann approach, we show how a properly encoded wavefunction, which lives in a Hilbert space composed of a set of discretized energy levels and bossing fields, can describe the state of the Boltzmann lattice. We explicitly explore this possibility with an enlightening example on a four-speed advection-diffusion problem.

IV **Appendix**

The Appendices contained in this Thesis provide with additional numerical and analytical calculations to support the main results. In Appendix A we explicitly compute an upper bound for the norm of the Holstein Hamiltonian, which serves to demonstrate the efficiency of the quantum simulation protocol presented in Chapter 4. In Appendix B we analytically compute non nearest neighbour interactions, which arise when one tries to implement an Ising interaction in a multiple laser beam approach on a set of trapped ions. Appendix C deals with the derivation of the effective collective interaction between many tunable-coupling transmon qubits. In Appendix D we derive many body operators, obtained with a sequence of collective and single qubit gates, in a cQED architecture.

Part I

Complex systems in trapped ions

Chapter 2

Protected Majorana parity qubits in trapped ions

2.1 Introduction

In this Chapter, we propose the implementation of a protected logical qubit in trapped-ion systems. Topologically protected systems offer promising properties for the building of a fault-tolerant quantum memory [45]. However, the realization of topological quantum memories up to now represents a challenging open problem. Here we face the problem from a bottom-up approach, by asking what is the minimal set of experimental requirements to build, on a trapped-ion system, a working logical qubit with quantum control, provided with coherence times superior to the ones of the physical qubit.

The discrete quantum wire model by A. Kitaev is one of the simplest systems supporting topological phases [46]. In this model, the signature for the topological nontrivial phase is the presence of unpaired Majorana fermions. Among their properties, these fermions coincide with their own antiparticles and support non-Abelian statistics [47]. Since its appearance, the model has attracted much interest, with diverse proposals for physical implementations, including superconducting heterostructures [48, 49] and optical lattices [50, 51]. Signatures of these particles have been recently measured [52]. However, a clear way to use the fault-tolerant properties of Majorana modes has not been experimentally achieved. In general, building a qubit made out of Majorana fermions requires exceptional system control.

Trapped ions are highly controllable quantum systems [8]. They can be cooled down to form crystals, easily initialized by optical pumping, manipulated with lasers, and efficiently measured. They offer one of the most reliable and scalable implementations for a quantum simulator [2, 24]. Some examples are spin systems [16, 25, 53–56], relativistic quantum mechanics [19–23, 57], quantum field theories [58, 59], and fermionic systems [60]. A proposal for realizing another topological system, i.e., Kitaev honeycomb model, was put forward in Ref. [61]. However, the complexity of the honeycomb model, requiring three different kinds of interactions, XX, YY, and ZZ, is much higher than the one of the wire model, that only requires an XX interaction. Another proposal for topological systems in trapped ions [62], not involving Majorana fermions, makes use of a highly nonlocal Hamiltonian.

We propose the implementation of Kitaev wire model [46] in a linear chain of trapped ions. By a mapping the Kitaev Hamiltonian onto a spin model, we show that this system can be realized in a trapped-ion chain with current technology, and a Majorana-fermion (MF) qubit can be encoded. This qubit will be topologically protected against major sources of decoherence for longer times, constituting an efficient quantum memory. The proposed implementation, already valid for 3 ions, allows for the straightforward realization of local operations on the MF qubit and for an efficient readout of its state. We also show that a quantum interface between highly entangled incoming photonic states and MF qubits can be implemented by grouping many of these basic units. To this end, we suggest the use of an array of ion chains inside a set of cavities as a possible experimental realization.

2.2 Trapped-ion implementation

We begin by considering the Kitaev Hamiltonian [46] made up of N spinless fermionic sites ($\hbar = 1$),

$$H = \sum_{j=1}^{N-1} [-w(a_j^\dagger a_{j+1} + a_{j+1}^\dagger a_j) + \Delta a_j a_{j+1} + \Delta^* a_{j+1}^\dagger a_j^\dagger] - \mu \sum_{j=1}^{N} \left(a_j^\dagger a_j - \frac{1}{2} \right), \tag{2.1}$$

where the operators $a_i(a_i^\dagger)$ are the annihilation (creation) operators of spinless fermions on the site i, satisfying $\{a_i, a_j^\dagger\} = \delta_{ij}$, w is the hopping energy, μ is a chemical potential and Δ is the order parameter of the pairing term, which mimics a p-wave spinless superconductivity. Given that $\Delta = |\Delta| e^{i\phi}$, one can define a set of $2N$ Majorana fermions $c_{2j-1} = e^{i\frac{\phi}{2}} a_j + e^{-i\frac{\phi}{2}} a_j^\dagger$, $c_{2j} = -ie^{i\frac{\phi}{2}} a_j + ie^{-i\frac{\phi}{2}} a_j^\dagger$, and the Hamiltonian becomes

$$\begin{aligned} H_M &= \frac{i}{2}\{-\sum_{j=1}^{N} \mu c_{2j-1} c_{2j} + \sum_{j=1}^{N-1} [(w + |\Delta|) c_{2j} c_{2j+1} \\ &\quad + (-w + |\Delta|) c_{2j-1} c_{2j+2}]\}. \end{aligned} \tag{2.2}$$

Under the parameter regime $\mu = 0$, $|\Delta| = w > 0$ the Majorana fermions c_1 and c_{2N} disappear, and H_M becomes diagonal in the basis $\tilde{a}_j = \frac{1}{2}(c_{2j} + ic_{2j+1})$, $j = 1, ..., N-1$. One can pair the two outer Majorana fermions into an additional complex fermion $a_M^\dagger = (c_1 + ic_{2N})/2$. The ground state is two-fold degenerate, and is spanned by the states $|\Psi_0\rangle$ and $|\Psi_1\rangle$ defined by $\tilde{a}_i|\Psi_{0,1}\rangle = 0$, $\forall i = 1, 2, ..., N-1$ and $a_M|\Psi_0\rangle = 0$, $|\Psi_1\rangle = a_M^\dagger|\Psi_0\rangle$. This ground state is separated by a gap $2w$ from the higher-energy excitations of the system. It was proved [46] that these states survive in the regime $|\mu| \ll 2w$. Under this regime one has a nontrivial value for the topological invariant $\mathbb{Z}_2$, that labels the two different topological phases of the ground state.

In order to implement the Kitaev model in an ion string, we take into account that Hamiltonian in Eq. (2.1), for the parameter regime $\phi = 0$, which does not reduce the generality of the model, and $|\Delta| = w > 0$, can be mapped onto the transverse field Ising model by using a Jordan-Wigner transformation [63, 64],

$$H_s = -J \sum_{j=1}^{N-1} \sigma_j^x \sigma_{j+1}^x - h_z \sum_{j=1}^{N} \sigma_j^z, \tag{2.3}$$

where $J = w$ is the exchange coupling and $h_z = -\mu/2$ is a transverse magnetic field. The mapping of the Majorana fermions onto the spins is $c_{2j} = \prod_{k=1}^{j-1} \sigma_k^z \sigma_j^y$, $c_{2j-1} = \prod_{k=1}^{j-1} \sigma_k^z \sigma_j^x$. The definitions of a_M, $\tilde{a}_i$, and $|\Psi_{0,1}\rangle$ change accordingly. The two ground states $|\Psi_{0,1}\rangle$ of H_s in Eq. (2.3) consequently span a subspace that is protected from higher-level excitations by the energy gap $2w = 2J$.

Hamiltonian (2.3) can be implemented with standard trapped-ion technology [8]. We consider a 1D string of N two-level ions coupled through the joint motional modes by means of external lasers. One possibility is to apply Raman lasers for the spin-spin interaction and for the magnetic field at the same time [53, 54, 65]. By locally addressing each ion with different Raman beatnotes, in a multiple Mølmer-Sørensen configuration, one can achieve the $\sum_{j=1}^{N-1} \sigma_j^x \sigma_{j+1}^x$ interaction with open boundary conditions in Eq. (2.3), while a single laser can implement the $\sum_j \sigma_j^z$ part [65].

Here, we are interested in the pure Majorana regime in which $J \gg |h_z|$. The aim is to achieve this regime in the always-on interaction, such that the degenerate ground state of Hamiltonian (2.3) encodes the topologically protected subspace. This degenerate ground state is composed of two Greenberger-Horne-Zeilinger (GHZ)-like states in the X basis, that are highly entangled, $|\Psi_0\rangle = (|\leftarrow\leftarrow ... \leftarrow\rangle - |\rightarrow\rightarrow ... \rightarrow\rangle)/\sqrt{2}$, and $|\Psi_1\rangle = (|\leftarrow\leftarrow ... \leftarrow\rangle + |\rightarrow\rightarrow ... \rightarrow\rangle)/\sqrt{2}$. These states have different parity $P = -\prod_i \sigma_i^z$, $P|\Psi_{0,1}\rangle = \pm|\Psi_{0,1}\rangle$, which is a conserved quantity with respect to Hamiltonian (2.3). On the other hand, they can also be easily achieved using an adiabatic evolution [66] from the opposite regime in which $J \ll |h_z|$. The ground state of the Hamiltonian $-h_z \sum_j \sigma_j^z$

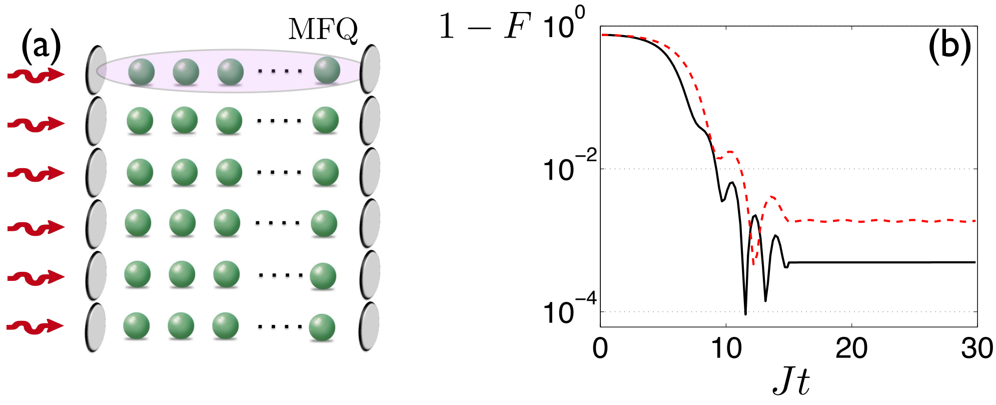

Figure 2.1: (a) Array of 1D ion crystals inside K optical cavities for the quantum interface between a multiqubit entangled photonic state and a MF qubit multipartite state. The shaded region denotes a single MF qubit. (b) Fidelity loss $1-F=1-|\langle\Psi_0|\psi(t)\rangle|^2$ for the evolved state $|\psi(t)\rangle$ from the initial state $|\Psi_0^{\rm init}\rangle$ using the adiabatic transfer protocol with H_s in Eq. (2.3), for $N=3$. The diabatic error for the ideal protocol (black solid line) is plotted against the diabatic error (red dotted line), obtained including a constant magnetic field in the Z direction of magnitude $\delta h_z = 10^{-3}J$ [14], a 1% error on the relative coupling magnitude J_{12}/J_{23} and a NNN coupling $J_{13}=J_{12}/8$.

for $h_z<0$, $|\Psi_0^{\rm init}\rangle = |{\downarrow\downarrow}\dots\downarrow\rangle$ is mapped adiabatically onto the ground state $|\Psi_0\rangle$ of the Hamiltonian $-J\sum_{j=1}^{N-1}\sigma_j^x\sigma_{j+1}^x$ for odd N, and to $|\Psi_1\rangle$ for even N. In turn, one specific linear combination of the first excited states of $-h_z\sum_j\sigma_j^z$, $|\Psi_1^{\rm init}\rangle = \sum_i c_i|\downarrow\downarrow\dots\uparrow_i\dots\downarrow\rangle$, is mapped onto the other ground state. For instance, for $N=3$, $c_1=c_3=1/2$, and $c_2=1/\sqrt{2}$. Notice, in addition, that the two states will not be mixed during the adiabatic evolution due to their different parity. Despite the closure of the energy gap between the ground and the first excited states, parity commutes with the Hamiltonian at all times during the protocol, such that the dynamics will not mix the two states. This is the reason for the small diabatic error, plotted as a function of time in Fig. 2.1b. Moreover, for three qubits, and for adiabatic enough protocol, the first excited state is not mixed with other single-excitation states, giving similar fidelities than for the ground state, with an adiabatic protocol time similar to the one shown in Fig. 2.1b.

In order to create state $|\Psi_0^{\rm init}\rangle$ one may just apply standard optical pumping. In order to create $|\Psi_1^{\rm init}\rangle$ one may apply an inhomogeneous Tavis-Cummings Hamiltonian [67] with appropriate couplings, engineered with an inhomogeneous red-sideband interaction upon the ions, using the center-of-mass mode (e.g., with displaced equilibrium positions in the trap by a tailored potential [68]). An important point here is that the Hamiltonian in the topological regime has to be turned on all the time to guarantee the topological protection against local noise, as we will explain in the following.

2.3 Quantum Interface

Besides state initialization, the adiabatic mapping can be also used to transfer an arbitrary qubit state that comes into the system, e.g., a photonic qubit, to the MF qubit. One can begin with a photonic incoming state, $\alpha|0\rangle+\beta|1\rangle$, where $|0\rangle$, $|1\rangle$ are Fock states: by using a quantum interface with a cavity, state $|0\rangle$ can be mapped to $|\Psi_0^{\text{init}}\rangle$ and $|1\rangle$ to $|\Psi_1^{\text{init}}\rangle$, by a collective excitation and an intermediate phonon state [69]. We point out that in order to get high fidelities in the coupling to the incoming photon, chains of around 20 ions at least should be employed [69], though for the MF qubit itself, as we will show, 3 ions are enough. Subsequently, the adiabatic transfer will produce the same qubit superposition $\alpha|\Psi_0\rangle+\beta|\Psi_1\rangle$ in the MF qubit. An extension could be considered with K copies of this system, with a highly-entangled incoming photonic state, $\sum c_{i_1...i_K}|i_1...i_K\rangle$. Here each photonic qubit is mapped similarly to the corresponding MF qubit, giving $\sum c_{i_1...i_K}|\Psi_{i_1}...\Psi_{i_K}\rangle$, i.e., an arbitrarily entangled state of nonlocal Majorana-fermion qubits. This could be used as an efficient quantum memory. In Fig. 2.1a we show a scheme of the proposed setup.

2.4 Local operations and measurement

One can efficiently implement local operations upon the MF qubits. In general, these local operations upon the nonlocal MF qubits translate into nonlocal operations upon the physical qubits, i.e., the trapped ions. The complete set of local operations, i.e. Pauli matrices, upon the nonlocal MF qubit, σ^x_{MFQ}, σ^y_{MFQ}, and σ^z_{MFQ}, can be related to the single-ion Pauli operators $\{\sigma_i^{x,y,z}\}_{i=1,..,N}$ through the expressions

$$\begin{aligned}
\sigma^x_{\text{MFQ}} &\equiv a_M^\dagger + a_M = I\otimes I\otimes ...\otimes I\otimes\sigma_1^x,\\
\sigma^y_{\text{MFQ}} &\equiv -i(a_M^\dagger - a_M) = -\sigma_N^y\otimes\sigma_{N-1}^z\otimes ...\otimes\sigma_1^z,\\
\sigma^z_{\text{MFQ}} &\equiv a_M^\dagger a_M - a_M a_M^\dagger = \sigma_N^y\otimes\sigma_{N-1}^z\otimes ...\otimes\sigma_2^z\otimes\sigma_1^y.
\end{aligned}\tag{2.4}$$

As can be appreciated, $\sigma^{y,z}_{\text{MFQ}}$ are highly nonlocal operations upon the ions. Nervertheless, they can be implemented efficiently with a reduced number of lasers as recently shown both theoretically [60, 70], and experimentally [56], using sequences of Mølmer-Sørensen and local gates. Thus, with the proposed setup, we have a fully controllable Majorana-fermion qubit.

The topological qubit readout can be also implemented. A projective measurement upon the basis $\{|\Psi_0\rangle,|\Psi_1\rangle\}$, which is equivalent to detecting the parity operator $P=-\prod_i\sigma_i^z$, amounts to one local measurement of σ^z operator per ion. This is the easiest detection performed in trapped ions and can be done, with standard resonance fluorescence, with fidelities larger than 0.99 [8]. Combined with the local operations exposed above, this allows one for the full tomographic reconstruction of the MF qubit.

2.5 Errors and decoherence protection

The proposed implementation, as has been shown above, contains a degenerate ground state, $\{|\Psi_0\rangle,\ |\Psi_1\rangle\}$, which is protected by a gap from higher-level excitations. A consequence of this is that local operations $\sigma_i^{y,z}$, which couple $\{|\Psi_0\rangle,\ |\Psi_1\rangle\}$ with higher energy states, are topologically supressed. Thus, magnetic field fluctuations along these directions will not have an effect upon the system. On the other hand, local σ_i^x operations realize swap gates between the $|\Psi_0\rangle$ and $|\Psi_1\rangle$ states [64]. In a trapped-ion setup, random ambient magnetic fields along X direction rotate fast in the interaction picture with respect to the trapped-ion qubit energy in which Eq. (3) is computed [65] , such that their contribution to decoherence will be negligible. This is because this spurious interaction is far off-resonant and will not induce transitions. For example, using a quadrupole transition between the two levels $|D_{5/2,3/2}\rangle$ and $|S_{1/2,-1/2}\rangle$ of $^{40}\mathrm{Ca}^+$, with an energy separation of about $\omega_0 = 411$THz, an X error of magnitude $J \cdot 10^{-3}$, e.g. around 6Hz, will rotate in the interaction picture, taking the form $J \cdot 10^{-3}(\sigma^+ e^{i\omega_0 t} + \sigma^- e^{-i\omega_0 t})$, resulting in an effective unintended excitation probability of about 10^{-28}. In general this will also happen with the Y-direction ambient magnetic fields, such that these will be doubly protected: by the topological Hamiltonian and by the single-ion qubit energy transition. Conversely, local rotations in Eq. (2.4) are realized in interaction picture with respect to the ion energy and commute with the Hamiltonian in the topological regime, also in the presence of non-next-neighbour (NNN) couplings, i.e. they can be realized efficiently.

A qubit encoded in the Kitaev wire model [46] is usually considered robust in the large N limit, for the parameter range $|\mu| \ll 2w$. On the other hand, for finite N, the degree of imperfection in the protocol depends on how much the system deviates from the parameter regime $w = |\Delta|$, $\mu = 0$. Indeed, the appearing energy splitting Γ between $|\Psi_0\rangle$ and $|\Psi_1\rangle$, which breaks the ground-state degeneracy and qubit coherence [46], is of the order of $\Gamma \propto \exp(-N/n_0)$, where $n_0^{-1} = \min\{|\ln|x_+||, |\ln|x_-||\}$, and $x_\pm = (-\mu \pm \sqrt{\mu^2 - 4w^2 + 4|\Delta|^2})/[2(w + |\Delta|)]$. We consider $J/2\pi \sim 6$ kHz for the 3 ion case. For realistic imperfections in the Rabi frequencies of the lasers of 1%, that induce the same order of imperfection in $w = |\Delta| = J$, and magnetic field fluctuations in $\delta h_z = 10^{-3}J$ [14], we have $n_0 \simeq 0.14$. The splitting computed numerically as a function of the number of sites is plotted in Fig. (2.2). This makes the implementation of the wire

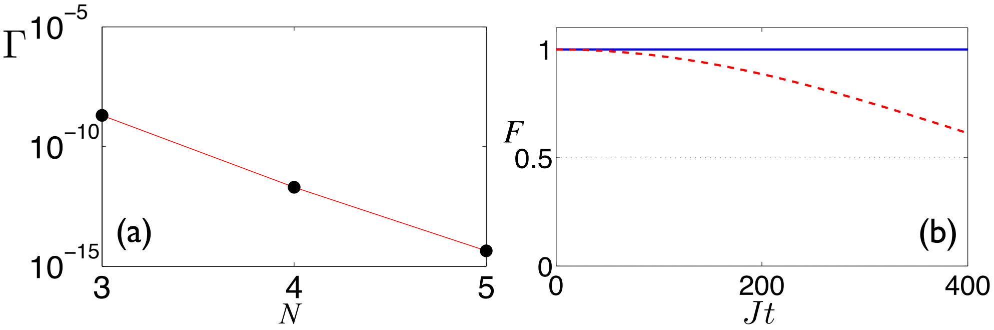

FIGURE 2.2: (a) Energy splitting Γ between $|\Psi_0\rangle$ and $|\Psi_1\rangle$ as a function of number of sites N, in units of $J = 1$, computed numerically for $\delta h_z = 10^{-3}J$ and 1% error on the relative magnitude J_{12}/J_{23}. (b) Survival probability $F = |\langle\Psi_0|\psi(t)\rangle|^2$ for the evolved state $|\psi(t)\rangle$ from $|\Psi_0\rangle$ under the dynamics of Hamiltonian (2.3) (with $h_z = 0$) (solid) or without it, i.e. free evolution of the state (dashed), plus constant local operators of modulus $10^{-3}J$, proportional to σ_i^z, for $N = 3$. The topological Hamiltonian provides protection against the σ_i^z noise.

model and Majorana fermions in trapped ions a real possibility with current technology. We show below that considering a linear chain of just $N = 3$ ions, one may encode a topologically-protected qubit subspace with very low decoherence.

In order to test the feasibility of the implementation with realistic trapped-ion systems, we have realized numerical simulations with different kinds of imperfections. With respect to the adiabatic protocol with H_s in Eq. (2.3), we have computed the fidelity loss $1 - F(t) = 1 - |\langle\Psi_0|\psi(t)\rangle|^2$ for the evolved state $|\psi(t)\rangle$ from $|\Psi_0^{\text{init}}\rangle$, making the evolution $|h_z|/J \gg 1 \rightarrow |h_z|/J \ll 1$, for $N = 3$, see Fig. 2.1b. We consider the ideal case with no ambient magnetic field and coupling errors, and the case with a $\delta h_z = 10^{-3}J$ constant magnetic field in the Z direction, a NNN coupling $J_{13} = J_{12}/8$ and a 1% error on the relative magnitude J_{12}/J_{23}. The diabatic error in both cases is of the order 10^{-3}. We plot in Fig. 2.2 (a) the energy splitting Γ between $|\Psi_0\rangle$ and $|\Psi_1\rangle$ as a function of N, in units of $J = 1$, computed numerically for $\delta h_z = 10^{-3}J$ and a 1% error on the relative magnitude J_{12}/J_{23}. The scaling is exponential, as expected. For $N = 3$, we have $\Gamma \simeq 2 \times 10^{-9}J$, i.e., a negligible dephasing error. Thus, the qubit encoding will in principle work already for 3 ions, which is feasible with current technology.

We remark that the presence of a NNN coupling does not affect the protocol for a 3 ion setup. A spurious coupling J_{13} between the first and the third ions does not modify the protocol in terms of ground subspace (the ground subspace span$\{|\Psi_0\rangle, |\Psi_1\rangle\}$ stays the same), in terms of splitting Γ (in presence of a J_{13} the energies of $|\Psi_0\rangle$ and $|\Psi_1\rangle$ only show a coherent down shift) and in terms of local operations upon the qubit. Thus even by addressing the three ions with one bichromatic laser is sufficient to implement the model [65]. Nevertheless, the Hamiltonian free of NNN coupling for three sites can be obtained by using different detuned lasers, as shown in [71].

To show the subspace topological protection of the degenerate ground state $\{|\Psi_0\rangle, |\Psi_1\rangle\}$ with respect to coupling to outer states, we plot in Fig. 6.2 (b) the survival probability $|\langle\Psi_0|\psi(t)\rangle|^2$ for the evolved state $|\psi(t)\rangle$ from $|\Psi_0\rangle$ under the dynamics of Hamiltonian (2.3) (solid) or without it (dashed) with a constant magnetic field $\delta h_z \sim 10^{-3}J$ along the Z axis for $N = 3$. This is the kind of local operators that couple span$\{|\Psi_0\rangle, |\Psi_1\rangle\}$ with outer states. It is clearly appreciated that the survival probability inside the subspace is significantly increased upon evolution with (2.3). We remark that this is the main fundamental decoherence source in most experimental trapped ion setups [14], with coherence lifetimes of about 30 ms. We have that states $|\Psi_0\rangle$, $|\Psi_1\rangle$ will couple to each other or to outer states only through higher-order processes in perturbation theory. The largest contribution to decoherence is at most of order $\sim \delta h_z^2/\Delta_g$. Here δh_z is the average local magnetic field perturbation, that we take, as in the numerical simulation, to be $10^{-3}J$, and $\Delta_g = 2J$ is the gap between the topological ground states $|\Psi_0\rangle, |\Psi_1\rangle$ and the excited states. For this we have assumed that these spurious magnetic fields change in time much more slowly than the frequency of the gap. Accordingly, the effective Rabi frequency of the error is about $5 \times 10^{-4}\delta h_z$, i.e., several orders of magnitude reduced with respect to the case without topological protection [without evolution by (2.3)], that is of order δh_z. We point out that, in the long time limit, other sources of error will dominate on the decoherence of the system. The choice for the optimal size of the ion array, in which one encodes the topological qubit, will depend on the type of errors and parameter control of the particular experimental setup. Indeed, while for shorter chains one has less errors due to spontaneous emission, for longer chains the realistic ground state energy splitting between the qubit basis states will be smaller. For a three-ion array, considering that motional heating rates in trapped ions can be of a few phonons per second and spontaneous emission lifetimes of more than one second [39], with this proposal one may improve coherence lifetimes by more than one order of magnitude with current technology.

Chapter 3

Interacting fermion lattice models in trapped ions

3.1 Introduction

In this Chapter, we propose a quantum algorithm for the simulation of the dynamics of fermionic systems, specifically designed for trapped-ion systems. The use of collective ion gates allows for the efficiency of the method presented here with respect to single and two-qubit gates protocols. The numerical simulation of fermionic systems is, in general, a hard problem due to the huge increase of the Hilbert space dimension with the number of modes [2, 72]. Using customized numerical methods as quantum Monte Carlo is not always possible due to the well-known sign problem [73, 74]. Quantum simulations appear as a tool that will allow us to compute the time evolution of free and interacting fermion lattice theories with minimal experimental resources. This will be helpful in performing a wide range of condensed matter calculations, including those related with many-body interactions as the Kondo [75], Fermi-Hubbard [76], or Fröhlich [77] Hamiltonians. Furthermore, quantum simulations will allow us to reproduce the complete dynamics of these systems, avoiding mean field approximations as Hartree-Fock to simplify nonlinear interactions [78].

In this Chapter, we propose a method of realizing the quantum simulation of many-body fermionic lattice models for N fermionic modes in trapped ions. Our method can be described in three steps. Firstly, we map the set of N fermionic modes, via the Jordan-Wigner transformation [63], to a set of N nonlocal spin operators. The second step consists in decomposing the total unitary evolution via Trotter expansion [24, 79, 80] in terms of a product of exponentials associated to each nonlocal spin operator appearing in the Hamiltonian. Finally, we implement each of these exponentials in polynomial time on a set of N two-level trapped ions with a reduced number of laser pulses [56, 70]. These three steps yield an efficient protocol that employs only polynomial resources. Our method can simulate highly nonlinear and long-range interactions in arbitrary spatial dimensions, applying the Jordan-Wigner transformation without the usual restriction of a reduced number of neighbors, and without the need of auxiliary virtual Majorana fermions [81]. This is due to the fact that the dynamics associated with the nonlocal spin operators, containing a large number of Pauli matrices, can still be efficiently implemented. The proposed protocol opens the possibility to simulate a wide range of interesting condensed-matter and high-energy physics fermionic systems for a large number of particles. This includes the calculation of time evolutions and ground state computations. For a number of particles above ~ 30, which is foreseeable in the near future, one could already simulate fermionic systems that are intractable for classical computers.

3.2 Digital quantum simulation of fermionic dynamics

We consider the quantum simulation of the dynamics associated with the general Hamiltonian

$$H = \sum_{n=2}^{\alpha} \Bigg[\sum_{i_1 \ldots i_n = 1}^{N} g_{i_1 \ldots i_n} c_{i_1} \cdots\ c_{i_n} + \text{H.c.} \Bigg], \tag{3.1}$$

where c_{i_k} has to be chosen as one of the fermionic operators b_{i_k}, $b^\dagger_{i_k}$, that obey the anticommutation rule $\{b_{i_k}, b^\dagger_{i_{k'}}\} = \delta_{i_k, i_{k'}}$, N is the number of fermionic modes, and α is the highest order of the many-body interaction.

Our protocol consists of three steps, gathering techniques that have not been previously considered for quantum simulators of fermionic lattice models.

i) Jordan-Wigner mapping.– This technique establishes a correspondence between a set of fermionic operators and a set of spin operators, transforming a local Hamiltonian of fermions onto a nonlocal Hamiltonian of spins. Only in one spatial dimension, and for couplings extended to a reduced number of neighbors, the correspondence is from a local model to a similar one [63]. The operators $b_{i_k}, b^\dagger_{i_k}$ can always be mapped to products of Pauli matrices, i.e., nonlocal spin operators, using the Jordan-Wigner transformation $b^\dagger_k = I_N \otimes I_{N-1} \otimes \ldots \otimes \sigma^+_k \otimes \sigma^z_{k-1} \otimes \ldots \otimes \sigma^z_1$, and $b_k = (b^\dagger_k)^\dagger$.

ii) Trotter decomposition of the total Hamiltonian.– Our second step consists in using standard Trotter techniques to decompose the total evolution operator in terms of a product of evolution operators associated to each nonlocal spin operator. We prove below that these evolution operators can be implemented efficiently.

iii) Implementation of nonlocal spin operators in trapped ions.– The exponentials of each nonlocal spin operator are efficiently implementable, given that their exponents consist of tensor products of k Pauli matrices. Each of these exponentials can be implemented, for arbitrary k and up to local rotations, with a Mølmer-Sørensen gate [13] upon k ions, one local gate upon one of the ions, and the inverse Mølmer-Sørensen gate [70]. This step can be summarized as

$$\begin{aligned} \mathcal{U} &= \mathcal{U}_{\mathrm{MS}}(-\pi/2,0)\mathcal{U}_{\sigma_z}(\phi)\mathcal{U}_{\mathrm{MS}}(\pi/2,0) \\ &= \exp\left[i\phi\ \sigma_1^z\otimes\sigma_2^x\otimes\sigma_3^x\otimes\cdots\otimes\sigma_k^x\right], \end{aligned} \tag{3.2}$$

where $\mathcal{U}_{\mathrm{MS}}(\theta,\phi) = \exp[-i\theta(\cos\phi S_x + \sin\phi S_y)^2/4]$, $S_{x,y} = \sum_{i=1}^{k}\sigma_i^{x,y}$ and $\mathcal{U}_{\sigma_z}(\phi) = \exp(i\phi'\sigma_1^z)$ for odd k, where $\phi' = \phi$ for $k = 4n+1$, and $\phi' = -\phi$ for $k = 4n-1$, with positive integer n. For even k, $\mathcal{U}_{\sigma_z}(\phi)$ would be substituted by $\mathcal{U}_{\sigma_y}(\phi) = \exp(i\phi'\sigma_1^y)$, where $\phi' = \phi$ for $k = 4n$, and $\phi' = -\phi$ for $k = 4n-2$, with positive integer n. In order to obtain directly a coupling composed of σ^y matrices times a σ^z, one may apply a similar approach with different Mølmer-Sørensen gates according to

$$\begin{aligned} \mathcal{U} &= \mathcal{U}_{\mathrm{MS}}(-\pi/2,\pi/2)\mathcal{U}_{\sigma}(\phi)\mathcal{U}_{\mathrm{MS}}(\pi/2,\pi/2) \\ &= \exp\left[i\phi\ \sigma_1^z\otimes\sigma_2^y\otimes\sigma_3^y\otimes\cdots\otimes\sigma_k^y\right], \end{aligned} \tag{3.3}$$

where the local $\mathcal{U}_{\sigma}(\phi)$ gate is $\exp(i\phi'\sigma_1^z)$ for odd k, where $\phi' = \phi$ for $k = 4n+1$, and $\phi' = -\phi$ for $k = 4n-1$, with positive integer n. For even k, the local gate is $\exp(i\phi'\sigma_1^x)$ where $\phi' = \phi$ for $k = 4n-2$, and $\phi' = -\phi$ for $k = 4n$, with positive integer n. Note that local rotations acting on each ion give rise to any tensor product of Pauli matrices $\sigma_k^{x,y,z}$. The coupling constant in each nonlocal spin term of the simulated Hamiltonian (3.1) will be related to ϕ through $\phi = -gt$, where g is a generic coupling strength and t is the corresponding gate time.

The three steps of our protocol amounts to an efficient method for simulating fermionic models with long-range couplings in arbitrary dimensions with trapped ions.

Note that for bounded Hamiltonians, the Trotter expansion associated with the exponential of the polynomial sum of efficiently implementable nonlocal terms is also efficient [24, 79, 80], i.e., it only requires polynomial resources [1] . This includes most fermionic models in condensed-matter and high-energy physics, some of which we consider below. This includes most fermionic models in condensed-matter and high-energy physics, some of which we consider below.

---

[1] See Section 3.6 in this Chapter.

3.3 Fermionic models in condensed matter

Kondo model.– The long debated Kondo Hamiltonian provides a variety of interesting features in different systems, as the minimum in the resistivity at low temperatures [82]. With the proposed method, we can simulate Kondo Hamiltonians [75], modelling the interaction of a Fermi sea of electrons with several magnetic impurities at positions R_j,

$$\begin{aligned} H &= \sum_{p\sigma} \epsilon_p b^\dagger_{p\sigma} b_{p\sigma} - J \sum_{pp'j} e^{iR_j\cdot(p-p')}[(b^\dagger_{p\uparrow} b_{p'\uparrow} - b^\dagger_{p\downarrow} b_{p'\downarrow})\sigma^z_j \\ & \quad + b^\dagger_{p\uparrow} b_{p'\downarrow}\sigma^-_j + b^\dagger_{p\downarrow} b_{p'\uparrow}\sigma^+_j]. \end{aligned} \tag{3.4}$$

Here, $\sigma = \uparrow, \downarrow$ is the spin of the electron, $b_{p,p'\uparrow}(b^\dagger_{p,p'\uparrow})$ is the annihilation(creation) operator for an electron with respective momentum p or p' and spin up, $\sigma^+_j(\sigma^-_j)$ is the impurity raising(lowering) spin operator, ϵ_p is the energy of the kinetic electronic Hamiltonian and J is the electron-impurity coupling. Notice that, e.g., the operators $b^\dagger_{p\uparrow} b_{p'\downarrow}\sigma^-_j$ can be now mapped to a sum of products of Pauli matrices, leading to an efficient implementation.

Fermi-Hubbard model.– The Fermi-Hubbard Hamiltonian [76] takes into account a range of effects in condensed-matter physics, as the Mott transition, and is also believed to be relevant in high-T_c superconductivity. It takes the form

$$H = w \sum_{\delta i \sigma} b^\dagger_{i\sigma} b_{i+\delta\sigma} + U \sum_j b^\dagger_{j\uparrow} b_{j\uparrow} b^\dagger_{j\downarrow} b_{j\downarrow}, \tag{3.5}$$

where the first fermionic operator subindex refers to the lattice site and the second to the spin, w is the hopping energy, U is the onsite Coulomb repulsion and one usually makes the tight-binding approximation $\delta = \pm 1$. Notice that our method is general and extends the hopping terms to arbitrarily distant pairs of electrons. The last term contains the product of four fermionic operators, allowing for efficient implementation.

We could as well implement the coupling of arbitrary products of fermionic operators, similarly to Eq. (3.1), to linear sum of bosonic operators,

$$H = \sum_{n=2}^{\alpha} \left[\sum_{i_1 \ldots i_n = 1}^{N} g_{i_1 \ldots i_n} c_{i_1} \cdots \, c_{i_n} \sum_j g_j (a_j + a^\dagger_j) + \text{H.c.} \right]. \tag{3.6}$$

The bosonic operators a_j can be implemented with the vibrational modes of the ion chain. One would now consider the same gate sequence as in Eq. (3.2) but replacing

$\mathcal{U}_{\sigma_z}(\phi) = \exp(i\phi'\sigma^z)$ with $\mathcal{U}_{\sigma_z,a}(\phi) = \exp[i\phi'\sigma^z \sum_j g_j(a_j + a_j^\dagger)]$. The latter can be implemented by using a red and a blue sideband interactions for each of the a_j modes in the context of standard trapped-ion technology [8].

Fröhlich model.– The Fröhlich Hamiltonian [77] models the interaction of electrons with phonons,

$$H = \sum_p \frac{p^2}{2m} b_p^\dagger b_p + \omega_0 \sum_q a_q^\dagger a_q + \sum_{qp} M(q) b_{p+q}^\dagger b_p (a_q + a_{-q}^\dagger), \tag{3.7}$$

with $M(q)$ being the electron-phonon coupling. Here, b_p is the electron annihilation operator that destroys an electron with momentum p, a_q is the phonon annihilation operator with momentum q, ω_0 is the phonon frequency, and m is the electron mass. The last term contains the product $b_{p+q}^\dagger b_p(a_q + a_q^\dagger)$, whose dynamics can be implemented with our technique above according to Eq. (3.6). We can simulate this kind of Hamiltonians in order to recover the polaron physics, a critical open issue for the deep understanding of correlated electrons in solids [83].

3.4 The n-dimensional case

One of the main appeals of our method is that the efficient encoding of fermionic models in a lattice with arbitrarily long-range couplings is feasible. This also means that we can apply the Jordan-Wigner transformation for two and three spatial dimensions, not just for one, without employing additional virtual Majorana fermions [81]. All this is due to the fact that the fermionic operators are encoded in nonlocal spin operators whose dynamics are efficiently implementable. Thus, the mapped spin Hamiltonians are highly nonlocal but their evolution is efficiently realizable.

In order to show this, we plot in Fig. 6.1 the mapping of a solid-state 3D fermionic system onto an ion string. As opposite to the nearest-neighbor tunneling coupling between fermions 1 and 2, which is local, the couplings between 1 and 4, and between 1 and 10, are nonlocal due to the Jordan-Wigner transformation, see yellow lines in Fig. 6.1a. Nevertheless, we can implement them in an efficient way. In Fig. 6.1b we show the set of quantum gates needed to the implementation of the tunneling coupling $b_1^\dagger b_{10} + b_{10}^\dagger b_1 = \sigma_1^x \otimes \sigma_2^z \otimes \sigma_3^z \otimes \ldots \otimes \sigma_9^z \otimes \sigma_{10}^x + \sigma_1^y \otimes \sigma_2^z \otimes \sigma_3^z \otimes \ldots \otimes \sigma_9^z \otimes \sigma_{10}^y$ in trapped ions. This highly nonlocal coupling is a global unitary of $2^{10} \times 2^{10}$ dimensions. In the general case, it would require a number of elementary gates of $2^{20} \simeq 10^6$ [24]. With our method, the number of gates can be as small as 10 per Trotter step, consisting of Mølmer-Sørensen

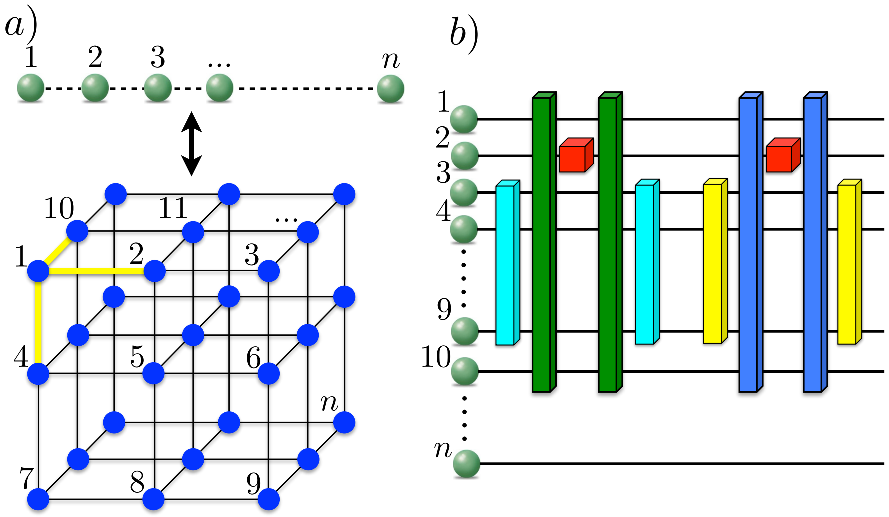

FIGURE 3.1: (a) Mapping of a fermionic Hamiltonian onto an ion string. The couplings between fermions 1 and 4 (resp., 1 and 10) are nonlocal when applying the Jordan-Wigner transformation. (b) Efficient mapping of the tunneling coupling $b_1^\dagger b_{10} + b_{10}^\dagger b_1$ in trapped ions. This highly nonlocal coupling can be implemented with Mølmer-Sørensen gates (dark blue and green), local $\exp(i\phi' \sigma_2^y)$ gates (red), $\exp[\pm i(\pi/4)\sum_i \sigma_i^y]$ (yellow) and $\exp[\pm i(\pi/4)\sum_i \sigma_i^x]$ (cyan) gates.

gates (dark blue and green), local $\exp(i\phi' \sigma_2^y)$ gates (red), $\exp[\pm i(\pi/4)\sum_i \sigma_i^y]$ (yellow) and $\exp[\pm i(\pi/4)\sum_i \sigma_i^x]$ (cyan) gates [2].

3.5 Numerical simulations

In order to compare the efficiency of the Trotter decomposition with the exact case, we have realized numerical simulations of the Fermi-Hubbard Hamiltonian, Eq. (3.5), for different levels of Trotter expansion and for the exact diagonalization case. We have considered the case of three lattice sites, with six modes (two spins per site), to be simulated with six two-level trapped ions. The resulting Hamiltonian is

$$\begin{aligned} H &= w(b_{1\uparrow}^\dagger b_{2\uparrow} + b_{1\downarrow}^\dagger b_{2\downarrow} + b_{2\uparrow}^\dagger b_{3\uparrow} + b_{2\downarrow}^\dagger b_{3\downarrow} + \text{H.c.}) \\ &+ U(b_{1\uparrow}^\dagger b_{1\uparrow} b_{1\downarrow}^\dagger b_{1\downarrow} + b_{2\uparrow}^\dagger b_{2\uparrow} b_{2\downarrow}^\dagger b_{2\downarrow} + b_{3\uparrow}^\dagger b_{3\uparrow} b_{3\downarrow}^\dagger b_{3\downarrow}). \end{aligned} \tag{3.8}$$

Notice that the number of terms to be implemented scales linearly with the number of modes, $5N/2 - 4$ (11 in this case, for $N = 6$). At the same time, the nonlocal gates upon several ions are efficiently implementable with few lasers, such that the number of gates in each term of the Hamiltonian is, in the worst case, linear in the number of modes, and in many cases just constant. In this particular example the total number of gates per Trotter step is of 33, i.e., on average 3 gates per Hamiltonian term, which is very

---

[2] See Appendix **??** for more detailed example

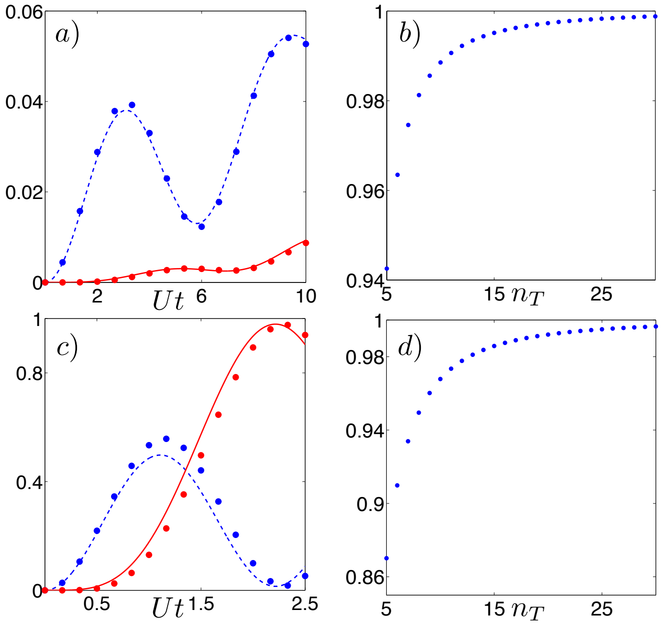

FIGURE 3.2: (a) $\langle b^\dagger_{2\downarrow} b_{2\downarrow}\rangle(t)$ (dashed, blue), and $\langle b^\dagger_{3\uparrow} b_{3\uparrow}\rangle(t)$ (solid, red) as a function of Ut, for a number of Trotter steps $n_T = 15$, and (b) fidelity $|\langle\psi(t_F)|\psi(t_F)_T\rangle|^2$ as a function of n_T, for $Ut_F = 10$, where $|\psi(t)\rangle$ is the state evolved with exact diagonalization, and $|\psi(t)_T\rangle$ is the Trotter-evolved state, for $|\psi(0)\rangle = |\psi_T(0)\rangle = b^\dagger_{1\uparrow} b^\dagger_{1\downarrow}|0\rangle$, for $|w|/U = 0.1$. (c) $\langle b^\dagger_{2\downarrow} b_{2\downarrow}\rangle(t)$ (dashed, blue), and $\langle b^\dagger_{3\uparrow} b_{3\uparrow}\rangle(t)$ (solid, red), for $n_T = 15$, and (d) fidelity $|\langle\psi(t_F)|\psi(t_F)_T\rangle|^2$, for $Ut_F = 2.5$, where $|\psi(t)\rangle$ is the state evolved with exact diagonalization, and $|\psi(t)_T\rangle$ is the Trotter-evolved state, for $|\psi(0)\rangle = |\psi_T(0)\rangle = b^\dagger_{1\uparrow} b^\dagger_{1\downarrow}|0\rangle$, for $|w|/U = 4$. In (a) and (c), the lines are obtained with exact diagonalization and the dots with Trotter expansion.

efficient. This is due to the specific structure of this Hamiltonian, that avoids the need to apply additional local rotations.

In Figs. 6.2a and 6.2c, we plot the average number of excitations for mode $b_{2\downarrow}$ (dashed, blue) and $b_{3\uparrow}$ (solid, red) for different parameters, showing the good convergence of the Trotter method. Here, the lines are obtained with exact diagonalization and the dots with Trotter expansion. For additional figures with larger number of Trotter steps, see Section 3.6 in this Chapter. In Figs. 6.2b and 6.2d, we include the fidelity $|\langle\psi(t_F)|\psi(t_F)_T\rangle|^2$ as a function of the number of Trotter steps n_T, where $|\psi(t)\rangle$ is the state evolved with exact diagonalization, and $|\psi(t)_T\rangle$ is the Trotter-evolved state, for $|\psi(0)\rangle = |\psi_T(0)\rangle = b^\dagger_{1\uparrow} b^\dagger_{1\downarrow}|0\rangle$, and for different parameters. Notice that the fidelity of the Trotter expansion goes to 1 with the number of Trotter steps n_T, and for $n_T = 10$ it is 0.99 and 0.97, respectively.

With current technology, more than 100 gates have been realized in a single experiment [25]. Indeed, without error correction, one would expect the realization of more than thousand gates in the near future [84]. This will allow, for $n_T = 10$ Trotter steps, the implementation of hundreds of gates per step, giving us the possibility to simulate a wide variety of fermionic models. In a possible experiment, one could consider, e.g., strings of Ca^+ ions controlled with lasers. The spin degrees of freedom can be encoded in long-lived electronic states of the ions [16, 23, 25, 54–56, 85]. Optimal state initialization via optical pumping and high-fidelity detection through resonance fluorescence can be easily performed.

3.6 Analysis of Trotter errors

In this Section, we show that the resources needed in our protocol, including number of elementary gates and time scaling, are polynomial on the Trotter error, the total time simulated, and the total size of the system, in terms of the number of fermionic modes.

The Trotter expansion is a useful tool to express the evolution operator of a Hamiltonian that can be written as a sum of efficiently-implementable Hamiltonians, in terms of a certain product of the operators associated to each of these individual Hamiltonians. More specifically, if the Hamiltonian H can be written as a sum of m terms, where m is polynomial in N, $H=\sum_{j=1}^{m} H_j$, then the standard Trotter expansion reads [24, 79, 80],

$$e^{-iHt} = (\prod_{j=1}^{m} e^{-iH_j t/n_T})^{n_T} + \mathcal{O}[1/n_T]. \tag{3.9}$$

Accordingly, by making n_T very large, the error can be made as small as possible.

There are more sophisticated, higher order expansions so called Lie-Trotter-Suzuki methods [86–88], that have a better scaling of the errors. Here, we will focus on time-independent Hamiltonians whose evolution operator is expanded in terms of a k-th order Lie-Trotter-Suzuki integrator. We will follow the formalism and error analysis of Ref. [80]. In this reference it is shown that decompositions of $\mathcal{U}=\exp(-iHt)$, where $H=\sum_{j=1}^{m} H_j$, can be carried out in the general form

$$\tilde{\mathcal{U}} = \prod_{l=1}^{N_{\mathrm{e}}} e^{-iH_{j_l} t_l}, \tag{3.10}$$

with error $||\mathcal{U}-\tilde{\mathcal{U}}||<\epsilon$. Here, the total number of gates needed, N_{e}, scales in the error ϵ, the total evolution time t, and the norm of the Hamiltonian H, $||H||$, where $||.||$ is the 2-norm, in the form [80]

$$N_{\mathrm{e}} \leq m5^{2k}(m||H||t)^{1+1/2k}/\epsilon^{1/2k}, \tag{3.11}$$

provided $\epsilon \leq 1 \leq 2m5^{k-1}||H||t$.

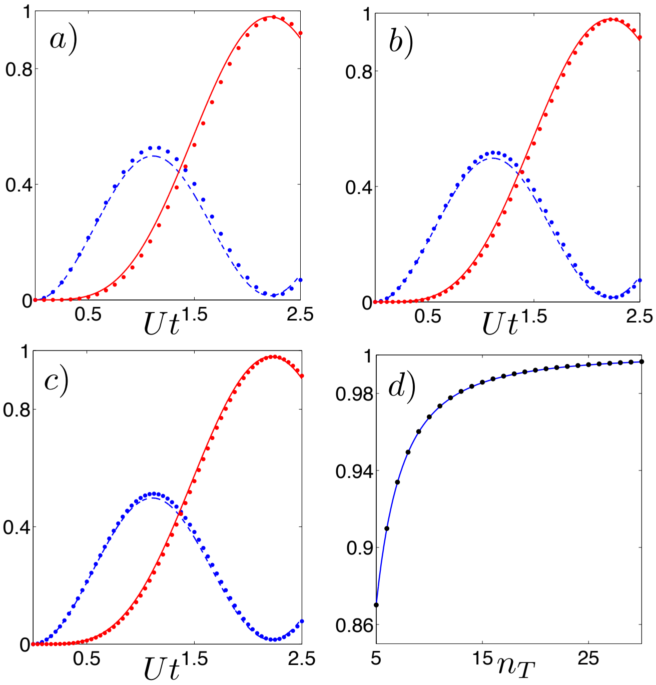

FIGURE 3.3: We plot $\langle b^\dagger_{2\downarrow} b_{2\downarrow}\rangle(t)$ (dashed, blue), and $\langle b^\dagger_{3\uparrow} b_{3\uparrow}\rangle(t)$ (solid, red) as a function of Ut, for $|\psi(0)\rangle = |\psi_T(0)\rangle = b^\dagger_{1\uparrow} b^\dagger_{1\downarrow}|0\rangle$, $|w|/U = 4$, and a number of Trotter steps $n_T = 30$ (a), 45 (b), and 60 (c). In (a), (b), and (c) the lines are obtained with exact diagonalization and the dots are obtained with Trotter expansion. We also plot (d) the fidelity $|\langle\psi(t_F)|\psi(t_F)_T\rangle|^2$ as a function of n_T, for $Ut_F = 2.5$, where $|\psi(t)\rangle$ is the state evolved with exact diagonalization, and $|\psi(t)_T\rangle$ is the Trotter-evolved state, for $|\psi(0)\rangle = |\psi_T(0)\rangle = b^\dagger_{1\uparrow} b^\dagger_{1\downarrow}|0\rangle$, and for $|w|/U = 4$. We show the numerical results with Trotter (dots) and a fit to the function $1 - C/n_T^2$ (line), where C is a free parameter.

Notice that in all fermionic Hamiltonians we are considering, we have i) a polynomial number of nonlocal spin operators, i.e., m is polynomial in N, the total number of fermionic modes. ii) each H_j is always of the form of a product of arbitrary number of Pauli matrices times a coupling h_j, such that its norm $||H_j|| = h_j$, given that the 2-norm of a product of arbitrary number of Pauli matrices is always 1. iii) the total norm of H is bounded by $||H|| \leq \sum_{j=1}^m ||H_j|| = \sum_{j=1}^m h_j \leq m h_j^{\max}$, where $h_j^{\max}$ is the maximum among all $h_j' s$. Thus, $||H||$ is polynomial in m, and in consecuence, also in N.

Accordingly, we have shown that the scaling of the number of elementary gates needed in our expansion, is polynomial (more specifically, a power law) in ϵ, t, and N, such that our method for implementing arbitrary fermionic Hamiltonians that occur in nature is efficient.

We plot Figs. 3.3a, b, and c, in order to analyze the convergence of Trotter methods to the exact diagonalization case when increasing the number of Trotter steps n_T, and comparing with Fig. 6.2 in the previous Section (for which $n_T = 15$). These three figures clearly show the fast convergence for a linear increase in n_T.

In Fig. 3.3d, we plot the fidelity $|\langle\psi(t_F)|\psi(t_F)_T\rangle|^2$ as a function of n_T, for $Ut_F = 2.5$, where $|\psi(t)\rangle$ is the state evolved with exact diagonalization, and $|\psi(t)_T\rangle$ is the Trotter-evolved state, for $|\psi(0)\rangle = |\psi_T(0)\rangle = b^\dagger_{1\uparrow}b^\dagger_{1\downarrow}|0\rangle$, and for $|w|/U = 4$. We show the numerical results with Trotter (dots) and a fit to the function $1 - C/n_T^2$ (line), where C is a free parameter. This curve has a perfect agreement with the Trotter numerics. Thus, the error goes to zero polynomially in n_T, as expected.

Chapter 4

Quantum simulation of the Holstein model

4.1 Introduction

In this Chapter, we will extend the protocol presented in Chapter 3, in order to deal with the digital simulation of coupled bosonic-fermionic systems. These systems are naturally described by unbounded Hamiltonians and, as we will show, the quantum simulation of such systems may have some subtleties in the convergence of the digital approximation, which are not usually addressed in the literature of quantum simulation protocols.

Strongly correlated quantum many body systems represent a challenge to both computational and analytic methods. Among them, correlated fermionic-bosonic models are of critical relevance. The importance of correlation between electrons and ion vibrations has been proven for a large number of condensed-matter systems [89]. Their role in high-temperature superconductors, as fullerides and cuprates, is still debated [90–92]. In solid state systems, the correlation between the presence of electrons in a lattice and deformations of the latter can result in the formation of polarons: electrons and phonons can no longer be considered as stand-alone particles. Depending on the strength of the electron-phonon couplings, the cloud of lattice displacements surrounding the electron can have different sizes. For strong couplings, the electrons can be trapped, with remarkable changes of global properties [93]. The Holstein model [94] has been proved to naturally describe the strong coupling case. This model has been recently addressed by heavy numerical simulations [95] and classical analog simulations for a reduced number of sites [96]. Perturbation methods based on the Lang-Firsov approximations [97], valid in the strong coupling limit, are known since long times. The dimensionality of the underlying lattice also raises critical features [98]. While involving a lot of efforts, the full and complete comprehension of the electron-phonon correlations is still an open problem. From a quantum mechanics point of view, when considering creation of phonons, even with few electron sites, the size of the simulated Hilbert space can dramatically grow. The quantum simulation of such a complex dynamics could represent an important step forward in the description of condensed matter systems.

Trapped-ion systems are among the most controllable quantum systems. They offer remarkable computational power to perform quantum simulations exponentially faster than their classical counterparts [4, 16, 17, 19–23, 53–55, 57, 58, 99–101].

We propose the implementation of the Holstein Hamiltonian in a chain of trapped ions, using digital-analog approximation methods, in which the fermionic part is digitized and the bosonic part is analog and provided naturally by the phonons. First, we address the problem of simulating unbounded Hamiltonians with digital-analog protocols. Then, we provide a convenient decomposition of the Holstein Hamiltonian, in that each step can be implemented in a trapped-ion setup. We discuss a possible experimental implementation, testing the whole protocol with numerical integrations of the Schrödinger equation. We show how critical observables, as electron-phonon correlations, can be retrieved from the trapped ion setup, leading to an estimation of the polaron size.

4.2 Trotter decomposition

It is known that the dynamics of a quantum state under the action of a Hamiltonian H can be recovered by using combined fractal-stroboscopic symmetric decompositions [40, 80]. In most practical cases, one can assume a fractal depth of one. This will be the case through all the rest of our analysis. With these techniques, the target Hamiltonian H is decomposed in a set of m terms: $H = \sum_{i=1}^{m} H_i$. Then, the *symmetric* decomposition for the unitary operator encoding the dynamics of Hamiltonian H reads

$$U_r(t) = \left(\prod_{i=1}^{m} e^{-\frac{iH_i t}{2r}} \prod_{i=m}^{1} e^{-\frac{iH_i t}{2r}} \right)^r . \tag{4.1}$$

Here r is the degree of approximation in terms of Trotter steps. It has been shown [80] that, using symmetric Suzuki fractal decompositions, the number of gates needed to approximate the exact time evolution of the quantum state grows with the norm of the simulated Hamiltonian. Therefore, it is a natural problem to think of a quantum simulation involving particle generation, in particular of bosons, whose number can grow, in principle, indefinitely. However, in the standard approach to these problems, the dynamics of a bosonic Hilbert space can be recovered by truncating at a certain point of the number of possible bosonic excitations, see Appendix A. Thus, the number of gates needed to achieve a certain fidelity for the simulated quantum state grows as more bosonic excitations are created.

The Holstein Hamiltonian [94], of a chain of N sites (in the following $\hbar = 1$), reads

$$H = -h\sum_{i=1}^{N-1}(c_i^\dagger c_{i+1} + h.c.) + g\sum_{i=1}^{N}(b_i + b_i^\dagger)n_i + \omega_0\sum_{i=1}^{N} b_i^\dagger b_i. \tag{4.2}$$

Here, $c_i(c_i^\dagger)$ is the annihilation (creation) operator in the electron site i, and $b_i(b_i^\dagger)$ is the phonon annihilation (creation) operator on the site i; $n_i = c_i^\dagger c_i$ is the electronic occupation number operator. The parameters h, g and ω_0 stand respectively for a nearest-neighbor (NN) site hopping for the electrons, electron-phonon coupling and free energy of the phonons. To encode the model in a trapped-ion chain, we first map the fermionic operators through the Jordan-Wigner transformation, $c_i \to \prod_{j=1}^{i-1}\sigma_j^z\sigma_i^-$ to tensor products of Pauli matrices. The mapped Hamiltonian describes now a coupled spin-boson system

$$\begin{aligned} H = h\sum_{i=1}^{N-1}(\sigma_i^+\sigma_{i+1}^- + h.c.) + \\ +g\sum_{i=1}^{N}(b_i + b_i^\dagger)\frac{(\sigma_i^z + 1)}{2} + \omega_0\sum_{i=1}^{N} b_i^\dagger b_i. \end{aligned} \tag{4.3}$$

The first term can be rewritten as $\frac{h}{2}\sum_{i=1}^{N}(\sigma_i^x\sigma_{i+1}^x + \sigma_i^y\sigma_{i+1}^y)$. We now decompose the Hamiltonian into three parts, $H = H_1 + H_2 + H_3$. The single steps read

$$\begin{aligned} H_1 &= \sum_{i=1}^{N-1}\frac{h}{2}\sigma_i^x\sigma_{i+1}^x + \frac{\omega_0}{3}\sum_{i=1}^{N} b_i^\dagger b_i, \\ H_2 &= \sum_{i=1}^{N-1}\frac{h}{2}\sigma_i^y\sigma_{i+1}^y + \frac{\omega_0}{3}\sum_{i=1}^{N} b_i^\dagger b_i, \\ H_3 &= \sum_{i=1}^{N} g(b_i + b_i^\dagger)\frac{(\sigma_i^z + 1)}{2} + \frac{\omega_0}{3}\sum_{i=1}^{N} b_i^\dagger b_i. \end{aligned} \tag{4.4}$$

According to Ref. [80], one can upper bound the number of gates N_g needed to achieve a simulation error smaller that ϵ, by giving an upper bound for the norm of H,

$$\begin{aligned} N_g &\leq 3\cdot 5^{2k}[3(|h|(N-1) + 2|g|N\sqrt{M-1} \\ &\quad +\omega_0 NM)t]^{1+\frac{1}{2k}}/\epsilon^{1/2k}. \end{aligned} \tag{4.5}$$

As mentioned before, the fractal depth k [40] can be set to one in most applications. Here, we show the dependence of the number of gates in the number of fermionic sites N,

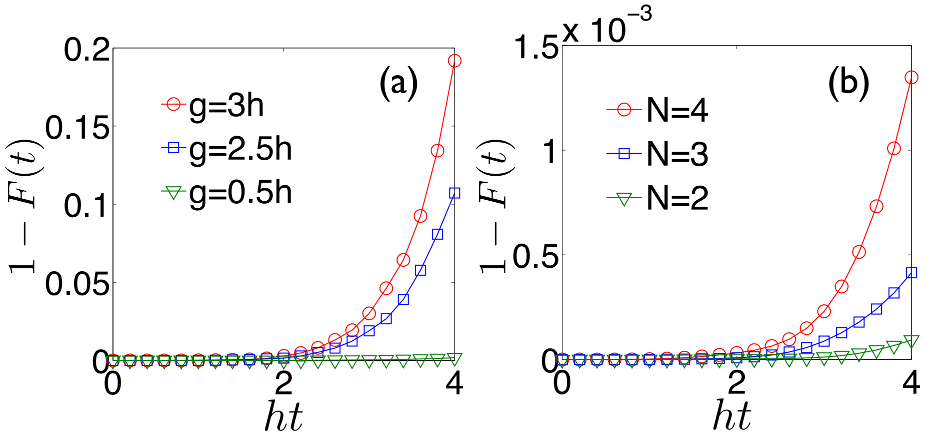

FIGURE 4.1: (a) Behavior of the fidelity loss $1-F(t)=1-|\langle\Psi_E(t)|\Psi_S(t)\rangle|^2$, for a two site configuration, as a function of the electron-phonon coupling strength g, for $\omega_0=h/4$. As the coupling g increases, more phonons are created, the Hilbert space describing the dynamics enlarges and the fidelity decreases for a fixed number of approximant gates ($r=10$ here). (b) Dependence of the fidelity loss in the number of sites. Here $g=0.3\ h$, $\omega_0=0.5\ h$, and ten symmetric steps are considered ($r=10$). The initial state of both plots corresponds to a configuration in which an electron is injected in the site $N/2$ (N even) or $(N+1)/2$ (N odd), and there are no phonons.

and on the truncation in the number of bosons M. As the number of created phonons increases, one needs a higher-level truncation, and a larger Hamiltonian norm. Nevertheless, this shows that we can efficiently simulate a $2^N\times(M+1)^N$ Hilbert space, i.e., with a number of gates that grows at most polynomially in N and M. To show the scaling of fidelities with the parameters considered, we plot in Fig. 4.1 the time dependence of the fidelity loss $1-F(t)=1-|\langle\Psi_E(t)|\Psi_S(t)\rangle|^2$ of the simulated wavefunction $|\Psi_S(t)\rangle$ versus the exact one $|\Psi_E(t)\rangle$ as a function of coupling g and of number of sites N. The particular decomposition has been chosen so that all terms in Eq. (4.4) can be implemented in a linear chain of trapped ions.

4.3 Proposal for ion-trap systems

We consider a set of $N+1$ trapped ions in a chain, in order to simulate N fermionic sites provided with Holstein interactions. The ions are bounded strongly in the radial direction, and confined longitudinally within a harmonic potential [102]. We define ν_i, $i=1,2,...N+1$, as the frequencies of the axial normal modes. We relate the ion normal mode energies with the dispersionless phonon energies in Eq. (4.2) via $\Delta_i=\nu_i-\frac{\omega_0}{3}$. The three Hamiltonian steps H_1, H_2 and H_3 are derived in the interaction picture with respect to

$$H_0=\sum_{i=1}^{N+1}\frac{\omega}{2}\sigma_i^z+\sum_{i=1}^{N}\Delta_i b_i^\dagger b_i+\nu_{N+1}b_{N+1}^\dagger b_{N+1}, \tag{4.6}$$

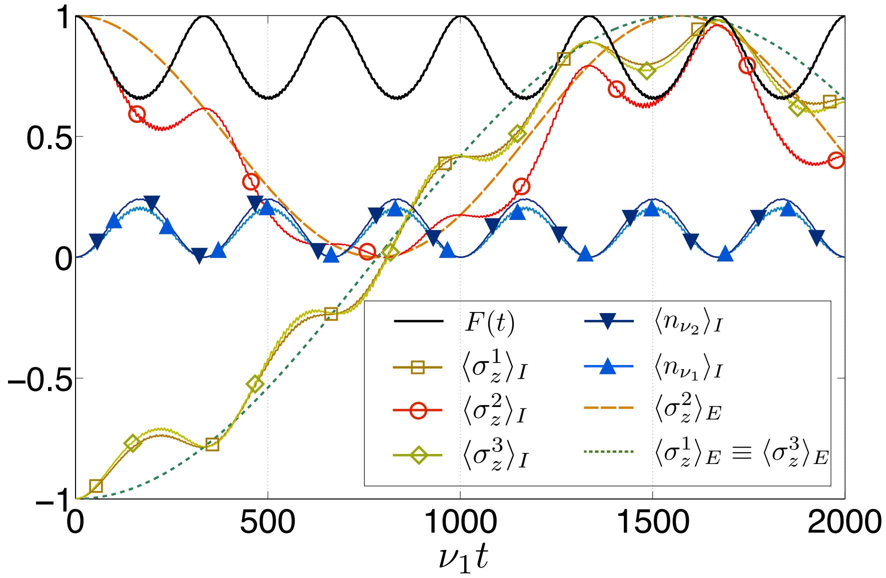

FIGURE 4.2: Dynamics for the $3+1$ ions configuration of the NN XX Hamiltonian. Dotted curves stand for $\langle\sigma_z^i\rangle_E$ for the exact dynamics, and solid curves stand for $\langle\sigma_z^i\rangle_I$ for realistic ion interactions ($i = 1, 2, 3$ for the first, second and third ion). The parameters are chosen in order to have maxima in the fidelity $F(t) = |\langle\Psi_E(t)|\Psi_I(t)\rangle|^2$ of ~ 0.995 (top black curve) at time steps of $\sim 333\ \nu_1 t$. These time steps can be chosen as Trotter steps.

where ω is the excitation energy of the individual ion taken as a two-level system, i.e., the carrier frequency. In this way, the free energies of N normal modes do not disappear in the interaction picture, and a flattered part of them is still present in order to recover the dispersionless phononic spectrum.

To simulate the dynamics associated to H_1 and H_2 of Eq. (4.4), one has to achieve a NN Ising coupling. The possibility of obtaining an Ising field in linear chains of trapped ions has been proposed and realized [16, 65]. However, in implementing NN interactions between more than two ions, one must be careful in designing an appropriate set of lasers and detunings in order to minimize the spurious non-nearest-neighbor (NNN) effects. To this extent, we have realized numerical simulations for a 3+1 ions setup, using one set of two pairs of counterpropagating lasers detuned close to the shifted center of mass (COM) shifted mode of frequency $\Delta_1 = \nu_1 - \omega_0/3$ to drive the first two ions (detunings $\pm\delta_1$), and another set of lasers detuned close to a second mode of frequency Δ_2, that in the case of 3+1 ions can be chosen as the breathing mode, addressing the second and the third ion (detunings $\pm\delta_2$). For a generic number of ions, Rabi frequencies Ω_i of the lasers driving the i-th and the $i+1$-th ions are chosen to achieve the desired strength in the Ising coupling, according to [65],

$$H_{NN} = \sum_{i=1}^{N-1} \Omega_i^2 \left[\left(\sum_{m=1}^{N} \frac{\eta_{i,m}\eta_{i+1,m}\Delta_m}{\delta_i^2 - \Delta_m^2} \right) + \frac{\eta_{i,N+1}\eta_{i+1,N+1}\nu_{N+1}}{\delta_i^2 - \nu_{N+1}^2} \right] \sigma_i^x \sigma_{i+1}^x . \tag{4.7}$$

In Fig. 4.2, the first and second ion are driven with two pairs of counterpropagating lasers with detuning close to the shifted COM mode ($\delta_1 = 1.0187\ \nu_1$ for $\omega_0 = h/4$). The Rabi frequencies are chosen properly in order to reach a NN interaction of $h/2 = 0.001\ \nu_1$. Lasers driving the second and the third ions are detuned close to the shifted breathing mode at $\nu_2 = 1.731\ \nu_1$ [102], with parameters $\delta_2 = 1.71196\ \nu_1$. Detunings are chosen to have a dynamics decoupled with respect to the phonons at time steps $\sim 333\ \nu t$ and a negligible NNN interaction. At these times, the ion spins match the exact value, phonons are detached from spins and the fidelity oscillation (top black curve) $F(t) = |\langle\Psi_E(t)|\Psi_I(t)\rangle|^2$ reaches maxima, with peaks of ~ 0.995.

The initial state, as in all our numerical simulations, except where specified, is chosen to mimic a configuration in which one electron is injected at the center of a one dimensional lattice provided with Holstein interactions. To this extent, all the spins are initialized in the opposite Z direction, except the one in site $N/2$, in case of even N, or $(N+1)/2$ in case of odd N. The spin of the last ion has to be initialized along the Z direction in order to be a passive ion with respect to the dynamics, according to the protocol for the implementation of H_3 given below. The vibrational modes are assumed to be initially cooled down to the ground state with resolved sideband cooling [8].

Notice that one can always implement a perfect NN coupling by using more stroboscopic steps. A possibility is to decompose the global NN into nearest-neighbor pairwise interactions. Another possibility is to design a counter, non-nearest-neighbor interaction step between pairs of non-nearest neighbor ions in order to eliminate the spurious NNN imperfections. Given that one has an unwanted $h_{i,j}\sigma_x^i\sigma_x^j$, one can add more Trotter steps to the protocol of the form $-h_{i,j}\sigma_x^i\sigma_x^j$ in order to have an Hamiltonian free of NNN couplings. The dynamics associated to the step with H_2 is implemented similarly to the one of H_1, with a different choice of the initial phases of the lasers, in order to achieve a YY interaction.

The Hamiltonian H_3 is realized as a combination of $2N$ red and blue detuned lasers with appropriate initial phases in order to recover a coupling of the i-th ion ($i = 1, ...N$) with the m_i-th normal (shifted) mode $\eta_{i,m_i}\Omega_i\sigma_x^i(b_{m_i}^\dagger + b_{m_i})$. The i-th ion is driven with red and blue detuned lasers to the m_i-th mode, establishing a one-to-one correspondence between the first N ions and the first N normal modes. Moreover, the last ion of the chain is driven by $2N$ lasers detuned in order to be coupled with the same modes of the ions in the chain. Two additional rotations of the spins of all ions around the Y axis are applied before and after coupling the spins to the phonons. They can be obtained by acting two times with a global beam upon all the $N+1$ ions at the same time. The

Hamiltonian describing this process is,

$$H_{e-p} = \sum_{i=1}^{N} (\Omega_i \eta_{i,m_i} \sigma_z^i + \Omega_{N+1,i} \eta_{N+1,m_i} \sigma_z^{N+1})(b_{m_i} + b_{m_i}^\dagger). \tag{4.8}$$

The Rabi frequencies of the lasers must be chosen according to $\Omega_i = g/2\eta_{i,m_i}$, $\Omega_{N+1,i} = g/2\eta_{N+1,m_i}$. If the last ion is initialized with the spin aligned along the Z axis and not addressed by spin flip gates during the simulation, the previous described gates result in the effective Hamiltonian on the *first N ions subspace*,

$$H_{e-p,N} = \sum_{i=1}^{N} g \frac{(\sigma_z^i + 1)}{2} (b_{m_i} + b_{m_i}^\dagger). \tag{4.9}$$

4.4 Digital quantum simulation analysis

In general, digital protocols are much sensitive to the state fidelity that one can achieve at the end of the digital step. According to the mathematical theory, increasing the number of steps will result in an increased fidelity on the final simulated state. However, if one has an error on a single step, increasing the number of gates will result in the accumulation of these errors. Thus on one hand the use of more accurate single gates is required, on the other hand one has to get a compromise between the increased fidelity due to the increased number of steps and the fidelity loss due to the accumulated single gate error.

To have a quantitative estimation of the fidelity loss with the dynamics of the full ion Hamiltonian, we have realized numerical integrations for the Schrödinger equation for $N = 2{+}1$ and $N = 3{+}1$ ion setups. We point out that we consider this reduced number of ions because of numerical computation restrictions, and to prove the feasibility of our model. In general our formalism may be straightforwardly extended to several ions. In Fig.4.3, a simulation for $r = 2$ and $r = 3$ symmetric Trotter steps is realized. The fidelity loss $1 - |\langle \Psi_E(t) | \Psi_S(t) \rangle|^2$ for the Trotter protocol with perfect gates, i.e., associated to Hamiltonians H_1, H_2 and H_3, is plotted against points of fidelity loss $1 - |\langle \Psi_E(t) | \Psi_I(t) \rangle|^2$ obtained with realistic trapped-ion gates including the full laser interactions are plotted at various times. As can be appreciated, the fidelity loss for the ion gates is only slightly larger than for the exact Trotter gates, showing the feasibility of the protocol with realistic trapped-ion interactions. The total simulation time has been chosen in order to remain under the decoherence time for the ions [14]. The frequency of the center of mass mode can be assumed to be $\nu_1 \simeq 2\pi \times 1$ MHz. The global rotation for the ion spins can be assumed to be done in 7 μs [25]. The number of global rotations is $4r$. The step for the red and blue sideband Hamiltonian can be performed in the same time as the

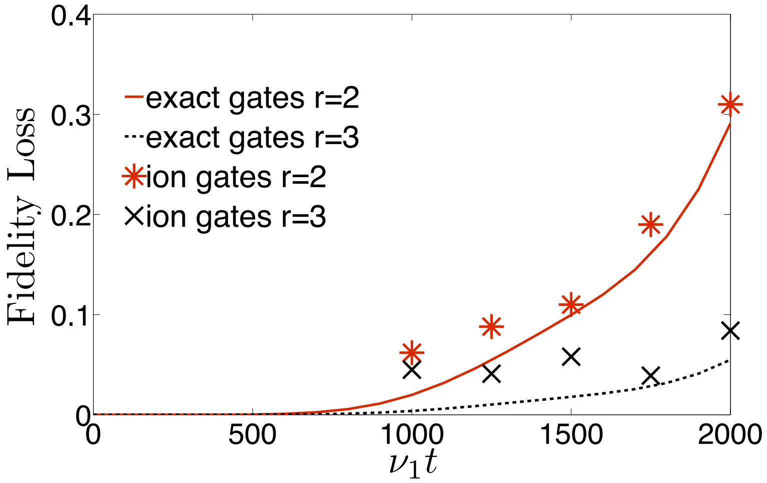

Figure 4.3: Fidelity loss for 3+1 ion configuration, involving Trotter simulation with perfect gates and realistic ion interactions, for two and three symmetric Trotter steps.

step for the NN XX gate (or even faster). Provided with these parameters, for a final simulated time of $2000/\nu_1 \sim 318\ \mu$s, the time spent for the simulation can be taken of ~ 1 ms. Given that typical heating rates in trapped ion experiments [25] are of about 1 phonon/s, we can assume that for the time of the proposed simulation heating will not be significant.

Tuning the coupling strength g by setting the Rabi frequencies of the red and blue detuned lasers to various values, one can measure the different correlations between electron and phonon displacement at distant sites,

$$\chi(i,j) = \langle \Psi(t) | c_i^\dagger c_i (b_j^\dagger + b_j) | \Psi(t) \rangle. \tag{4.10}$$

This will amounts to a signature of the polaron size [93]. Ranging from small to large g will lead to a measure of the crossover between large/small polaron. Notice that these correlations are mapped in our ion setup onto

$$\chi(i,j) = \langle \Psi(t) | (b_{m_j} + b_{m_j}^\dagger) \frac{(\sigma_i^z + 1)}{2} | \Psi(t) \rangle, \tag{4.11}$$

which can be measured by mapping the motional onto the internal state of the auxiliary $N+1$-th ion, and then detecting resonance fluorescence of ions $N+1$ and i [20, 23]. We notice that with our setup the possibility of simulating a 2D and 3D Holstein model is provided, by encoding two and three dimensional interactions into a linear chain by addressing distant ions with nonlocal gates [60].

Currently, more than 100 gates have been implemented in a trapped-ion quantum simulation experiment with Trotter methods [25]. In the near future, it should be possible to achieve hundreds or even thousands of gates per experiment, allowing our proposal to reach about ten qubits. It is noteworthy to mention that our proposed digital quantum simulation will already overcome the limits of classical computers with 10 ions and 5 phonons per ion. This will allow to study the formation of small polarons under these conditions. Future experiments involving 20 to 30 ions will permit to address the study of more complex dynamics, including electron-electron correlations mediated by phonons. In this manner, the trapped-ion quantum simulator will prove to be a remarkable tool for simulating fermions coupled to bosons and related condensed-matter or high-energy physics scenarios.

4.5 Numerical simulations

In this section, we provide additional numeric plots and further discussions for our simulation protocol for a 2+1 and 3+1 ion configuration. First of all, in all our numerical simulations, we have fixed the total *simulated* time to a maximum of $2000/\nu_1$, in units of the center of mass (COM) mode frequency ν_1. Assuming $\nu_1 \sim 2\pi \times 1$ MHz, this gives a total simulated time of ~ 318 μs. We choose Trotter steps equally extended within a time $\tau = t/2$, where t is the total simulated time. With these assumptions, to compute the total effective *simulation* time, one has to multiply the simulated time by the number of terms in the decomposition of the simulated dynamics, i.e. 3 in our case. Then we have to add the time contribution for the global $\pi/4$ rotations along the Y axis, necessary to achieve the Z-like coupling to the phonons, that can be estimated to be around ~ 7 μs each [25]. Considering four global rotations per symmetric Trotter step, this gives a total simulation time of the order ~ 1 ms for the $r = 1$ and $r = 2$ case. This is well below the typical decoherence times for a trapped-ion setup [14]. Notice that we have made assumptions on the time extension for the Trotter steps, but nothing prevents to set the duration for the Trotter step to shorter times, as long as one can adjust properly the Rabi frequencies of the lasers used [25]. This paves the way to the scalability of the protocol.

The dynamics described by Hamiltonians H_1 and H_2 can be achieved by using two pairs of counterpropagating lasers with opposite detunings $\pm\delta_i$ [65], driving the i-th and the $i+1$-th ions. One can switch between a nearest neighbor (NN) XX/YY Ising interactions by taking appropriate initial phases for the lasers. The effective spin-spin coupling generated by this kind of laser drivings has the form of Eq. (7) in the main text.

In order to have negligible phonon displacements at the Trotter step time τ, one has to choose the detuning $\delta_i = \pm 2\pi/\tau + \Delta_m$ close to one of the modes of (shifted) frequencies Δ_m (thus $|\delta_i - \Delta_m| \ll |\Delta_m|, |\delta_i|$). We point out again here that in our

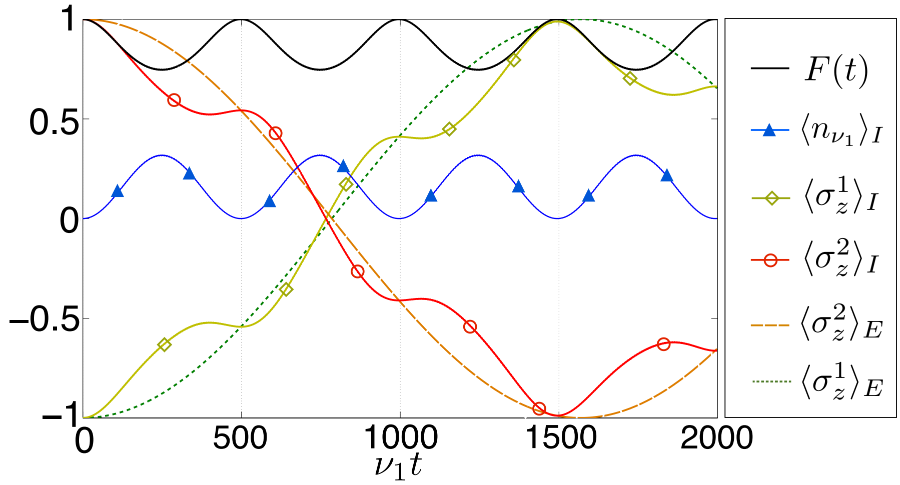

FIGURE 4.4: Dynamics for the 2+1 ions configuration of the NN XX Ising Hamiltonian. Dotted curves stand for $\langle\sigma_z^i\rangle_E$ for the exact dynamics, and solid curves stand for $\langle\sigma_z^i\rangle_I$ for realistic ion interactions ($i = 1, 2$ for the first and second ion). The parameters are chosen in order to have fidelity losses of $1 - F(t) = 1 - |\langle\Psi_E(t)|\Psi_I(t)\rangle|^2 \sim 10^{-4}$ (top black curve) at time steps of $\sim 500/\nu_1$.

protocol we deal with shifted frequencies, to take into account the desired dispersionless energies of the Holstein phonons. The ± sign in the choice of δ_i can be used to change the relative sign of the spin-spin interaction, depending on $\mathrm{sgn}[\eta_{i,m}\eta_{i+1,m}]$. We assume in our simulations a relative Lamb-Dicke parameter distribution for ions and modes as in [102], with an overall magnitude of 0.1. If one chooses $m = 1$ for the 2+1 ions setup, i.e. a detuning close to the COM mode, it must be set to $\delta = 2\pi/\tau + \Delta_1$, to obtain a positive $h/2$ coupling in the Ising NN interaction, because $\mathrm{sgn}[\eta_{1,1}\eta_{2,1}] = +$.

In Fig. 4.4, we show the numerical integration for the dynamics of the NN XX Ising interaction for a 2+1 ions configuration. The simulated strength for the Ising coupling is $h/2 = 0.001\ \nu_1$. For $\omega_0 = h/4$, one has a shifted frequency for the COM mode of $\Delta_1 = \nu_1 - 0.0005\nu_1/3$. By choosing $\tau = 500/\nu_1$, the detuning used in this case is $\delta = 2\pi\nu_1/500 + \Delta_1 = 1.0124\ \nu_1$, i.e. for $\nu_1 \simeq 2\pi \times 1$ MHz, a frequency difference with the mode of $\delta - \nu_1 = 2\pi \times 12.4$ KHz. The Rabi frequencies of the lasers are chosen in order to recover the desired strength for the Ising coupling.

To have an idea of how real ion interactions affect the protocol for a 2+1 ion setup, we make a plot of the errors on the simulated state with perfect gates and with ion gates in Fig. 4.5. One clearly sees that the higher fidelities obtained by using the ion gates with respect to the 3+1 ion setup are due to the higher single gate fidelity for the 2+1 setup, which permits to explore better fidelity regimes. The simulated parameters here are $g = h/10$, $\omega_0 = h/4$, $h = 0.002\ \nu_1$. We remark that in the simulations we have used a small g/h ratio to reduce the complexity of the simulation (i.e., the necessary truncation for the Fock space is small). Nevertheless, in a trapped-ion experiment, big

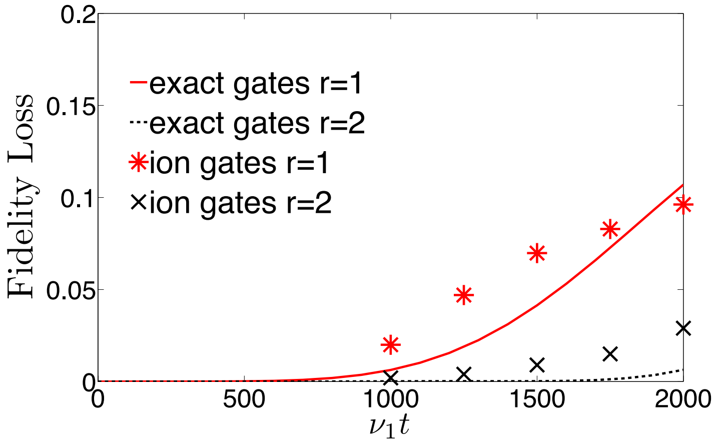

FIGURE 4.5: Fidelity loss for a 2+1 ions configuration as a function of time and Trotter steps. The simulated Holstein interaction has parameters $g = h/10$, $\omega_0 = h/4$. Dotted and solid lines stand respectively for a simulation with one and two symmetric Trotter steps. Single points stand for the error in the simulation protocol using ion gates.

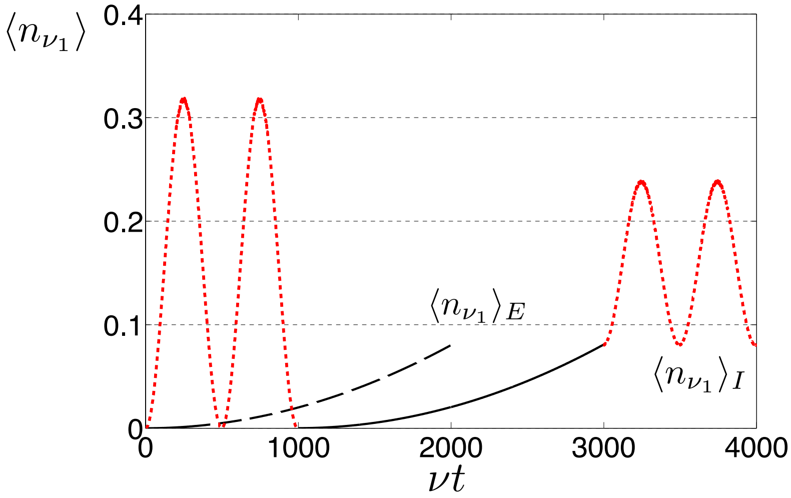

FIGURE 4.6: Mean number of phonons inside a Trotter protocol for a 2+1 ions configuration, for the Hamiltonian $H = H_1 + H_3$, where H_1 is a spin spin XX interaction and H_3 is a spin-phonon coupling interaction. The phonons are excited within the time for the H_3 steps (solid black line), and excited and released to their initial value within the H_1 interactions (dotted red lines), with the typical oscillations for this kind of gates.

g/h ratios with large freedom for the choice of ω_0 can be explored, thus recovering the typical *self trapping line* for the formation of small polarons [93]. The time points for the simulation range from $t = 1000/\nu_1$ to $t = 2000/\nu_1$. For $r = 1$ this gives Trotter steps ranging from $\tau = 500/\nu_1$ to $\tau = 1000/\nu_1$. The detuning for the NN interaction has to be set accordingly at each point, ranging from 1.0124 ν_1 to 1.0061 ν_1.

To obtain the plot of Fig. 3 in the main paper, with the same simulated parameter $g = h/10$, $\omega_0 = h/4$, $h = 0.002\ \nu_1$, we have used two simultaneous NN XX interactions as described above. One involves the first two ions with a detuning close to the COM mode, and another one driving the second and the third ion with a detuning close to the breathing mode, of frequency $\nu_2 = 1.731\ \nu_1$ [102]. To obtain an Ising interaction with the proper sign for the second and the third ion, we have to set the detuning for the second laser below the shifted frequency Δ_2. This is because for a 3+1 configuration (i.e., four ions in a linear trap), one has $\mathrm{sgn}[\eta_{1,1}\eta_{2,1}] \neq\ \mathrm{sgn}[\eta_{2,2}\eta_{3,2}]$ [102]. The detuning for the second set of lasers is therefore chosen to be $\delta = -2\pi/\tau + \Delta_2$. For example, for the simulation point at $t = 1000/\nu_1$, corresponding to $\tau = 250/\nu_1$ for $r = 2$, one has $\delta_1 = 1.025\ \nu_1$ and $\delta_2 = 1.7057\ \nu_1$. Using these parameters, it turns out that the non-nearest-neighbor coupling between the first and the third ion is negligible.

To get an insight of what happens to the phonon population of the COM mode inside a Trotter protocol, one can have a look to Fig. 4.6. Here, it is shown the mean number of phonons for a 2+1 ion setup using a symmetric decomposition at $r = 1$ of the Hamiltonian $H = H_1 + H_3$, where H_1 is a XX Ising interaction obtained with a detuning close to Δ_1 and H_3 is a Z-like coupling to phonons. The decomposed evolution operator has the form $U_2(t) = e^{-iH_1t/2}e^{-iH_3t/2}e^{-iH_3t/2}e^{-iH_1t/2}$. We see that, in the first and the last step, the two Ising interactions create phonons, while relaxing them at the end of the step, because the laser detuning and Rabi frequencies are chosen to obtain detachment from the phonons at the end of the Trotter step. In the two middle steps, the phonons are excited according to the H_3 Hamiltonian. The final mean value for the phonon number is recovered with respect to the dashed line value, which is the numerical value according to the exact evolution operator e^{-iHt}, with an error of $\sim 1\%$. Notice that since the decomposition involves symmetric Trotter steps, and each one is chosen to be of the same duration, the total simulation time is doubled.

Chapter 5

Quantum-classical simulator for quantum chemistry

5.1 Introduction

In this Chapter, we propose the implementation of a hybrid quantum-classical algorithm for the simulation of quantum chemistry problems. We show how quantum simulation steps can be inserted into the complex bottleneck parts of a simulation protocol, in order to retrieve molecular energy levels. We find that trapped-ion system are ideal systems for these kind of protocols, given the possibility of simulating fermionic interactions with collective gates.

Quantum chemistry represents one of the most successful applications of quantum mechanics. It provides an excellent platform for understanding matter from atomic to molecular scales, and involves heavy interplay of experimental and theoretical methods. In 1929, shortly after the completion of the basic structure of the quantum theory, Dirac speculated [103] that the fundamental laws for chemistry were completely known, but the application of the fundamental laws led to equations that were too complex to be solved. About ninety years later, with the help of transistor-based digital computers, the development of quantum chemistry continues to flourish, and many powerful methods, such as Hartree-Fock, configuration interaction, density functional theory, coupled-cluster, and quantum Monte Carlo, have been developed to tackle the complex equations of quantum chemistry (see e.g. [104] for a historical review). However, as the system size scales up, all of the methods known so far suffer from limitations that make them fail to maintain accuracy with a finite amount of resources [105]. In other words, quantum chemistry remains a hard problem to be solved by the current computer technology.

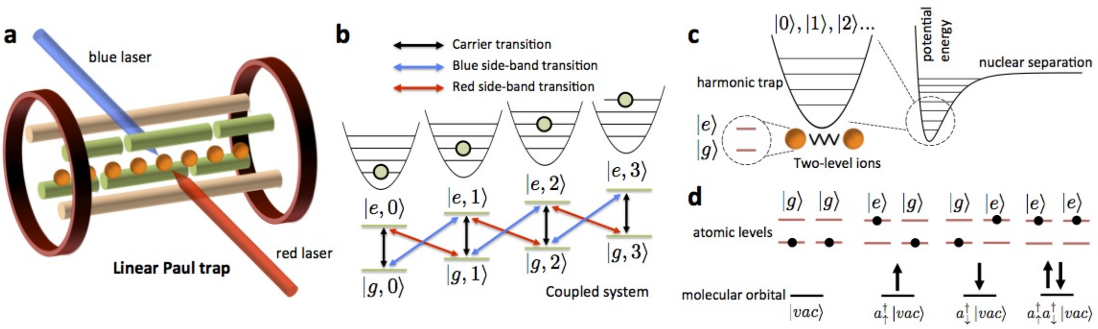
a
blue laser
Linear Paul trap
red laser
b
Carrier transition
Blue side-band transition
Red side-band transition
$|e,0\rangle$
$|e,1\rangle$
$|e,2\rangle$
$|e,3\rangle$
$|g,0\rangle$
$|g,1\rangle$
$|g,2\rangle$
$|g,3\rangle$
Coupled system
c
$|0\rangle, |1\rangle, |2\rangle...$
harmonic trap
potential energy
nuclear separation
$|e\rangle$
$|g\rangle$
Two-level ions
d
$|g\rangle$ $|g\rangle$ $|e\rangle$ $|g\rangle$ $|g\rangle$ $|e\rangle$ $|e\rangle$ $|e\rangle$
atomic levels
molecular orbital
$|vac\rangle$
$a^\dagger_\uparrow|vac\rangle$
$a^\dagger_\downarrow|vac\rangle$
$a^\dagger_\uparrow a^\dagger_\downarrow|vac\rangle$

FIGURE 5.1: Simulating quantum chemistry with trapped ions. (a) Scheme of a trapped-ion setup for quantum simulation, which contains a linear chain of trapped ions confined by a harmonic potential, and external lasers that couple the motional and internal degrees of freedom. (b) Transitions between internal and motional degrees of freedom of the ions in the trap. (c) The normal modes of the trapped ions can simulate the vibrational degrees of freedom of molecules. (d) The internal states of two ions can simulate all four possible configurations of a molecular orbital.

As envisioned by Feynman [2], one should be able to efficiently solve problems of quantum systems with a quantum computer. Instead of solving the complex equations, this approach, known as *quantum simulation* (see the recent reviews in Refs. [6, 106, 107]), aims to solve the problems by simulating target systems with another controllable quantum system, or qubits. Indeed, simulating many-body systems beyond classical resources will be a cornerstone of quantum computers. Quantum simulation is a very active field of study and various methods have been developed. Quantum simulation methods have been proposed for preparing specific states such as ground [108–113] and thermal states, simulating time evolution [24, 25, 60, 114, 115], and the measurement of physical observables [116].

Trapped-ion systems (see Fig. 5.1) are currently one of the most sophisticated technologies developed for quantum information processing [14]. These systems offer an unprecedented level of quantum control, which opens new possibilities for obtaining physico-chemical information about quantum chemical problems. The power of trapped ions for quantum simulation is manifested by the high-precision control over both the internal degrees of freedom of the individual ions and the phonon degrees of freedom of the collective motions of the trapped ions, and the high-fidelity initialization and measurement [8, 14]. Up to 100 quantum logic gates have been realized for six qubits with trapped ions [25], and quantum simulators involving 300 ions have been demonstrated [17].

In this work, we present an efficient toolkit for solving quantum chemistry problems based on the state-of-the-art in trapped-ion technologies. The toolkit comprises two components *i*) First, we present a hybrid quantum-classical variational optimization

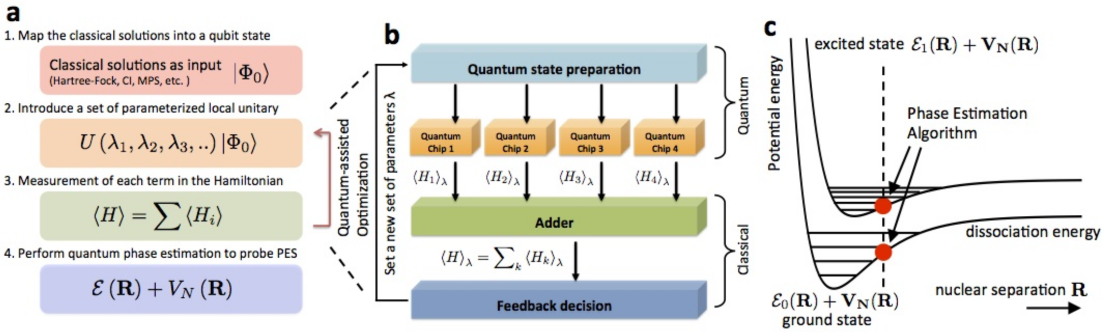
a
1. Map the classical solutions into a qubit state
Classical solutions as input
(Hartree-Fock, CI, MPS, etc.)
$|\Phi_0\rangle$
2. Introduce a set of parameterized local unitary
$U(\lambda_1, \lambda_2, \lambda_3, ..)\,|\Phi_0\rangle$
3. Measurement of each term in the Hamiltonian
$\langle H\rangle = \sum \langle H_i\rangle$
4. Perform quantum phase estimation to probe PES
$\mathcal{E}(\mathbf{R}) + V_N(\mathbf{R})$
Quantum-assisted Optimization
b
Set a new set of parameters λ
Quantum state preparation
Quantum Chip 1
Quantum Chip 2
Quantum Chip 3
Quantum Chip 4
$\langle H_1\rangle_\lambda$
$\langle H_2\rangle_\lambda$
$\langle H_3\rangle_\lambda$
$\langle H_4\rangle_\lambda$
Adder
$\langle H\rangle_\lambda = \sum_k \langle H_k\rangle_\lambda$
Feedback decision
Quantum
Classical
c
Potential energy
excited state $\mathcal{E}_1(\mathbf{R}) + \mathbf{V_N}(\mathbf{R})$
Phase Estimation Algorithm
dissociation energy
$\mathcal{E}_0(\mathbf{R}) + \mathbf{V_N}(\mathbf{R})$
ground state
nuclear separation $\mathbf{R}$

FIGURE 5.2: Outline of the quantum-assisted optimization method. (a) The key steps for quantum assisted optimization, which starts from classical solutions. For each new set of parameters λ's, determined by a classical optimization algorithm, the expectation value $\langle H\rangle$ is calculated. The potential energy surface is then obtained by quantum phase estimation. (b) Quantum measurements are performed for the individual terms in H, and the sum is obtained classically. (c) The same procedure is applied for each nuclear configuration $\mathbf{R}$ to probe the energy surface.

method, called quantum-assisted optimization, for approximating both ground-state energies and the ground-state eigenvectors for electronic problems. The optimized eigenvector can then be taken as an input for the phase estimation algorithm to project out the exact eigenstates and hence the potential-energy surfaces (see Fig. 5.2). Furthermore, we extend the application of the unitary coupled-cluster method [117]. This allows for the application of a method developed for classical numerical computations in the quantum domain. *ii*) The second main component of our toolkit is the optimized use of trapped-ion phonon degrees of freedom not only for quantum-gate construction, but also for simulating molecular vibrations, representing a mixed digital-analog quantum simulation. The phonon degrees of freedom in trapped-ion systems provide a natural platform for addressing spin-boson or fermion-boson-type problems through quantum simulation [19, 20, 57, 60, 70, 71]. It is noteworthy to mention that, contrary to the continuous of modes required for full-fledged quantum field theories, quantum simulations of quantum chemistry problems could reach realistic conditions for finite bosonic and fermionic mode numbers. Consequently, trapped ions can be exploited to solve dynamical problems involving linearly or non-linearly coupled oscillators, e.g., spin-boson models [118], that are difficult to solve either analytically or numerically with a classical computer. Furthermore, we have also developed a novel protocol to measure correlation functions of observables in trapped ions that will be crucial for the quantum simulation of quantum chemistry.

5.2 Trapped ions for quantum chemistry

Quantum chemistry deals with the many-body problem involving electrons and nuclei. Thus, it is very well suited for being simulated with trapped-ion systems, as we will show below. The full quantum chemistry Hamiltonian, $H = T_e + V_e + T_N + V_N + V_{eN}$, is a sum of the kinetic energies of the electrons $T_e \equiv -\frac{\hbar^2}{2m}\sum_i \nabla_{e,i}^2$ and nuclei $T_N \equiv -\sum_i \frac{\hbar^2}{2M_i}\nabla_{N,i}^2$, and the electron-electron $V_e \equiv \sum_{j>i} e^2/\left|\mathbf{r}_i - \mathbf{r}_j\right|$, nuclei-nuclei $V_N \equiv \sum_{j>i} Z_i Z_j e^2/\left|\mathbf{R}_i - \mathbf{R}_j\right|$, and electron-nuclei $V_{eN} \equiv -\sum_{i,j} Z_j e^2/\left|\mathbf{r}_i - \mathbf{R}_j\right|$ potential energies, where $\mathbf{r}$ and $\mathbf{R}$ respectively refer to the electronic and nuclear coordinates.

In many cases, it is more convenient to work on the second-quantization representation for quantum chemistry. The advantage is that one can choose a good fermionic basis set of molecular orbitals, $|p\rangle = c_p^\dagger\,|vac\rangle$, which can compactly capture the low-energy sector of the chemical system. This kind of second quantized fermionic Hamiltonians are efficiently simulatable in trapped ions [60]. To be more specific, we will choose first $M > N$ orbitals for an N-electron system. Denote $\phi_p\left(\mathbf{r}\right) \equiv \langle \mathbf{r}|\,p\rangle$ as the single-particle wavefunction corresponding to mode p. The electronic part, $H_e(\mathbf{R}) \equiv T_e + V_{eN}\left(\mathbf{R}\right) + V_e$, of the Hamiltonian H can be expressed as follows:

$$H_e(\mathbf{R}) = \sum_{pq} h_{pq} c_p^\dagger c_q + \frac{1}{2}\sum_{pqrs} h_{pqrs} c_p^\dagger c_q^\dagger c_r c_s, \tag{5.1}$$

where h_{pq} is obtained from the single-electron integral $h_{pq} \equiv -\int d\mathbf{r}\phi_p^*\left(\mathbf{r}\right)\left(T_e + V_{eN}\right)\phi_q\left(\mathbf{r}\right)$, and h_{pqrs} comes from the electron-electron Coulomb interaction,

$$h_{pqrs} \equiv \int d\mathbf{r}_1 d\mathbf{r}_2 \phi_p^*\left(\mathbf{r}_1\right)\phi_q^*\left(\mathbf{r}_2\right) V_e\left(\left|\mathbf{r}_1 - \mathbf{r}_2\right|\right)\phi_r\left(\mathbf{r}_2\right)\phi_s\left(\mathbf{r}_1\right). \tag{5.2}$$

We note that the total number of terms in H_e is $O(M^4)$; typically M is of the same order as N. Therefore, the number of terms in H_e scales polynomially in N, and the integrals $\{h_{pq}, h_{pqrs}\}$ can be numerically calculated by a classical computer with polynomial resources [109].

To implement the dynamics associated with the electronic Hamiltonian in Eq. (5.1) with a trapped-ion quantum simulator, one should take into account the fermionic nature of the operators c_p and $c_q^\dagger$. We invoke the Jordan-Wigner transformation (JWT), which is a method for mapping the occupation representation to the spin (or qubit) representation [119]. Specifically, for each fermionic mode p, an unoccupied state $|0\rangle_p$ is represented by the spin-down state $|\downarrow\rangle_p$, and an occupied state $|1\rangle_p$ is represented by the spin-up state $|\uparrow\rangle_p$. The exchange symmetry is enforced by the Jordan-Wigner transformation: $c_p^\dagger = (\prod_{m<p}\sigma_m^z)\sigma_p^+$ and $c_p = (\prod_{m<p}\sigma_m^z)\sigma_p^-$, where $\sigma^\pm \equiv \left(\sigma^x \pm i\sigma^y\right)/2$. Consequently, the electronic Hamiltonian in Eq. (5.1) becomes highly nonlocal in terms

of the Pauli operators $\{\sigma^x, \sigma^y, \sigma^z\}$, i.e.,

$$H_e \xrightarrow[\text{JWT}]{} \sum_{i,j,k\ldots\in\{x,y,z\}} g_{ijk\ldots}\left(\sigma_1^i \otimes \sigma_2^j \otimes \sigma_3^k \ldots\right) \quad . \tag{5.3}$$

Nevertheless, the simulation can still be made efficient with trapped ions, as we shall discuss below.

In trapped-ion physics two metastable internal levels of an ion are typically employed as a qubit. Ions can be confined either in Penning traps or radio frequency Paul traps [8], and cooled down to form crystals. Through sideband cooling the ions motional degrees of freedom can reach the ground state of the quantum Harmonic oscillator, that can be used as a quantum bus to perform gates among the different ions. Using resonance fluorescence with a cycling transition quantum non demolition measurements of the qubit can be performed. The fidelities of state preparation, single- and two-qubit gates, and detection, are all above 99% [14].

The basic interaction of a two-level trapped ion with a single-mode laser is given by [14], $H = \hbar\Omega\sigma_+ e^{-i(\Delta t-\phi)}\exp(i\eta[ae^{-i\omega_t t} + a^\dagger e^{i\omega_t t}]) + \text{H.c.}$, where $\sigma_\pm$ are the atomic raising and lowering operators, a ($a^\dagger$) is the annihilation (creation) operator of the considered motional mode, and Ω is the Rabi frequency associated to the laser strength. $\eta = kz_0$ is the Lamb-Dicke parameter, with k the wave vector of the laser and $z_0 = \sqrt{\hbar/(2m\omega_t)}$ the ground state width of the motional mode. ϕ is a controllable laser phase and Δ the laser-atom detuning.

In the Lamb-Dicke regime where $\eta\sqrt{\langle(a+a^\dagger)^2\rangle} \ll 1$, the basic interaction of a two-level trapped ion with a laser can be rewritten as

$$H = \hbar\Omega[\sigma_+ e^{-i(\Delta t-\phi)} + i\eta\sigma_+ e^{-i(\Delta t-\phi)}(ae^{-i\omega_t t} + a^\dagger e^{i\omega_t t}) + \text{H.c.}] \tag{5.4}$$

By adjusting the laser detuning Δ, one can generate the three basic ion-phonon interactions, namely: the carrier interaction ($\Delta = 0$), $H_c = \hbar\Omega(\sigma_+ e^{i\phi} + \sigma_- e^{-i\phi})$, the red sideband interaction, ($\Delta = -\omega_t$), $H_r = i\hbar\eta\Omega(\sigma_+ a e^{i\phi} - \sigma_- a^\dagger e^{-i\phi})$, and the blue sideband interaction, ($\Delta = \omega_t$), $H_b = i\hbar\eta\Omega(\sigma_+ a^\dagger e^{i\phi} - \sigma_- a e^{-i\phi})$. By combining detuned red and blue sideband interactions, one obtains the Mølmer-Sørensen gate [13], which is the basic building block for our methods. With combinations of this kind of gates, one can obtain dynamics as the associated one to H_e in Eq. (5.3), that will allow one to simulate arbitrary quantum chemistry systems.

5.3 Quantum-assisted optimization

Quantum-assisted optimization [120] (see also Fig. 5.2) for obtaining ground-state energies aims to optimize the use of quantum coherence by breaking down the quantum simulation through the use of both quantum and classical processors; the quantum processor is strategically employed for expensive tasks only.

To be more specific, the first step of quantum-assisted optimization is to prepare a set of quantum states $\{|\psi_\lambda\rangle\}$ that are characterized by a set of parameters $\{\lambda\}$. After the state is prepared, the expectation value $E_\lambda \equiv \langle\psi_\lambda| H |\psi_\lambda\rangle$ of the Hamiltonian H will be measured directly, without any quantum evolution in between. Practically, the quantum resources for the measurements can be significantly reduced when we divide the measurement of the Hamiltonian $H = \sum_i H_i$ into a polynomial number of small pieces $\langle H_i\rangle$ (cf Eq. (5.3)). These measurements can be performed in a parallel fashion, and no quantum coherence is needed to maintain between the measurements (see Fig. 5.2a and 5.2b). Then, once a data point of E_λ is obtained, the whole procedure is repeated for a new state $\{|\psi'_\lambda\rangle\}$ with another set of parameters $\{\lambda'\}$. The choice of the new parameters is determined by a classical optimization algorithm that aims to minimize E_λ (see Methods). The optimization procedure is terminated after the value of E_λ converges to some fixed value.

Finally, for electronic Hamiltonians $H_e(\mathbf{R})$, the optimized state can then be sent to a quantum circuit of phase estimation algorithm to produce a set of data point for some $\mathbf{R}$ on the potential energy surfaces (Fig. 5.2c shows the 1D case). After locating the local minima of the ground and excited states, vibronic coupling for the electronic structure can be further studied (see Supplementary Material).

The performance of quantum-assisted optimization depends crucially on (a) the choice of the variational states, and (b) efficient measurement methods. We found that the unitary coupled-cluster (UCC) states [117] are particularly suitable for being the input state for quantum-assisted optimization, where each quantum state $|\psi_\lambda\rangle$ can be prepared efficiently with standard techniques in trapped ions. Furthermore, efficient measurement methods for H_e are also available for trapped ion systems. We shall discuss these results in detail in the following sections.

5.4 Unitary coupled-cluster (UCC) ansatz

The unitary coupled-cluster (UCC) ansatz [117] assumes electronic states $|\psi\rangle$ have the following form, $|\psi\rangle = e^{T-T^\dagger} |\Phi\rangle$, where $|\Phi\rangle$ is a reference state, which can be, e.g., a

Slater determinant constructed from Hartree-Fock molecular orbitals. The particle-hole excitation operator, or cluster operator T, creates a linear combination of excited Slater determinants from $|\Phi\rangle$. Usually, T is divided into subgroups based on the particle-hole rank. More precisely, $T = T_1 + T_2 + T_3 + ... + T_N$ for an N-electron system, where $T_1 = \sum_{i,a} t_i^a c_a^\dagger c_i$, $T_2 = \sum_{i,j,a,b} t_{ij}^{ab} c_a^\dagger c_b^\dagger c_j c_i$, and so on.

Here $c_a^\dagger$ creates an electron in the orbital a. The indices a, b label unoccupied orbitals in the reference state $|\Phi\rangle$, and i, j label occupied orbitals. The energy obtained from UCC, namely $E = \langle\Phi| e^{T^\dagger - T} H e^{T - T^\dagger} |\Phi\rangle$ is a variational upper bound of the exact ground-state energy.

The key challenge for implementing UCC on a classical computer is that the computational resource grows exponentially. It is because, in principle, one has to expand the expression $\tilde{H} \equiv e^{T^\dagger - T} H e^{T - T^\dagger}$ into an infinity series, using the Baker-Campbell-Hausdorff expansion. Naturally, one has to rely on approximate methods [117] to truncate the series and keep track of finite numbers of terms. Therefore, in order to make good approximations by perturbative methods, i.e., assuming T is small, one implicitly assumes that the reference state $|\Phi\rangle$ is a good solution to the problem. However, in many cases, such an assumption is not valid and the use of approximate UCC breaks down. We explain below how implementing UCC on a trapped-ion quantum computer can overcome this problem.

We can generate the UCC state by simulating a pseudo time evolution through Suzuki-Trotter expansion on the evolution operator $e^{T - T^\dagger}$ [24]. To proceed, we consider an N-electron system with M, where $M > N$, molecular orbitals (including spins). We need totally M qubits; the reference state is the Hartree-Fock state where N orbitals are filled, and $M - N$ orbitals are empty, i.e, $|\Phi\rangle = |000...0111...1\rangle$. We also define an effective Hamiltonian $K \equiv i\left(T - T^\dagger\right)$, which means that we should prepare the state $e^{-iK}|\Phi\rangle$.

We decompose K into subgroups $K = K_1 + K_2 + K_3 + ... + K_P$, where $P \leq N$, and $K_i \equiv i(T_i - T_i^\dagger)$. We now write $e^{-iK} = \left(e^{-iK\delta}\right)^{1/\delta}$ for some dimensionless constant δ. For small δ, we have $e^{-iK\delta} \approx e^{-iK_P\delta} ... e^{-iK_2\delta} e^{-iK_1\delta}$. Since each K_j contains $N^j(M - N)^j$ terms of the creation $c^\dagger$ and annihilation c operators, we will need to individually simulate each term separately, e.g., $e^{-i\left(tc_a^\dagger c_i - t^* c_i^\dagger c_a\right)}$ and $e^{-i\left(tc_a^\dagger c_b^\dagger c_j c_i - t^* c_i^\dagger c_j^\dagger c_b c_a\right)}$, which can be implemented by transforming into spin operators through Jordan-Wigner transformation. The time evolution for each term can be simulated with a quantum circuit involving many nonlocal controlled gates, which can be efficiently implemented with trapped ions as we shall see below.

5.5 Implementation issues of UCC with trapped-ions

Our protocol for implementing the UCC ansatz requires the simulation of the small-time t/n evolution of non-local product of Pauli matrices of the form: $e^{-iH_l t/n}$, where $H_l = g_l \sigma_1^i \sigma_2^j \sigma_3^k \cdots$ for $i,j,k \in \{x,y,z\}$. Note that for any N-spin interaction, the $e^{-iH_l t/n}$ terms are equivalent to $e^{i\phi\sigma_1^z\sigma_2^x\sigma_3^x\cdots\sigma_N^x}$ through local spin rotations, which are simple to implement on trapped ions. Such a non-local operator can be implemented using the multi-particle Mølmer-Sørensen gate [60, 70]: $U_{\text{MS}}(\theta,\varphi) \equiv \exp\left[-i\theta(\cos\varphi S_x + \sin\varphi S_y)^2/4\right]$, where $S_{x,y} \equiv \sum_i \sigma_i^{x,y}$ is a collective spin operator. Explicitly,

$$e^{i\phi\sigma_1^z\sigma_2^x\sigma_3^x\cdots\sigma_N^x} = U_{MS}\left(\tfrac{-\pi}{2},0\right) R_N(\phi) U_{MS}\left(\tfrac{\pi}{2},0\right) \quad . \tag{5.5}$$

Here $R_N(\phi)$ is defined as follows: for any $m \in \mathbb{N}$, $R_N(\phi) = e^{\pm i\phi\sigma_1^z}$ for $N = 4m \pm 1$, and (ii) $R_N(\phi) = e^{i\phi\sigma_1^y}$ for $N = 4m$, and (iii) $R_N(\phi) = e^{-i\phi\sigma_1^y}$ for $N = 4m-2$.

It is remarkable that the standard quantum-circuit treatment for implementing each $e^{-iH_l t/n}$ involves as many as $2N$ two-qubit gates for simulating N fermionic modes; in our protocol one needs only two Mølmer-Sørensen gates, which are straightforwardly implementable with current trapped-ion technology. Furthermore, the local rotation $R_N(\phi)$ can also include motional degrees of freedom of the ions for simulating arbitrary fermionic Hamiltonians coupled linearly to bosonic operators a_k and $a_k^\dagger$.

5.6 Measurement of arbitrarily-nonlocal spin operators

For any given state $|\psi\rangle$, we show how to encode expectation value of products of Pauli matrices $\langle\sigma_1^i \otimes \sigma_2^j \otimes \sigma_3^k \otimes \cdots\rangle \equiv \langle\psi|\,\sigma_1^i \otimes \sigma_2^j \otimes \sigma_3^k \otimes \cdots |\psi\rangle$, where $i,j,k \in \{x,y,z\}$, onto an expectation value of a single qubit. The idea is to first apply the unitary evolution of the form: $e^{-i\theta(\sigma_1^i\otimes\sigma_2^j\otimes\cdots)}$, which as we have seen (cf Eq. 5.5) can be generated by trapped ions efficiently, to the state $|\psi\rangle$ before the measurement. For example, defining $|\psi_\theta\rangle \equiv e^{-i\theta\left(\sigma_1^x\otimes\sigma_2^x\otimes\cdots\right)}|\psi\rangle$, we have the relation

$$\langle\psi_\theta|\,\sigma_1^z\,|\psi_\theta\rangle = \cos(2\theta)\,\langle\sigma_1^z\rangle + \sin(2\theta)\,\langle\sigma_1^y \otimes \sigma_2^x \otimes \cdots\rangle \quad , \tag{5.6}$$

which equals $\langle\psi|(\sigma_1^y \otimes \sigma_2^x \otimes \ldots)|\psi\rangle$ for $\theta = \pi/4$. Note that the application of this method requires the measurement of one qubit only, making this technique especially suited for trapped ion systems where the fidelity of the measurement of one qubit is 99.99%.

This method can be further extended to include bosonic operators in the resulting expectation values. For example, re-define $|\psi_\theta\rangle \equiv e^{-i\theta(\sigma_1^i\otimes\sigma_2^j\otimes\cdots)\otimes\left(a+a^\dagger\right)}|\psi\rangle$ and consider

$\theta \to \theta\left(a + a^\dagger\right)$ in Eq. (5.6). We can obtain the desired correlation through the derivative of the single-qubit measurement: $\partial_\theta \left\langle \psi_\theta \right| \sigma_1^z \left| \psi_\theta \right\rangle|_{\theta=0} = -2\langle (\sigma_1^y \otimes \sigma_2^x \otimes \cdots)\left(a + a^\dagger\right)\rangle$. Note that the evolution operator of the form $e^{-i\theta(\sigma_1^i \otimes \sigma_2^j \otimes \cdots)\otimes(a+a^\dagger)}$ can be generated by replacing the local operation $R_N(\phi)$ in Eq. 5.5 with $e^{\pm i\phi\sigma_1^i(a+a^\dagger)}$. This technique allows us to obtain a diverse range of correlations between bosonic and internal degrees of freedom.

In the Born-Oppenheimer (BO) picture, the potential energy surface $\mathcal{E}_k\left(\mathbf{R}\right)+V_N\left(\mathbf{R}\right)$ associated with each electronic eigenstate $\left|\phi_k\right\rangle$ is obtained by scanning the eigenvalues $\mathcal{E}_k\left(\mathbf{R}\right)$ for each configurations of the nuclear coordinates $\{\mathbf{R}\}$. Of course, we can apply the standard quantum phase estimation algorithm [121] that allows us to extract the eigenvalues. However, this can require many ancilla qubits. In fact, locating these eigenvalues can be achieved by the phase estimation method utilizing one extra ancilla qubit [112] corresponding, in our case, to one additional ion.

This method works as follows: suppose we are given a certain quantum state $|\psi\rangle$ (which may be obtained from classical solutions with quantum-assisted optimization) and an electronic Hamiltonian $H_e(\mathbf{R})$ (cf. Eq. (5.1)). Expanding the input state, $|\psi\rangle = \sum_k \alpha_k \left|\phi_k\right\rangle$, by the eigenstate vectors $\left|\phi_k\right\rangle$ of $H_e(\mathbf{R})$, where $H_e\left(\mathbf{R}\right)\left|\phi_k\right\rangle = \mathcal{E}_k\left(\mathbf{R}\right)\left|\phi_k\right\rangle$, then for the input state $|0\rangle\,|\psi\rangle$, the quantum circuit of the quantum phase estimation produces the following output state, $\left(1/\sqrt{2}\right)\sum_k \alpha_k \left(|0\rangle + e^{-i\omega_k t}\,|1\rangle\right)\left|\phi_k\right\rangle$, where $\omega_k = \mathcal{E}_k/\hbar$. The corresponding reduced density matrix,

$$\frac{1}{2}\begin{pmatrix} 1 & \sum_k \left|\alpha_k\right|^2 e^{i\omega_k t} \\ \sum_k \left|\alpha_k\right|^2 e^{-i\omega_k t} & 1 \end{pmatrix}, \tag{5.7}$$

of the ancilla qubit contains the information about the weight (amplitude-square) $\left|\alpha_k\right|^2$ of the eigenvectors $\left|\phi_k\right\rangle$ in $|\psi\rangle$ and the associated eigenvalues ω_k in the off-diagonal matrix elements. All $\left|\alpha_k\right|^2$'s and ω_k's can be extracted by repeating the quantum circuit for a range of values of t and performing a (classical) Fourier transform to the measurement results. The potential energy surface is obtained by repeating the procedure for different values of the nuclear coordinates $\{\mathbf{R}\}$.

5.7 Numerical analysis

In order to show the feasibility of our protocol, we can estimate the trapped-ion resources needed to simulate, e.g., the prototypical electronic Hamiltonian $H_e = \sum h_{pq} a_p^\dagger a_q + (1/2)\sum h_{pqrs} a_p^\dagger a_q^\dagger a_r a_s$ as described in Eq. (5.1), for the specific case of the H_2 molecule in a minimal STO-3G basis. This is a two-electron system represented in a basis of four

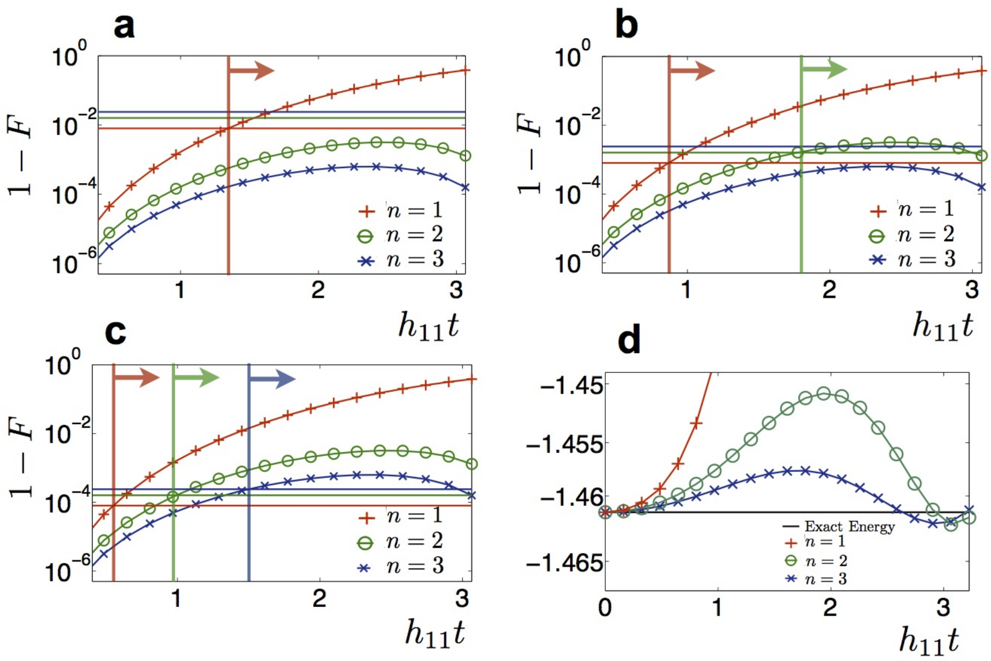

Figure 5.3: Digital error $1-F$ (curves) along with the accumulated gate error (horizontal lines) versus time in h_{11} energy units, for $n = 1, 2, 3$ Trotter steps in each plot, considering a protocol with an error per Trotter step of $\epsilon = 10^{-3}$ (a), $\epsilon = 10^{-4}$ (b) and $\epsilon = 10^{-5}$ (c). The initial state considered is $|\uparrow\uparrow\downarrow\downarrow\rangle$, in the qubit representation of the Hartree-Fock state in a molecular orbital basis with one electron on the first and second orbital. Vertical lines and arrows define the time domain in which the dominant part of the error is due to the digital approximation. d) Energy of the system, in h_{11} units, for the initial state $|\uparrow\uparrow\downarrow\downarrow\rangle$ for the exact dynamics, versus the digitized one. For a protocol with three Trotter steps the energy is recovered up to a negligible error.

spin-orbitals. The hydrogen atoms were separated by 0.75 Å, near the equilibrium bond distance of the molecule. The Hamiltonian is made up of 12 terms, that include 4 local ion operations and 8 non-local interactions. Therefore, to implement the dynamics, one needs 16 MS gates per Trotter step and a certain number of local rotations upon the ions. Since $\pi/2$ MS gates can be done in $\sim 50\mu$s, and local rotations can be performed in negligible times ($\sim 1\mu$s) [14, 25], the total simulation time can be assumed of about 800 μs for the $n = 1$ protocol, 1.6 ms and 2.4 ms for the $n = 2$ and $n = 3$ protocols. Thus total simulation times are within the decoherence times for trapped-ion setups, of about 30 ms [14]. In a digital protocol performed on real quantum systems, each gate is affected by an error. Thus, increasing the number of Trotter steps leads to an accumulation of the single gate error. To implement an effective quantum simulation, on one hand one has to increase the number of steps to reduce the error due to the digital approximation, on the other hand one is limited by the accumulation of the single gate error. We plot in Fig. 5.3a, 5.3b, 5.3c, the fidelity loss $1 - |\langle\Psi_S|\Psi_E\rangle|^2$ of the simulated state $|\Psi_S\rangle$ versus the exact one $|\Psi_E\rangle$, for the hydrogen Hamiltonian, starting from the initial state with two electrons in the first two orbitals. We plot, along with the digital error, three horizontal lines representing the accumulated gate error, for $n = 1, 2, 3$ in each plot, considering a protocol with an error per Trotter step of $\epsilon = 10^{-3}$ (a), $\epsilon = 10^{-4}$ (b) and $\epsilon = 10^{-5}$ (c). To achieve a reasonable fidelity, one has to find a number of steps that fits the simulation at a specific time. The vertical lines and arrows in the figure mark the time regions in which the error starts to be dominated by the digital error. Trapped-ion two-qubit gates are predicted to achieve in the near future fidelities of 10^{-4}, thus making the use of these protocols feasible. In Fig. 5.3d we plot the behavior of the energy of the system for the initial state $|\uparrow\uparrow\downarrow\downarrow\rangle$ for the exact dynamics, versus the digitized one. Again, one can observe how the energy can be retrieved with a small error within a reduced number of digital steps.

To implement the optimization with the UCC wavefunction ansatz on a trapped-ion quantum simulator, our proposal is to first employ classical algorithms to obtain approximate solutions [117]. Then, we can further improve the quality of the solution by searching for the true minima with an ion trap. The idea is as follows: first we create a UCC ansatz by the Suzuki-Trotter method described in the previous section. Denote this choice of the cluster operator as $T^{(0)}$, and other choices as $T^{(k)}$ with $k = 1, 2, 3, ...$ The corresponding energy $E_0 = \langle\Phi| e^{T^{(0)\dagger}-T^{(0)}} H e^{T^{(0)}-T^{(0)\dagger}} |\Phi\rangle$ of the initial state is obtained by a classical computer.

Next, we choose another set of cluster operator $T^{(1)}$ with is a perturbation around $T^{(0)}$. Define the new probe state $|\phi_k\rangle \equiv e^{T^{(k)}-T^{(k)\dagger}} |\Phi\rangle$. Then, the expectation value of the energy $E_1 = \langle\Phi|e^{T^{(1)\dagger}-T^{(1)}} H e^{T^{(1)}-T^{(1)\dagger}} |\Phi\rangle = \langle\phi_1| H |\phi_1\rangle$ can be obtained by measuring components of the second quantized Hamiltonian,

$$\langle\phi_1| H |\phi_1\rangle = \sum\nolimits_{pqrs} \tilde{h}_{pqrs} \langle\phi_1|c_p^\dagger c_q^\dagger c_r c_s |\phi_1\rangle \,. \tag{5.8}$$

Recall that the coefficients $\tilde{h}_{pqrs}$ are all precomputed and known.

In order to obtain measurement results for the operators $\langle\phi_1| c_p^\dagger c_q^\dagger c_r c_s |\phi_1\rangle$, we will first convert the fermion operators into spin operators via Jordan-Wigner transformation; the same procedure is applied for creating the state $|\phi_1\rangle$. The quantum measurement for the resulting products of Pauli matrices can be achieved efficiently with trapped ions, using the method we described.

The following steps are determined through a classical optimization algorithm. There can be many choices for such an algorithm, for example gradient descent method, Nelder-Mead method, or quasi-Newton methods. For completeness, we summarize below the application of gradient descent method to our optimization problem.

First we define the vector $\mathbf{T}^{(k)} = (t_i^{a(k)}, t_{ij}^{ab(k)}, ...)^T$ to contain all coefficients in the cluster operator $T^{(k)}$ at the k-th step. We can also write the expectation value

$E\left(\mathbf{T}^{(k)}\right) \equiv \langle\phi_k| H |\phi_k\rangle$ for each step as a function of $\mathbf{T}^{(k)}$. The main idea of the gradient descent method is that $E\left(\mathbf{T}^{(k)}\right)$ decreases fastest along the direction of the negative gradient of $E\left(\mathbf{T}^{(k)}\right)$, $-\nabla E\left(\mathbf{T}^{(k)}\right)$. Therefore, the $(k+1)$-th step is determined by the following relation:

$$\mathbf{T}^{(k+1)} = \mathbf{T}^{(k)} - a_k \nabla E(\mathbf{T}^{(k)}), \tag{5.9}$$

where a_k is an adjustable parameter; it can be different for each step. To obtain values of the gradient $\nabla E\left(\mathbf{T}^{(k)}\right)$, one may use the finite-difference method to approximate the gradient. However, numerical gradient techniques are often susceptible to numerical instability. Alternatively, we can invoke the Hellman-Feynman theorem and get, e.g., $(\partial/\partial t_i^a)\, E(\mathbf{T}^{(k)}) = \langle\phi_k|[H, c_a^\dagger c_i]\,|\phi_k\rangle$, which can be obtained with a method similar to that for obtaining $E(\mathbf{T}^{(k)})$.

Finally, as a valid assumption for general cases, we assume our parametrization of UCC gives a smooth function for $E\left(\mathbf{T}^{(k)}\right)$. Thus, it follows that $E\left(\mathbf{T}^{(0)}\right) \geq E\left(\mathbf{T}^{(1)}\right) \geq E\left(\mathbf{T}^{(2)}\right) \geq \cdots$, and eventually $E\left(\mathbf{T}^{(k)}\right)$ converges to a minimum value for large k. Finally, we can also obtain the optimized UCC quantum state.

Part II

Complex systems in superconducting circuits

Chapter 6

Interacting spin models using superconducting circuits

6.1 Introduction

The quantum coherent control of superconducting qubits has improved dramatically in the last years [34]. In this sense, circuit quantum electrodynamics (cQED) [31] is considered as a potential scalable platform for quantum computing. Basic quantum algorithms [122] and tests of fundamentals in quantum mechanics [123] have been already realized. Moreover, superconducting circuits have reached sufficient complexity and potential scalability to be considered as quantum simulators. In this Chapter, we propose a series of simulation protocols for interacting spin systems, amenable to realization in a cQED architecture. We find that trough the use of natural two-qubit dispersive interactions present in this system, a universal simulation of spin dynamics can be dynamically built within a set of charge-like qubits.

A quantum simulator is a platform that allows to reproduce the behavior of another quantum system. The original idea of quantum simulation can be traced back to Feynman [2], while the first mathematical formulation using local interactions was proposed some years later [24]. So far, initial steps for quantum simulations in circuit QED have been taken, where a few analog quantum simulators have been proposed in superconducting qubits. On the other hand, an experiment of discrete-time gate sequences to reproduce the dynamics of a given spin Hamiltonian has been recently realized in ion-trap [25] and photonic [111] systems, together with proposals for the emulation of interacting fermionic-bosonic models [60, 71]. The digital decomposition of Hamiltonians and their implementation using short-time gates has been demonstrated to be efficient [40, 80]. Accordingly, it is timely to address the issue of digital quantum simulators with superconducting circuits. The quantum simulation of spin models can shed light onto a variety of open problems, such as quantum phase transitions [124], correlated one-dimensional systems [125], and high-T_c superconductivity [126].

We investigate the possible implementation of digital quantum simulations of spin Hamiltonians in a superconducting setup, consisting of several superconducting qubits, coupled to a coplanar waveguide resonator. Although our proposal is valid for every superconductor-based qubit with long enough coherence time, we focus on a transmon qubit setup. Superconducting transmon qubits are one of the most used superconducting qubits due to their low sensitivity to offset charge fluctuations [30], that makes them the best candidates for quantum simulations. First, we show that a variety of spin dynamics can be retrieved by a digital decomposition in a generic quantum simulator. Then, we consider prototypical spin models, simulation times, and fidelities with current circuit QED technology, showing the computational power of superconducting qubits in terms of digital quantum simulations. In this way, we analyze the resources that are required to implement, in a realistic setup, a multipurpose quantum simulator of spin dynamics capable of emulating a general many-qubit spin Hamiltonian.

Most physical Hamiltonians can be written as a sum of local terms, $H = \sum_{k=1}^{N} H_k$, where each H_k acts on a local Hilbert space. The dynamics of a generic Hamiltonian H can be approximated by discrete stepwise unitaries, up to arbitrary small errors, according to the formula ($\hbar = 1$ here and in the following) [24],

$$\begin{aligned} e^{-iHt} = & \left(e^{-iH_1 t/l} \cdots e^{-iH_N t/l}\right)^l \\ & + \sum_{i<j} \frac{[H_i, H_j]t^2}{2l} + \sum_{k=3}^{\infty} E(k), \end{aligned} \tag{6.1}$$

with $l||Ht/l||_{\text{sup}}^k/k! \geq ||E(k)||_{\text{sup}}$ being an upper bound on the higher order error terms. In the trivial case, when $[H_i, H_j] = 0$ for every $\{i, j\}$, the error made in the digital approximation is zero. To approximate e^{-iHt} to arbitrary precision, one can divide the simulated time t into l time intervals of size t/l, and apply sequentially the evolution operator of each local term for every time interval. Repeating the sequence l times, the error can be made as small as desired just by increasing l. However, in a realistic quantum simulator, there will be a limit to the number of local $e^{-iH_k t/l}$ gates, due to accumulated gate errors. Accordingly, one has to optimize the number of steps l to get the best possible result.

6.2 Heisenberg interaction with digital methods

Digital methods can be used to simulate the Heisenberg spin model with available resources in superconducting circuits. We consider a setup made of several transmon qubits coupled to a single coplanar microwave resonator [30],

$$\begin{aligned} H^{\mathrm{T}} = \quad & \sum_{i=1}^{N} 4E_{C,i}(n_i - n_{g,i})^2 - E_{J,i}\cos\phi_i \\ & +\omega_r a^\dagger a + 2\beta_i e V_{\mathrm{rms}} n_i (a + a^\dagger). \end{aligned} \tag{6.2}$$

Here, n_i, $n_{g,i}$ and ϕ_i stand respectively for the quantized charge on the superconducting island, the offset charge and the quantized flux of the i-th transmon qubit. The operators $a(a^\dagger)$ act on the resonator field, whose first mode has frequency ω_r. $E_{C,i}$ is the charging energy of the superconducting island, while $E_{J,i} = E_{J,i}^{\max}|\cos(\pi\Phi_i/\Phi_0)|$ is the Josephson energy of the dc-SQUID loop embedded in the i-th qubit. The latter can be tuned from small values up to $E_{J,i}^{\max}$ by changing the ratio of the external magnetic flux Φ_i, that threads the loop, with the elementary flux quantum Φ_0. Here β_i are renormalization coefficients of the couplings due to circuit capacitances, V_{rms} is the root mean square voltage of the resonator, and e is the electron charge. Typical transmon regimes consider ratios of Josephson versus charging energy starting from $E_J/E_C \gtrsim 20$.

Notice that cavity and circuit QED platforms do not feature the Heisenberg interaction from first principles. Nevertheless, one can consider a digital simulation of the model. We show that the coupled transmon-resonator system, governed by the Hamiltonian in Eq. (6.2), can simulate Heisenberg interactions of N qubits, which in the case of homogeneous couplings reads

$$H^{\mathrm{H}} = \sum_{i=1}^{N-1} J\left(\sigma_i^x\sigma_{i+1}^x + \sigma_i^y\sigma_{i+1}^y + \sigma_i^z\sigma_{i+1}^z\right). \tag{6.3}$$

Here the Pauli matrices σ_i^j, $j \in \{x, y, z\}$ refer to the subspace spanned by the first two levels of the i-th transmon qubit. We begin by considering the simplest case, in which two qubits are involved. The XY exchange interaction can be directly reproduced by dispersively coupling two transmon qubits to the same resonator [32], $H_{12}^{xy} = J\left(\sigma_1^+\sigma_2^- + \sigma_1^-\sigma_2^+\right) = J/2\,(\sigma_1^x\sigma_2^x + \sigma_1^y\sigma_2^y)$. The XY exchange interaction can be transformed via local rotations of the single qubits to get the effective Hamiltonian $H_{12}^{xz} = R_{12}^x(\pi/4)H_{12}^{xy}R_{12}^{x\dagger}(\pi/4) = J/2\,(\sigma_1^x\sigma_2^x + \sigma_1^z\sigma_2^z)$. Here, $R_{12}^{x(y)}(\pi/4) = \exp[-i\pi/4(\sigma_1^{x(y)} + \sigma_2^{x(y)})]$ represents a local rotation of the first and second transmon qubits along the $x(y)$ axis. The XYZ exchange Hamiltonian H_{12}^{xyz} can therefore be implemented according to the protocol shown in Fig. 6.1a with the following steps. *Step 1.*– The qubits interact

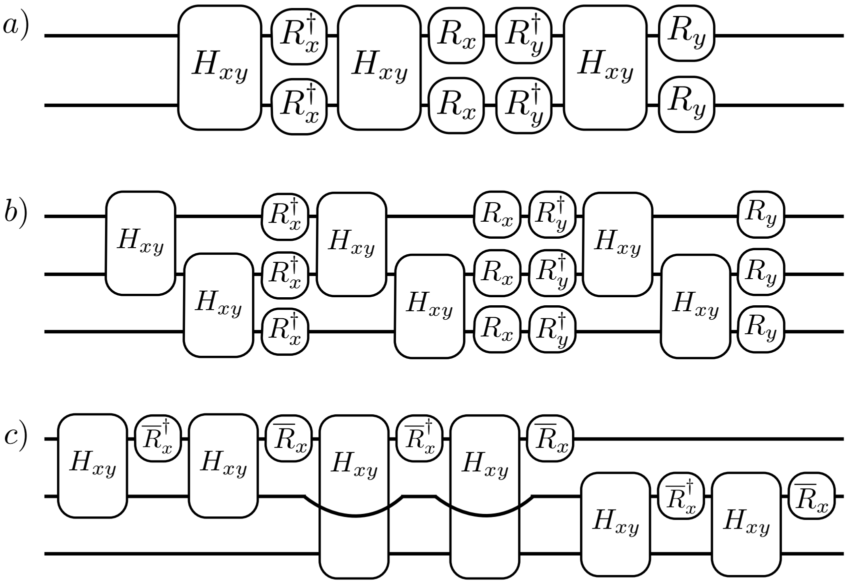

FIGURE 6.1: Protocols for digital quantum simulations with transmon qubits. a) Heisenberg model of two qubits. b) Heisenberg model of three qubits. c) Frustrated Ising model of three qubits. Here $R_{x(y)} \equiv R^{x(y)}(\pi/4)$ and $\overline{R}_x \equiv R^x(\pi/2)$.

for a time t according to the XY Hamiltonian H_{12}^{xy}. *Step 2.–* Application of single qubit rotations $R_{12}^{x}(\pi/4)$ to both qubits. *Step 3.–* The qubits interact for a time t with H_{12}^{xy} Hamiltonian. *Step 4.–* Application of single qubit rotation $R_{12}^{x\dagger}(\pi/4)$ to both qubits. *Step 5.–* Application of single qubit rotation $R_{12}^{y}(\pi/4)$ to both qubits. *Step 6.–* The qubits interact for a time t according to the H_{12}^{xy} Hamiltonian. *Step 7.–* Application of single qubit rotation $R_{12}^{y\dagger}(\pi/4)$ to both qubits. Consequently, the total unitary evolution reads

$$U_{12}^{\mathrm{H}}(t) \quad = \quad e^{-iH_{12}^{xy}t}e^{-iH_{12}^{xz}t}e^{-iH_{12}^{yz}t} = e^{-iH_{12}^{\mathrm{H}}t}. \tag{6.4}$$

This evolution operator simulates the dynamics of Eq. (6.3) for two qubits. Arbitrary inhomogeneites of the couplings can be achieved by implementing different simulated phases for different digital steps. Notice that, in this case, just one Trotter step is needed to achieve a simulation without digital errors, due to the commutativity of H_{12}^{xy}, H_{12}^{xz}, and H_{12}^{yz}. Thus, from a practical point of view, the only source of errors will come from accumulated gate errors. One can assume two-qubit gates with an error of about 5% and eight $\pi/4$ single qubit rotations with errors of 1%. This will give a total fidelity of the protocol around 77%. Moreover, the total execution time for the protocol for a $\pi/4$ simulated XYZ phase will be of about 0.10 μs.

Now, we consider a digital protocol for the simulation of the Heisenberg interaction for a chain of three spins. When considering more than two spins, one has to take into account noncommuting Hamiltonian steps, involving digital errors. This three-spin

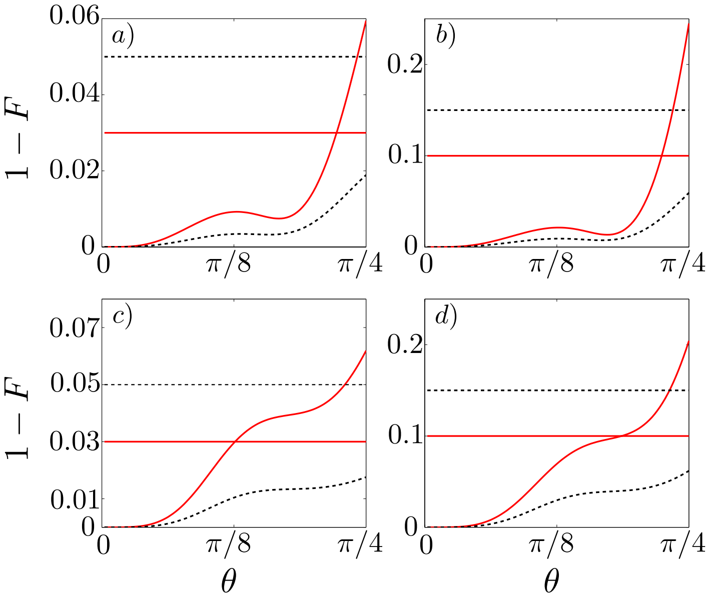

FIGURE 6.2: Fidelity loss for simulated Hamiltonians for three qubits, in the interval $\theta = [0, \pi/4]$, $\theta \equiv Jt$. Curved lines show digital errors, while horizontal lines show the accumulated error due to a single step error of ϵ. Red solid (black dotted) lines stand for higher (lower) digital approximations l. a) Heisenberg model, with $\epsilon = 10^{-2}$, $l = 3, 5$, and b) $\epsilon = 5 \times 10^{-2}$, $l = 2, 3$. c) Transverse field Ising model, with $\epsilon = 10^{-2}$, $l = 3, 5$ and d) $\epsilon = 5 \times 10^{-2}$, $l = 2, 3$.

case is directly extendable to arbitrary numbers of spins. We follow a digital approach for its implementation, as shown in Fig. 6.1b. *Step 1.–* Qubits 1 and 2 interact for a time t/l with XY Hamiltonian. *Step 2.–* Qubits 2 and 3 interact for a time t/l with XY Hamiltonian. *Step 3.–* Application of $R^{x}_{12}(\pi/4)$ to each qubit. *Step 4.–* Qubits 1 and 2 interact for a time t/l with XY Hamiltonian. *Step 5.–* Qubits 2 and 3 interact for a time t/l with XY Hamiltonian. *Step 6.–* Application of $R^{x\dagger}_{12}(\pi/4)$ to each qubit. *Step 7.–* Application of $R^{y}_{12}(\pi/4)$ to each qubit. *Step 8.–* Qubits 1 and 2 interact for a time t/l with XY Hamiltonian. *Step 9.–* Qubits 2 and 3 interact for a time t/l with XY Hamiltonian. *Step 10.–* Application of $R^{y\dagger}_{12}(\pi/4)$ to each qubit. Therefore, the total unitary evolution per step reads

$$\begin{aligned} U^{\mathrm{H}}_{123}(t/l) = \; & e^{-iH^{xy}_{12}t/l}e^{-iH^{xy}_{23}t/l}e^{-iH^{xz}_{12}t/l}e^{-iH^{xz}_{23}t/l} \\ & \times e^{-iH^{yz}_{12}t/l}e^{-iH^{yz}_{23}t/l}. \end{aligned} \tag{6.5}$$

In this case, the protocol has to be repeated l times according to Eq. (6.1), to approximate the dynamics of Eq. (6.3) for three qubits. Each Trotter step involves four single qubit gates at different times and six two qubit gates, producing a step-time of about 0.16 μs, which is well below standard coherence times for transmon qubits [127]. In Fig. 6.2a and 2b, we plot the digital error of the simulated Heisenberg model for three

Table 6.1: Execution times and error bounds for the Heisenberg and Ising models with open and periodic boundary conditions for N qubits. Here $\theta \equiv Jt$, $J/2$ and g_ϕ are respectively the coupling strenght of the XY and single-qubit gates, and τ_s is the pulse raising time for a single qubit rotation.

	Execution time	Error bound
$\mathrm{H_o}$	$4l\tau_s + 6(N-1)\theta/J$	$24(N-2)(Jt)^2/l$
$\mathrm{H_p}$	$4l\tau_s + 6N\theta/J$	$24N(Jt)^2/l$
$\mathrm{I_o}$	$2(N-1)l\tau_s + \theta/g_\phi + 4(N-1)\theta/J$	$2(N-1)(Jt)^2/l$
$\mathrm{I_p}$	$2Nl\tau_s + \theta/g_\phi + 4N\theta/J$	$2N(Jt)^2/l$

qubits, along with horizontal lines, that show the error of the imperfect gates multiplied by the number of Trotter steps, i.e., the total accumulated gate error. In this way, one can distinguish time domains dominated by the digital error and time domains in which the largest part of the error in the quantum simulation is due to experimental gate errors. One can consider interactions with open and closed boundary conditions, adding an extra term coupling the first and last spin. Extending this protocol to N qubits with open or periodic boundary conditions, we compute an upper bound on the second order Trotter error $E_{\text{open}} = 48(N-2)(Jt)^2/2l$ and $E_{\text{periodic}} = 48N(Jt)^2/2l$.

6.3 Ising interaction with digital methods

We consider now a generic N qubit Ising interaction $J\sum_i \sigma_i^x \sigma_{i+1}^x$, with periodic boundary conditions. Considering a three site model is sufficient to show the effect of frustration in the system. The antiferromagnetic interaction is inefficiently solvable in a classical computer, while it is efficient for a quantum simulator [128]. We consider the isotropic antiferromagnetic case between three sites , $H_{123}^{\mathrm{I}} = J\sum_{i<j} \sigma_i^x \sigma_j^x$, with $i, j = 1, 2, 3$ and $J > 0$. In order to simulate this Hamiltonian, one can apply a $\pi/2$ rotation to one of the qubits. This will result in an effective stepwise elimination of the YY component of interaction,

$$H_{12}^{x-y} = R_1^x(\pi/2) H_{12}^{xy} R_1^{x\dagger}(\pi/2) = J\left(\sigma_1^x \sigma_2^x - \sigma_1^y \sigma_2^y\right). \tag{6.6}$$

The protocol for the simulation is shown in Fig. 6.1c. As the terms of the Ising Hamiltonian commute, there is no error from the Trotter expansion. We obtain a fidelity of the protocol of about 64%. The time for the execution of all gates is of 0.18 μs.

One can also add a transverse magnetic field, that leads to the Hamiltonian $H_{123}^{\mathrm{IT}} = J\sum_{i<j} \sigma_i^x \sigma_j^x + B\sum_i \sigma_i^y$. In this case, the terms of the Hamiltonian do not commute, so we need to apply more than one Trotter step to achieve adequate fidelities. The unitary

evolution per Trotter step in this case is given by,

$$\begin{aligned} U(t/l) &= e^{-iH_{12}^{xy}t/l}e^{-iH_{12}^{x-y}t/l}e^{-iH_{13}^{xy}t/l}e^{-iH_{13}^{x-y}t/l} \\ &\times e^{-iH_{23}^{xy}t/l}e^{-iH_{23}^{x-y}t/l}e^{-iBt/l(\sigma_1^y+\sigma_2^y+\sigma_3^y)} \\ &= e^{-i2Jt/l(\sigma_1^x\sigma_2^x+\sigma_1^x\sigma_3^x+\sigma_2^x\sigma_3^x)}e^{-iBt/l(\sigma_1^y+\sigma_2^y+\sigma_3^y)}. \end{aligned} \tag{6.7}$$

In Fig. 6.2c and 2d, we plot the fidelity loss for different number of Trotter steps, in the 3-qubit frustrated Ising model with transverse magnetic field, considering a certain error for each step due to the imperfect gates. The protocol can also be extended to N qubits with open and periodic boundary conditions, where we compute an upper bound to the second order error in Jt/l of $E_{\text{open}} = 4(N-1)(Jt)^2/2l$ and $E_{\text{periodic}} = 4N(Jt)^2/2l$. We report in Table 8.1 execution times and error bounds for the models proposed, for N qubits.

6.4 Feasibility in current architectures

In order to estimate the feasibility of the protocols in a superconducting circuit setup, we perform a numerical simulation for the Heisenberg interaction between two transmon qubits coupled to a coplanar waveguide resonator. We compute the effect on the protocol of a realistic XY interaction, given as an effective second order Hamiltonian, obtained from the first order Hamiltonian

$$\begin{aligned} H_{\text{t}} =& \sum_{i=0}^{2}\sum_{j=1}^{2}\Big(\omega_i^j \left|i,j\right\rangle\left\langle i,j\right|\Big) + \omega_r a^\dagger a \\ &+ \sum_{i=0}^{2}\sum_{j=1}^{2} g_{i,i+1}(\left|i,j\right\rangle\left\langle i+1,j\right| + \text{H.c.})(a+a^\dagger). \end{aligned} \tag{6.8}$$

Here, ω_i^j is the transition energy of the i-th level, with respect to the ground state, of the j-th qubit, and ω_r is the transition frequency of the resonator. We consider the first three levels for each transmon qubit, and a relative anharmonicity factor of $\alpha_r = (\omega_2^j - 2\omega_1^j)/\omega_1^j = -0.1$, typical for the transmon regime [30]. We assume identical transmon devices, with transition frequencies $\omega_1^{1,2} \equiv \omega_1 = 2\pi \times 5$ GHz. The resonator frequency is set to $\omega_r = 2\pi \times 7.5$ GHz. We consider $g_{i,i+1} = \sqrt{i+1}g_0$, where $g_0 = 2\beta e V_{\text{rms}} = 2\pi \times 200$ MHz. The resonator-transmon coupling Hamiltonian, in interaction picture with the free energy $\sum_{i,j}\omega_i^j \left|i,j\right\rangle\left\langle i,j\right| + \omega_r a^\dagger a$, results in an effective coupling between the first two levels of the two transmon qubits $H_{\text{eff}} = [g_{01}^2\omega_1/(\omega_1^2-\omega_r^2)] \times (\sigma_1^x\sigma_2^x + \sigma_1^y\sigma_2^y)$, where we have considered negligible cavity population $\langle a^\dagger a\rangle \approx 0$ and renormalization of the qubit frequencies to cancel Lamb shifts. Here we have defined a set of Pauli matrices for the subspace spanned by the first two levels of each transmon, e.g. $\sigma^x_{1(2)} \equiv |0, 1(2)\rangle \langle 1, 1(2)| + \mathrm{H.c.}$ In order to estimate the effect of decoherence in a realistic setup, we consider the master equation dynamics,

$$\dot{\rho} = -i[H_{\mathrm{t}}, \rho] + \kappa L(a)\rho + \sum_{i=1}^{2} \left(\Gamma_\phi L(\sigma_i^z)\rho + \Gamma_- L(\sigma_i^-)\rho \right), \tag{6.9}$$

where we have defined the Lindblad superoperators $L(\hat{A})\rho = (2\hat{A}\rho\hat{A}^\dagger - \hat{A}^\dagger\hat{A}\rho - \rho\hat{A}^\dagger\hat{A})/2$. We have set a decay rate for the resonator of $\kappa = 2\pi \times 10$ kHz, and a dephasing and decay rate for the single transmon qubit of $\Gamma_\phi = \Gamma_- = 2\pi \times 20$ kHz. We perform a numerical simulation for the Heisenberg protocol for two transmon qubits, following the steps as in Fig. 6.1a, using for the XY interaction steps the result of the dynamics obtained by solving Eq. (6.9), and ideal single-qubit rotations. The result is plotted in Fig. 6.3. The evolution for the density matrix ρ, that encodes the dynamics of the two transmon qubits, is compared to the exact quantum evolution $|\Psi\rangle_I$, that evolves according to the Hamiltonian in Eq. (6.3), with $J = g_{01}^2\omega_1/(\omega_1^2 - \omega_r^2) \approx 2\pi \times 6$ MHz. One can observe that good simulation fidelities $F = \mathrm{Tr}(\rho|\Psi_I\rangle\langle\Psi_I|)$ are achieved for a nontrivial dynamics. Notice that the action of the Heisenberg Hamiltonian on an initial state, which is also an eigenstate of the $\sigma_1^z\sigma_2^z$ operator, would be equivalent to the one of the XY exchange interaction. To show signatures of the Heisenberg interaction, we choose in our simulation an initial state which has not this property. One can also notice the typical small time-scale fidelity oscillations due to the first order part of the dispersive exchange interaction. By further detuning of the qubits with respect to the resonator, one can reduce the contribution from the non-dispersive part of the interaction, and increase the global fidelity of the protocol.

In conclusion, we have proposed a digital quantum simulation of spin chain models in superconducting circuits. We have considered prototypical models as the Heisenberg and frustrated Ising interactions. Furthermore, we have shown the feasibility of the simulation with state-of-the-art technology of transmon qubits coupled to microwave resonators. In the near future, these protocols may be extended to many-qubit spin models, paving the way towards universal quantum simulation of spin dynamics in circuit QED setups. The latter may be relevant for understanding the behavior of highly correlated quantum systems.

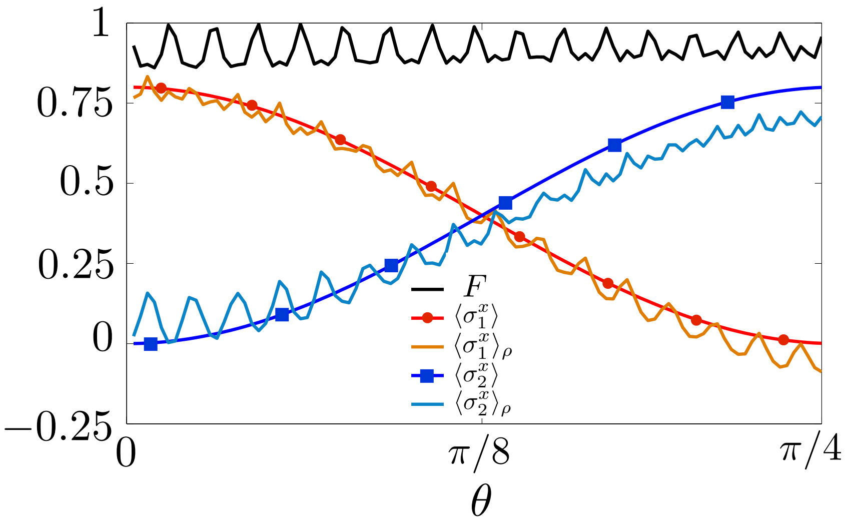

FIGURE 6.3: Dynamics for the simulated Heisenberg model for two transmon qubits, which are initialized in the state $1/\sqrt{5}(|\uparrow\rangle + 2\,|\downarrow\rangle) \otimes |\downarrow\rangle$. Fidelity $F = \mathrm{Tr}(\rho|\Psi_I\rangle\langle\Psi_I|)$ shows the behavior of the protocol for a given simulated phase θ. The ideal spin dynamics $\langle\sigma_i^x\rangle$ for both qubits is plotted versus mean values $\langle\sigma_i^x\rangle_\rho$ obtained with the qubit Hamiltonian H_t.

Chapter 7

Collective gates and many-body interactions in circuit QED

7.1 Introduction

In this Chapter, we present the implementation of a many-qubit interaction in a superconducting circuit device. We study a set of charge-like qubits provided with tunable coupling to a single microwave waveguide, and analyze their collective behavior under the action of fast flux threading of SQUID loops embedded into them. Among superconducting qubits, transmon qubits are currently the most robust and reliable. They are designed in order to suppress offset charge noise to negligible values [30]. Protocols of quantum information have been implemented, such as error correction up to three qubits [129] and experimental tests of fundamental quantum mechanics [123]. Implementations of quantum simulators of spin and coupled spin-boson systems have been recently proposed [130, 131]. Complex entangled states encoded in superconducting transmon qubits have already been proposed and realized experimentally [132–134]. However, state-of-the-art realizations of many-qubit entangled states still rely on complex sequences of gates, and implementations of effective many-body interactions represent a tough challenge.

The introduction of collective entangling operations in superconducting devices can ease several tasks of quantum information processing. They have been proposed theoretically [13] and realized experimentally in ion traps up to fourteen qubits [135]. By means of collective gates, one can drive the generic many-qubit transition $|00\cdots 0\rangle \rightarrow |11\cdots 1\rangle$ and prepare multipartite Greenberger-Horne-Zeilinger states with a single operation.

The transition can be obtained with effective simultaneous red and blue sidebands acting upon the ions. The latter have been also demonstrated in a variety of superconducting setups [136–138]. Sequences of collective gates, together with local qubit rotations, can i andmplement stabilizer operators [70, 139], that can allow for the implementation of topological codes [140]. Recently it has been shown that collective qubit interactions allow for efficient simulation of fermionic dynamics and coupled fermionic-bosonic systems [60, 71].

We propose the implementation of effective many-body interactions among several tunable-coupling transmons inside a microwave cavity. We consider three-island superconducting devices [141, 142], addressed as tunable-coupling transmon qubits (TCQs), coupled to a coplanar microwave resonator. Then, we show that dynamically sweeping flux biases, acting on two SQUID loops embedded in the three-island devices, it is possible to perform simultaneous red and blue-sideband transitions of many qubits. This leads to effective collective entangling gates that can be used to efficiently obtain many-particle operators. We demonstrate that the third level of the single TCQ can be ruled out of the dynamics. Finally, we validate the proposal with numerical simulations of the system dynamics taking into account a realistic decoherence model.

7.2 Three-island devices for many-body interactions

We start by considering a setup made of a resonator coupled to several TCQs, as in Fig. 7.1a. We show that under specific conditions, the TCQs in the setup behave as two level systems and the effective interaction among them is given by the Hamiltonian

$$H_{I_{\text{eff}}} = -\xi \sum_{i<j} \sigma_i^{\alpha} \sigma_j^{\alpha}. \tag{7.1}$$

Here, ξ is the interaction strength that sets the speed of the transition and the Pauli matrix σ_i^{α}, with either $\alpha = x$ or $\alpha = y$, refers to the subspace spanned by the two lowest energy levels of the i-th TCQ. A single device is composed of three superconducting islands: the upper and lower islands are connected to a central one by means of two SQUID loops. Their effective Josephson couplings $E_{J_\pm}(\Phi_\pm)$ can be tuned by threading the respective superconducting loops with external magnetic fluxes $\Phi_\pm$. In the symmetric limit for the two Josephson junctions of the loops, one has $E_{J_\pm} = E_{J_\pm}^M \cos(\pi\Phi_\pm/\Phi_0)$, where $E_{J_\pm}^M$ is the total Josephson energy of the junctions, Φ_0 being the fundamental flux quantum. The Hamiltonian of the individual TCQ, neglecting the interaction with the resonator, reads $H_T = \sum_\pm 4E_{C\pm}(n_\pm - n'_{g\pm})^2 - \sum_\pm E_{J_\pm}\cos(\gamma_\pm) + 4E_I n_+ n_-$. Here, $\gamma_\pm$ are the gauge invariant phase differences on the upper and lower SQUID loops, $n_\pm$ the charge associated, with the offset charge due to gate voltage bias $n'_{g\pm}$. The charging energies of the upper and lower islands are labeled by $E_{C_\pm}$, while E_I stands for the interaction energy between them. In the limit $E_{J_\pm} \gg E_{C_\pm}$, the charge dispersion of the device is negligible [30]. One can expand to fourth order the cosine potentials associated with the Josephson energies and write the Hamiltonian as a coupled anharmonic oscillator model, $H_{T_{\rm eff}} = \sum_\pm [\omega_\pm + \delta_\pm (b_\pm^\dagger b_\pm - 1)/2] b_\pm^\dagger b_\pm + J(b_+ b_-^\dagger + b_+^\dagger b_-)$. Here, and in the following, we have set $\hbar = 1$. The anharmonicity factors depend on the charging energies $\delta_\pm = -E_{C_\pm}$ and the parameters $\omega_\pm$, $\delta_\pm$ and J are defined in terms of the two external flux biases $\Phi_\pm$ [141].

We consider here that the two external fluxes are changed in time, with some time-dependent functions $\Phi_\pm(t)$. While the fluxes change in time, the parameters in the Hamiltonian $H_{T_{\rm eff}}$ follow accordingly. We apply to $H_{T_{\rm eff}}$ the time-dependent unitary $T(t) = e^{\lambda(t)(b_+ b_-^\dagger - b_+^\dagger b_-)}$, where the phase $\lambda(t)$ is defined instantaneously as a function of the parameters of the time-dependent Hamiltonian $H_{T_{\rm eff}}$. The resulting transformed Hamiltonian $\tilde{H}_{T_d} = T^\dagger(t) H_{T_{\rm eff}} T(t) - iT^\dagger(t)\dot{T}(t)$ reads

$$\begin{aligned}\tilde{H}_{T_d} = \sum_\pm \left[\tilde{\omega}_\pm + \frac{\tilde{\delta}_\pm}{2}(\tilde{b}_\pm^\dagger \tilde{b}_\pm - 1)\right] \tilde{b}_\pm^\dagger \tilde{b}_\pm + \\ \tilde{\delta}_c \tilde{b}_+^\dagger \tilde{b}_+ \tilde{b}_-^\dagger \tilde{b}_- + i\dot{\lambda}(t)(\tilde{b}_+^\dagger \tilde{b}_- - \tilde{b}_+ \tilde{b}_-^\dagger).\end{aligned} \tag{7.2}$$

One can recognize in the above Hamiltonian a diagonal part and an off-diagonal term that results in a small renormalization of the energy levels. The diagonal part reads

$$\tilde{H}_0 = \sum_\pm \left[\tilde{\omega}_\pm + \tilde{\delta}_\pm/2(\tilde{b}_\pm^\dagger \tilde{b}_\pm - 1)\right] \tilde{b}_\pm^\dagger \tilde{b}_\pm + \tilde{\delta}_c \tilde{b}_+^\dagger \tilde{b}_+ \tilde{b}_-^\dagger \tilde{b}_-. \tag{7.3}$$

The first two excited levels of $\tilde{H}_0$ are defined by the occupation of the two modes $\tilde{b}_\pm^\dagger$ and have energies $\tilde{\omega}_\pm$. When the two external magnetic fluxes $\{\Phi_+(t), \Phi_-(t)\}$ are driven in time, the first two excited levels of the Hamiltonian $\tilde{H}_0$ are continuously sweeping between different states in the original basis, as $|\tilde{01}\rangle = \tilde{b}_+^\dagger|00\rangle = \cos(\lambda)|01\rangle + \sin(\lambda)|10\rangle$, $|\tilde{10}\rangle = \tilde{b}_-^\dagger|00\rangle = \cos(\lambda)|01\rangle - \sin(\lambda)|10\rangle$. One can use the two levels $|0\rangle \equiv |00\rangle$ and $|1\rangle \equiv |\tilde{01}\rangle$ as a qubit, see Fig. 7.1b.

7.3 Collective dynamics

We focus now on the interaction term between a single TCQ and the resonator, when the flux biases are varied in time. The TCQs are capacitively coupled to a coplanar resonator, of frequency ω_r. Their interaction can be modeled as $H_I = 2eV_{\rm rms}(\beta_+ n_+ + \beta_- n_-)(-ia^\dagger + ia)$, where the a, $a^\dagger$ operators act on the resonator field. The coupling

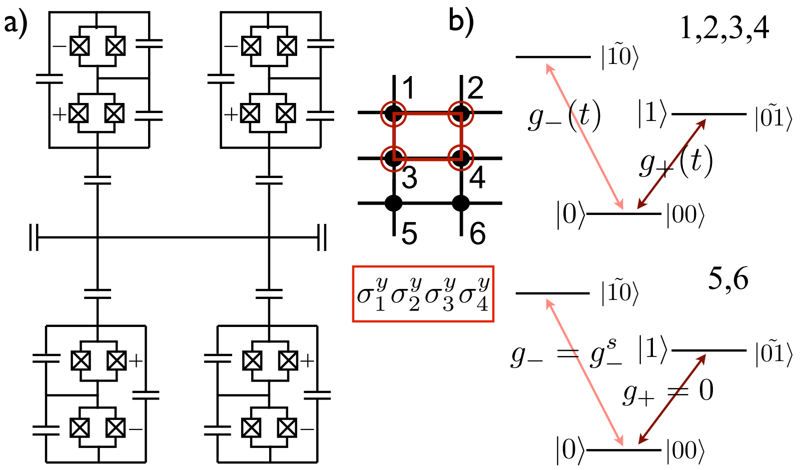

FIGURE 7.1: a) Scheme of a setup composed of four TCQs capacitively coupled to a coplanar resonator. The SQUID loops labeled with + and − can be threaded by external magnetic fluxes. b) Generation of many-particle operator $\sigma_1^y\sigma_2^y\sigma_3^y\sigma_4^y$, between the first, second, third and fourth qubits, see Appendix B. Selectivity is obtained by setting the coupling of the other qubits to the resonator to zero. The qubit logical levels $|0\rangle$ and $|1\rangle$ are the first levels of the TCQ, $|00\rangle$ and $|\tilde{01}\rangle$.

prefactors $\beta_\pm$ are defined by the circuit capacitances, while $V_{\rm rms}$ stands for the root mean square voltage of the resonator. We consider identical capacitances for the upper and lower islands ($\beta_\pm = \beta$). Non-symmetric capacitance configurations do not change the nature of the problem and result in small deviations in the numerical analysis [141]. The interaction can be expressed in the frame of $T(t)$,

$$\tilde{H}_I = \sum_\pm g_\pm(t)(\tilde{b}_\pm^\dagger - \tilde{b}_\pm)(a^\dagger - a). \tag{7.4}$$

We introduce a two-tone driving of the coupling $g_+(t) \equiv 2eV_{\rm rms}\beta\langle 1|\hat{n}|0\rangle$, with $\hat{n} = n_+ + n_-$, between the first two levels of the TCQ and prove later that it can be realized by proper flux drivings,

$$g_+(t) \equiv g_+^s + g_+^d[\cos(\omega_g t) + \cos(\omega_g' t)]. \tag{7.5}$$

Here, we have defined a static contribution g_+^s and a dynamical part, where g_+^d sets the strength of the two-tone ω_g, ω_g' modulation. The frequencies of the coupling are chosen to be detuned by δ with respect to the qubit-resonator sidebands, $\omega_g = \omega_r + \tilde{\omega}_+ - \delta$ and $\omega_g' = \omega_r - \tilde{\omega}_+ - \delta$. Namely, in interaction picture with $\tilde{H}_0$, the effective TCQ-resonator Hamiltonian can be written as (see Appendix B for details)

$$\tilde{H}_I = \tilde{H}_{I_{\rm JC}} + \tilde{H}_{I_+} + \tilde{H}_{I_-}. \tag{7.6}$$

The first term of this Hamiltonian is a Jaynes-Cummings interaction due to the static contributions to the couplings $g_\pm(t)$, $\tilde{H}_{I_{\rm JC}} = -\sum_\pm g^s_\pm(\tilde{b}_\pm a^\dagger + \tilde{b}^\dagger_\pm a)$, which results in an effective interaction of coupling strength $(g^s_\pm)^2/\Delta_\pm$, where $\Delta_\pm = \tilde{\omega}_\pm - \omega_r$ is the detuning of the first two TCQ levels from the resonator frequency. The second and third terms of the right side of Eq. (7.6) $\tilde{H}_{I_\pm}$ involve the dynamical contribution to the coupling terms, proportional to $g^d_\pm$. The term acting on the first two levels, imposing the condition of Eq. (7.5), reads

$$\tilde{H}_{I_+} = g^d_+ \big[\cos(\omega_g t) + \cos(\omega'_g t)\big](\tilde{b}^\dagger_+ - \tilde{b}_+)(a^\dagger - a). \tag{7.7}$$

Neglecting fast oscillating terms, Eq. (7.7) reduces to $\tilde{H}_{I_+} \approx i(g^d_+/2)\Big(a^\dagger e^{i\delta t} - a e^{-i\delta t}\Big)\sigma^y$, where σ^y is a Pauli matrix acting on the Hilbert space spanned first the two levels of the device. The third contribution to the dynamics, $\tilde{H}_{I_-}$ in Eq. (7.6), has several terms oscillating at different frequencies. If none of them is close to the third level sidebands, contribution from $\tilde{H}_{I_-}$ will be negligible and leakage to the third level will be suppressed. In fact, when the dynamical detuning is much smaller than qubit-resonator one, $(g^s_\pm)^2/\Delta_\pm \ll (g^d_+)^2/4\delta$, the dynamics will be dominated by $\tilde{H}_{I_+}$. A small Stark-Lamb shift term $\sum_j[(g^s_+)^2/\Delta_+]\sigma^z_j(\frac{1}{2} + a^\dagger a)$, can be considered negligible, taking into account small cavity population and renormalization of the qubit frequencies. Provided with TCQ-resonator interactions as in Eq. (7.6), one can build multi-qubit setups, where the effective total Hamiltonian reads

$$\tilde{H}_{I_{\rm eff}} = \sum_j i\frac{g_b}{2}\Big(a^\dagger e^{i\delta t} - a e^{-i\delta t}\Big)\sigma^y_j, \tag{7.8}$$

where σ^y_j refers to the first two levels of the j-th TCQ. The evolution operator associated with the global Hamiltonian in Eq. (7.8) can be exactly solved, computing a Magnus expansion at second order, see Appendix B. The qubit dynamics gets entangled with the photons in the resonator, and at times $\tau_n = 2\pi n/\delta$, with integer n, the dynamics is detached from the photons and it follows the Hamiltonian in Eq. (7.1). The global interaction in Eq. (7.1) is a collective entangling operation between many two level systems. It can be used to obtain many-qubit GHZ states at specific times, starting from a configuration in which all the qubits are initialized in the lowest level [13]. By choosing appropriate initial phases, one can map the dynamics onto $H_{I_{\rm eff}} = -\xi\sum_{i<j}\sigma^x_i\sigma^x_j$. In general, one can retrieve the dynamics of many-body operators of the form $\sigma^i_1\sigma^j_2\cdots\sigma^k_N$, with $\{i, j, ...k\} \in \{x, y, z\}$ [70], up to local qubit rotations. The selectivity upon a generic set of qubits is obtained by setting the coupling between the first two levels to $g_+ = 0$. The corresponding third level static coupling $g_- = g^s_-$ will not contribute to the dynamics due to the large detuning between the third level and the resonator frequencies.

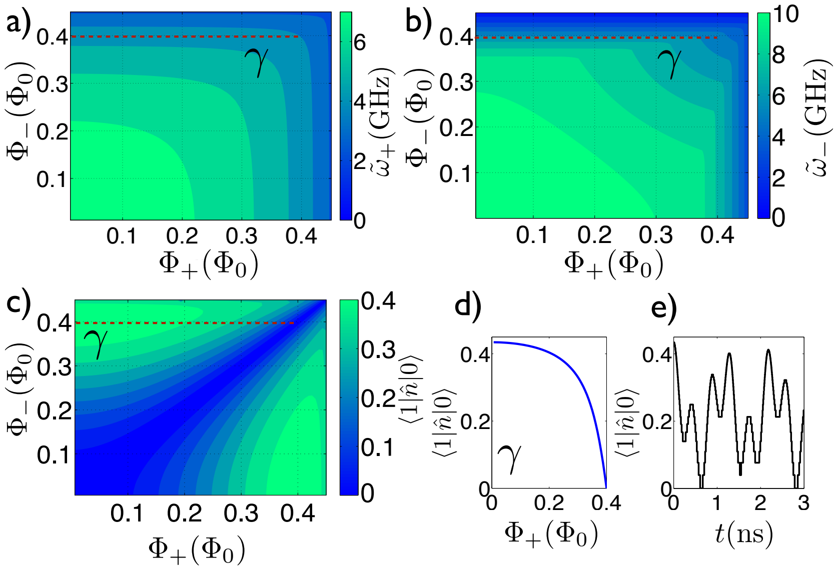

FIGURE 7.2: a) Transition frequency between the first two levels of the TCQ and b) between the ground state and the third level, as a function of the magnetic fluxes Φ_+ and Φ_-. c) Matrix element $\langle 1|\hat{n}|0\rangle$. d) Variation of $\langle 1|\hat{n}|0\rangle$ along γ. e) The magnetic flux is varied in time to obtain the time dependence $g_+(t) = g_+^s + g_+^d[\cos(\omega_g t) + \cos(\omega_g' t)]$.

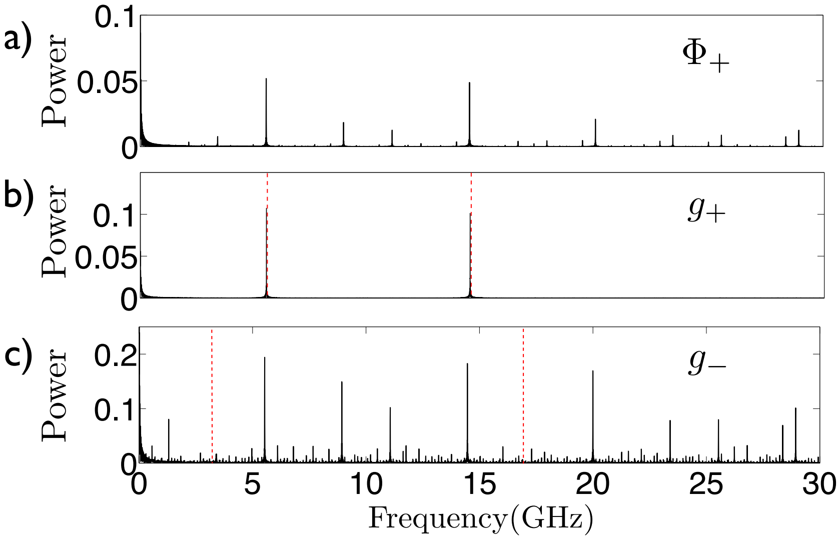

FIGURE 7.3: a) Numerical power spectrum of the magnetic signal $\Phi_+(t)$, used to obtain $g_+(t)$. b) Power spectrum of $g_+(t)$, obtained by plugging the signal $\Phi_+(t)$. The spectrum has two resonances at ω_g, ω_g', close to the two sidebands at $\omega_r - \tilde{\omega}_+ = 5.5$ GHz and $\omega_r + \tilde{\omega}_+ = 14.5$ GHz (red dotted lines). c) Power spectrum of $g_-(t)$, with the sidebands $\omega_r - \tilde{\omega}_- = 3$ GHz and $\omega_r + \tilde{\omega}_- = 17$ GHz (red dotted lines).

7.4 Analysis of parameters of circuit QED

One can tune in time the coupling, as in Eq. (7.5), by modulating the external magnetic fluxes $\Phi_\pm$. In general, this will also have an influence on the energy of the first two excited levels. To retain a proper coherent dynamics, one can choose appropriate time-dependent flux drivings such that the coupling has the desired strength, while the qubit transition frequency $\tilde{\omega}_+$ is constant. To give an example, we choose $E_{C_\pm} = 500$ MHz, $E_I = 350$ MHz and $E_{J_\pm} = 25$ GHz and plot numerically in Fig 7.2a and 7.2b, respectively, transition frequencies between the first two levels and the first and the third one, as a function of the flux biases $\{\Phi_+, \Phi_-\}$. For the same parameters, in Fig. 7.2c, is plotted the matrix element $\langle 1|\hat{n}|0\rangle$. Along the curve γ, approximated by the segment at constant $\Phi_- = 0.4\Phi_0$ and $\Phi_+ \in [0, 0.4]\Phi_0$, the transition frequencies are constant, while $\langle 1|\hat{n}|0\rangle$ ranges between a maximum value at $\langle 1|\hat{n}|0\rangle^M \simeq 0.45$ at $\Phi_+ = 0$ and a minimum at $\langle 1|\hat{n}|0\rangle^m = 0$ at $\Phi_+ = 0.4\Phi_0$, as in Fig. 7.2d. The coupling range between $\langle 1|\hat{n}|0\rangle^M$ and $\langle 1|\hat{n}|0\rangle^m$ can be used to encode the time dependent coupling behavior as in Eq. (7.5). One can design an overall capacitance prefactor β such that, e.g., $2eV_{\mathrm{rms}}\beta\langle 1|\hat{n}|0\rangle^M = g_+^M = 80$ MHz. Then one can set $g_+^s \equiv (g_+^M + g_+^m)/2 = 40$ MHz ($g_+^m = 0$) and $g_+^d \equiv (g_+^M - g_+^m)/4 = 20$ MHz. By changing $\Phi_+(t)$ along the curve in time, one can encode the proper time-dependence of the coupling. Notice that the range in which one can drive the magnetic flux is limited by the validity of the negligible charge dispersion regime and by the coupled anharmonic oscillator model, used to describe the TCQ. In fact, large magnetic fluxes will decrease the effective Josephson energies of the SQUID loops, breaking the regime $E_{J_\pm} \gg E_{C_\pm}$.

Along γ, one has $\tilde{\omega}_+ = 4.5$ GHz and $\tilde{\omega}_- = 7$ GHz. Furthermore, one can choose $\delta = 50$ MHz and consider a resonator frequency of 10 GHz. The magnetic signal $\Phi_+(t)$ that gives the coupling in Eq. (7.5) is obtained by inverting the function in Fig 7.2d, for every time t. The coupling, for a sample time interval, is plotted in Fig. 7.2e. We then decompose the signal $\Phi_+(t)$ in its Fourier components. Applying the magnetic signal $\Phi_+(t)$, also the coupling between the first and the third level $g_-(t)$ undergoes fast oscillations. We obtain numerically the time dependence of $g_-(t)$, when the flux $\Phi_+(t)$ is plugged into the system. Considering $g_+^s = 40$ MHz, one has a static contribution for $g_-(t)$ of $g_-^s = 60$ MHz. The power spectra of $g_+(t)$ and $g_-(t)$ are plotted in Fig 7.3b and 7.3c. As expected, $g_+(t)$ has only two Fourier components around $\omega_g = 14.45$ GHz, $\omega_g' = 5.45$ GHz, detuned by δ from the qubit-resonator sidebands. On the other hand, $g_-(t)$ has no Fourier component close to the resonator-third level sidebands, at 3 GHz and 17 GHz. Thus, leakage to the third level of the TCQ will not affect the dynamics. The setup can therefore be regarded as an effective two-level system that undergoes red-detuned and blue-detuned sideband interactions. Furthermore, one can prove that standard Jaynes-Cummings interactions do not affect in a relevant way the dynamics.

Considering that one can maximize the dynamical interaction and choose $g^s_+ = 2g^d_+$, the condition for neglecting $H_{I_{\mathrm{JC}}}$ in Eq. (7.6), $(g^s_+)^2/\Delta_+ \ll (g^d_+)^2/4\delta$, can be formulated in terms of the ratio $\Delta_+/\delta \gg 16$. Thus, using higher frequency transitions will improve the fidelity of the gate. To prove this, we perform numerical simulation of the dynamics driven by the interaction Hamiltonian in Eq. (7.6), in interaction picture with $\tilde{H}_0$. We consider the first three levels for each TCQ. We integrate numerically a Lindblad master equation for the dynamics of four TCQs and resonator, $\dot{\rho} = -i[H_{I_{\mathrm{eff}}}, \rho] + \kappa L(a)\rho + \sum_{i=1}^4 [\Gamma_\phi L(\sigma^z_i)\rho + \Gamma_- L(\sigma^-_i)\rho]$, adding Lindblad superoperators for the i-th qubit $\Gamma_\phi L(\sigma^z_i)\rho$, $\Gamma_- L(\sigma^-_i)\rho$ to take into account dephasing and relaxation rates and $\kappa L(a)\rho$ to take into account resonator losses. Here, $L(A)\rho = (2A\rho A^\dagger - A^\dagger A\rho - \rho A^\dagger A)/2$. We set $\kappa = 100$ KHz, $\Gamma_\phi, \Gamma_- = 20$ KHz. We use the time-dependent couplings $g_+(t)$, $g_-(t)$ as obtained in Fig. 7.3. The overall magnitude of the qubit-resonator interaction is set to $g^d_+ = 20$ MHz, $g^s_+ = 40$ MHz, $g^s_- = 60$ MHz. We choose $\delta = 50$ MHz. The transition frequencies for the first two levels of the TCQ are $\tilde{\omega}_+ = 4.5$ GHz and $\tilde{\omega}_- = 7$ GHz. The diagonalizing phase $\lambda(t)$ has a fast oscillating contribution. Its effect can be estimated in a small renormalization of the qubit frequency. In fact, the last term in Eq. (7.2) will result, in interaction picture with respect to $\tilde{H}_0$ and neglecting first-order fast-oscillating contribution, into an effective second-order small renormalization of the free energies, leading to $\tilde{\omega}^R_\pm = \tilde{\omega}_\pm + \tilde{\omega}_{\pm\lambda}$, where $\tilde{\omega}_{\pm\lambda} = \lambda_d^2\omega_\lambda^2 \cdot (\tilde{\omega_+} - \tilde{\omega}_-)/2[(\tilde{\omega}_+ - \tilde{\omega}_-)^2 - \omega_\lambda^2]$ and ω_λ is a frequency of the diagonalizing parameter $\lambda(t)$. The detuning ratio is approximately $\Delta_+/\delta \sim 100$. Fig. 7.4a shows the fidelity peaks at $\tau_n = 2\pi n/\delta$ for the simulated density matrix ρ versus the ideal qubit dynamics, $|\Psi_I\rangle$, that follows the Hamiltonian in Eq. (7.1), with $\xi = (g^d_+)^2/4\delta$. In Fig. 7.4b, the same dynamics is integrated considering two different resonator frequencies. One can notice that, as the qubit-resonator detuning increases, the fidelity peaks get higher as the Jaynes-Cummings part of Eq. (7.6) is better suppressed.

To perform readout, one can fix $g_+(t) = g^s_+$ and implement standard dispersive measurement with a resonator pull of $\pm(g^s_+)^2/\Delta_+$ depending on the state of the single TCQ [32]. For the practical implementation of this interaction, specific designed flux drivings can take into account inhomogeneous qubit transition frequencies and couplings, by choosing different flux driving trajectories.

In conclusion, we have shown that a setup made out of several superconducting three-island devices, provided with tunable coupling to a coplanar waveguide resonator, may realize collective gates and many-body interactions among superconducting qubits.

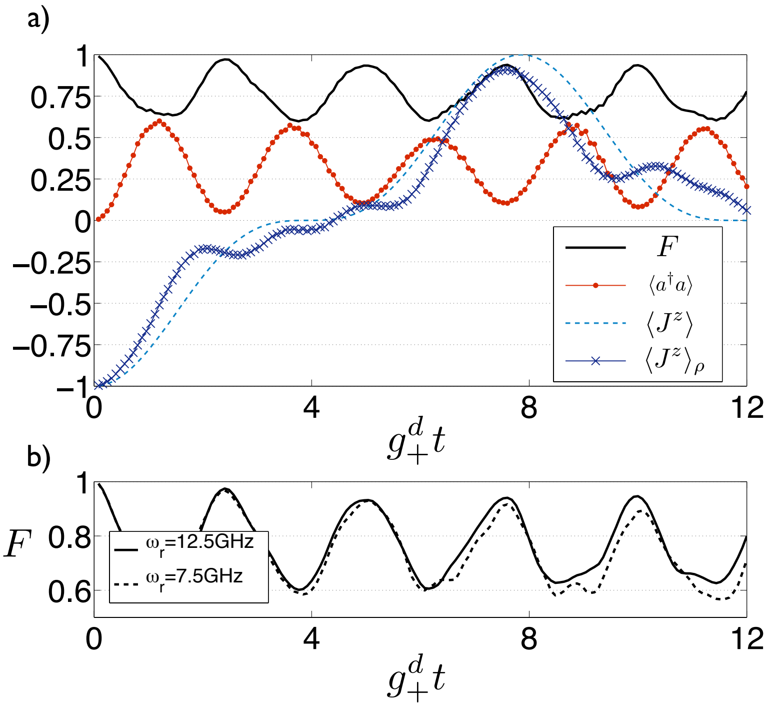

Figure 7.4: a) Collective entanglement between four TCQs, intialized in their ground states. The ideal state $|\Psi_I\rangle$ follows the dynamics regulated by the Hamiltonian of Eq. (7.1), with $\xi = (g_+^d)^2/4\delta$. The fidelity $F = \mathrm{Tr}[\rho|\Psi_I\rangle\langle\Psi_I|]$ of the TCQ dynamics is plotted, along with mean number of photons $\langle a^\dagger a\rangle$. The ideal mean value of the collective spin oscillation $\langle J_z\rangle$, $J_z = 1/4\sum_{i=1}^4 \sigma_i^z$, is compared with the TCQ one $\langle J_z\rangle_\rho$. b) Fidelities for different resonator frequencies. The fidelity improves as the qubit-resonator detuning increases. The first two peaks have values $F \approx 0.97, 0.93$.

These interactions can be used to implement topological codes and efficiently simulate fermionic dynamics in circuit QED setups.

Chapter 8

Quantum Rabi and Dicke models in superconducting circuits

8.1 Introduction

In this Chapter, we propose the Digital-analog quantum simulation of the quantum Rabi and Dicke models using cQED. We find that all physical regimes, in particular those which are impossible to realize in typical cavity QED setups, can be simulated via unitary decomposition into digital steps. The simplest, most fundamental interaction of quantum light and quantum matter can be described by the quantum Rabi model, consisting of the dipolar coupling of a two-level system with a single radiation mode [143]. The Dicke model [144] was later introduced to generalize this interaction to an ensemble of N two-level systems. Typically, the coupling strength is small compared to the transition frequencies of the two-level system and the radiation mode, leading to effective Jaynes-Cummings and Tavis-Cummings interactions, respectively, after performing a rotating-wave approximation (RWA). This introduces a $U(1)$ symmetry and integrability to the model for any N [145, 146]. Recently, analytical solutions for the generic quantum Rabi and Dicke model for $N = 3$ were found [147, 148]. However, the general case for arbitrary N is still unsolved, while its direct study in a physical system remains an outstanding challenge.

A variety of quantum platforms, such as cavity QED, trapped ions, and circuit QED, provides a natural implementation of the Jaynes-Cummings and Tavis-Cummings models, due to the weak qubit-mode coupling strength. When the latter is a fraction or comparable to the mode frequency, the model is said to be in the ultrastrong coupling (USC) regime. Experimental evidence of this regime has been observed in the optical [149] and microwave domains [150, 151]. Coupling strengths larger than the

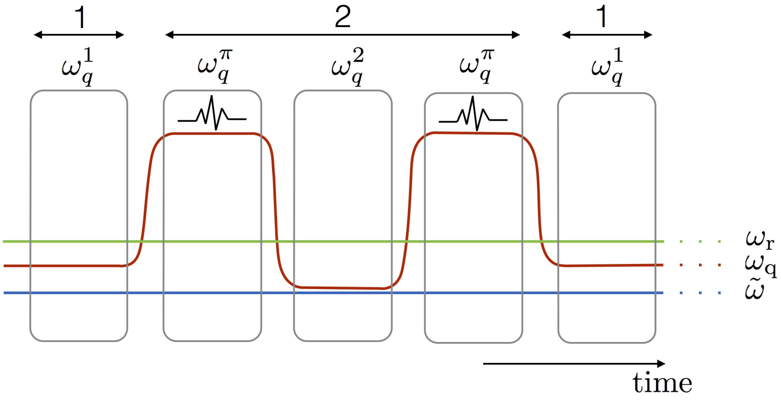

Figure 8.1: Frequency scheme of the stepwise implementation for the quantum Rabi Hamiltonian. A transmon qubit of frequency ω_q is interacting with a microwave resonator, whose transition frequency is ω_r. The interactions $H_{1,2}$ in Eq. (8.3) are simulated respectively with a Jaynes-Cummings interaction (step 1), and another one with different detuning, anticipated and followed by π pulses (step 2).

mode frequency mark the transition towards the recently introduced deep-strong coupling (DSC) regime [152]. An experimental observation of the full quantum Rabi and Dicke models in all parameter regimes has not yet been realized. In particular, the quantum simulation [2] of the Dicke Hamiltonian could outperform analytical and numerical methods, while enabling the simulation of engineered super-radiant phase transitions [153–155]. Recently, technological improvements of controlled quantum platforms have increased the interest in quantum simulations [4–6, 36]. A digital approach to quantum simulations was put forward in Ref. [24]. In this sense, it has been analyzed how suitable versions of digital quantum simulators can be implemented with available quantum platforms [25, 60, 71, 130]. Standard digital quantum simulations focus on the efficient decomposition of the quantum system dynamics in terms of elementary gates. In order to maximize the efficiency of the simulation, one may analyze which is the decomposition of the dynamics in its largest realizable parts, and reduce the number of elementary interactions in the simulation. This approach can be labeled as digital-analog quantum simulation and corresponds to finding some terms in the simulated system that can be implemented in an analog way, e.g., to employ a harmonic oscillator to simulate a bosonic field, while others will be carried out with a digital decomposition.

We propose the digital-analog quantum simulation of the quantum Rabi and Dicke models in a circuit QED setup, provided only with Jaynes-Cummings and Tavis-Cummings interactions, respectively. We show how the rotating and counter-rotating contributions to the corresponding dynamics can be effectively realized with digital techniques. By interleaved implementation of rotating and counter-rotating steps, the dynamics of the quantum Rabi and Dicke models can be simulated for all parameter regimes with negligible error. Lastly, we show how a relativistic Dirac dynamics can be retrieved in the limit where the mode frequency cancels.

Table 8.1: Simulated quantum Rabi dynamics parameters versus frequencies of the system. For all entries in the right column, the resonator frequency is fixed to $\omega_r/2\pi = 7.5$ GHz, and the coupling $g^R/2\pi = 100$ MHz. Frequencies are shown up to a 2π factor.

$g^R = \omega_q^R/2 = \omega_r^R/2$	$\tilde{\omega} = 7.4$ GHz, $\omega_q^1 - \omega_q^2 = 200$ MHz
$g^R = \omega_q^R = \omega_r^R$	$\tilde{\omega} = 7.45$ GHz, $\omega_q^1 - \omega_q^2 = 100$ MHz
$g^R = 2\omega_q^R = \omega_r^R$	$\tilde{\omega} = 7.475$ GHz, $\omega_q^1 - \omega_q^2 = 100$ MHz

8.2 Digital-analog decomposition of the Rabi model

We start by considering a generic circuit QED setup consisting of a charge-like qubit, e.g. a transmon qubit [30], coupled to a microwave resonator. The setup is well described by the Hamiltonian ($\hbar = 1$) [32]

$$H = \omega_r a^\dagger a + \frac{\omega_q}{2}\sigma^z + g(a^\dagger\sigma^- + a\sigma^+), \tag{8.1}$$

where ω_r and ω_q are the resonator and qubit transition frequencies, g is the resonator-qubit coupling strength, $a^\dagger(a)$ is the creation(annihilation) operator for the resonator mode, and $\sigma^\pm$ raise and lower excitations on the qubit. The capacitive interaction in Eq. (8.1) excludes excitations of the higher levels of the qubit device, because typically the coupling g is much smaller than other transition frequencies of the system. By trying to design setups with larger capacitive couplings, pushing them above dispersive regimes, one starts to populate the higher levels of the transmons, producing unwanted leakage. Here, we show that the dynamics of the quantum Rabi Hamiltonian

$$H_R = \omega_r^R a^\dagger a + \frac{\omega_q^R}{2}\sigma^z + g^R\sigma^x(a^\dagger + a) \tag{8.2}$$

can be encoded in a superconducting setup provided with a Jaynes-Cummings interaction, as in Eq. (8.1), using a digital expansion.

The quantum Rabi Hamiltonian in Eq. (8.2) can be decomposed into two parts, $H_R = H_1 + H_2$, where

$$\begin{aligned} H_1 &= \frac{\omega_r^R}{2}a^\dagger a + \frac{\omega_q^1}{2}\sigma^z + g(a^\dagger\sigma^- + a\sigma^+), \\ H_2 &= \frac{\omega_r^R}{2}a^\dagger a - \frac{\omega_q^2}{2}\sigma^z + g(a^\dagger\sigma^+ + a\sigma^-), \end{aligned} \tag{8.3}$$

and we have defined the qubit transition frequency in the two steps such that $\omega_q^1 - \omega_q^2 = \omega_q^R$. These two interactions can be simulated in a typical circuit QED device with fast control of the qubit transition frequency. Starting from the qubit-resonator Hamiltonian in Eq. (8.1), one can define a frame rotating at frequency $\tilde{\omega}$, in which the effective

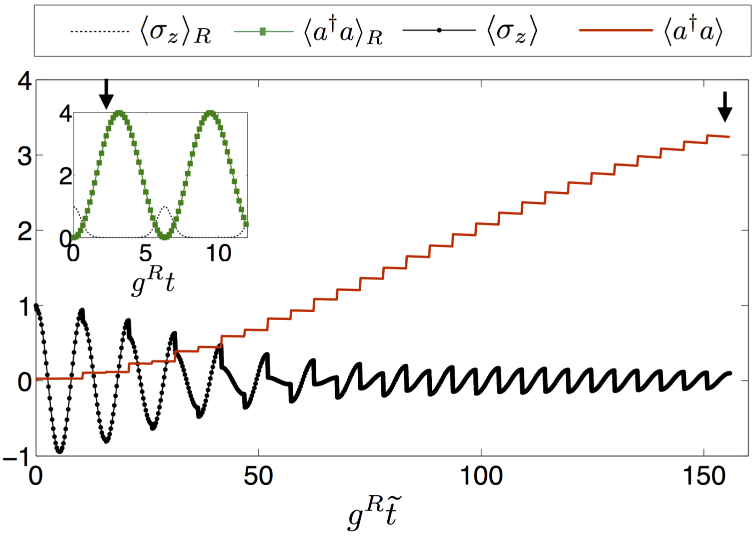

FIGURE 8.2: A transmon qubit and microwave resonator simulating the quantum Rabi Hamiltonian in the regime $g^R = \omega_r^R$, $\omega_q^R = 0$. The ideal dynamics, plotted in the inset, shows collapses and revivals of the photon and qubit population. The latter are recovered via sequential qubit-resonator interactions and qubit flips. The photon population is pumped to the expected value at the time marked by the arrow. Note that the simulating time $\tilde{t}$ is different from the simulated time t.

interaction Hamiltonian becomes

$$\tilde{H} = \tilde{\Delta}_r a^\dagger a + \tilde{\Delta}_q \sigma^z + g(a^\dagger \sigma^- + a\sigma^+), \tag{8.4}$$

with $\tilde{\Delta}_r = (\omega_r - \tilde{\omega})$ and $\tilde{\Delta}_q = (\omega_q - \tilde{\omega})/2$. Therefore, Eq. (8.4) is equivalent to H_1, following a proper redefinition of the coefficients. The counter-rotating term H_2 can be simulated by applying a local qubit rotation to $\tilde{H}$ and a different detuning for the qubit transition frequency,

$$e^{-i\pi\sigma^x/2}\tilde{H}e^{i\pi\sigma^x/2} = \tilde{\Delta}_r a^\dagger a - \tilde{\Delta}_q \sigma^z + g(a^\dagger \sigma^+ + a\sigma^-). \tag{8.5}$$

By choosing different qubit-resonator detuning for the two steps, $\tilde{\Delta}_q^1$ for the first one and $\tilde{\Delta}_q^2$ for the rotated step, one is able to simulate the quantum Rabi Hamiltonian, Eq. (8.2), via digital decomposition [24], by interleaving the simulated interactions. The frequency scheme of the protocol is shown in Fig. 8.1. Standard resonant Jaynes-Cummings interaction parts with different qubit transition frequencies are interrupted by microwave pulses, in order to perform customary qubit flips. This sequence can be repeated according to the digital simulation scheme to obtain a better approximation of the quantum Rabi dynamics.

8.3 Circuit QED implementation

The simulated Rabi parameters can be obtained as a function of the physical parameters of the setup by inverting the derivation presented above. In this way, one has that the simulated bosonic frequency is related to the resonator detuning $\omega_r^R = 2\tilde{\Delta}_r$, the two-level transition frequency is related to the transmon frequency in the two steps, $\omega_q^R = \tilde{\Delta}_q^1 - \tilde{\Delta}_q^2$, and the coupling to the resonator remains the same, $g^R = g$. Notice that even if the simulated two-level frequency ω_q^R depends only on the frequency difference, large detunings $\tilde{\Delta}_q^{1(2)}$ will affect the total fidelity of the simulation. In fact, since the digital error depends on the magnitude of individual commutators between the different interaction steps, using larger detunings linearly increases the latter, which results in fidelity loss of the simulation. To minimize this loss, one can choose, for example, the transmon frequency in the second step to be tuned to the rotating frame, such that $\tilde{\Delta}_q^2 = 0$. Nevertheless, to avoid sweeping the qubit frequency across the resonator frequency, one may choose larger detunings. To estimate the loss of fidelity due to the digital approximation of the simulated dynamics, we consider a protocol performed with typical transmon qubit parameters [30]. We estimate a resonator frequency of $\omega_r/2\pi = 7.5$ GHz, and a transmon-resonator coupling of $g/2\pi = 100$ MHz. The qubit frequency ω_q and the frequency of the rotating frame $\tilde{\omega}$ are varied to reach different parameter regimes.

To perform the simulation for the quantum Rabi model with $g^R/2\pi = \omega_q^R/2\pi = \omega_r^R/2\pi = 100$ MHz, for example, one can set $\omega_q^1/2\pi = 7.55$ GHz, $\omega_q^2/2\pi = 7.45$ GHz. In this way, one can define an interaction picture rotating at $\tilde{\omega}/2\pi = 7.45$ GHz to encode the dynamics of the quantum Rabi model with minimal fidelity loss. Considering that single-qubit rotations take approximately ~ 10 ns, tens of Trotter steps could be comfortably performed within the coherence time. Notice that, in performing the protocol, one has to avoid populating the third level of the transmon qubit. Considering transmon anharmonicities of about $\alpha = -0.1$, for example, in this case one has third level transition frequencies of 6.795 GHz and 6.705 GHz. Therefore, given the large detuning with the resonator, it will not be populated. Similarly, by choosing different qubit detunings and rotating frames, one can simulate a variety of parameter regimes, e.g. see Table 8.1.

8.4 Numerical analysis

In order to capture the physical realization of the simulation, we plot in Fig. 8.2 the behavior of the transmon-resonator system during the simulation protocol. We numerically integrate a master equation, alternating steps of Jaynes-Cummings interaction with

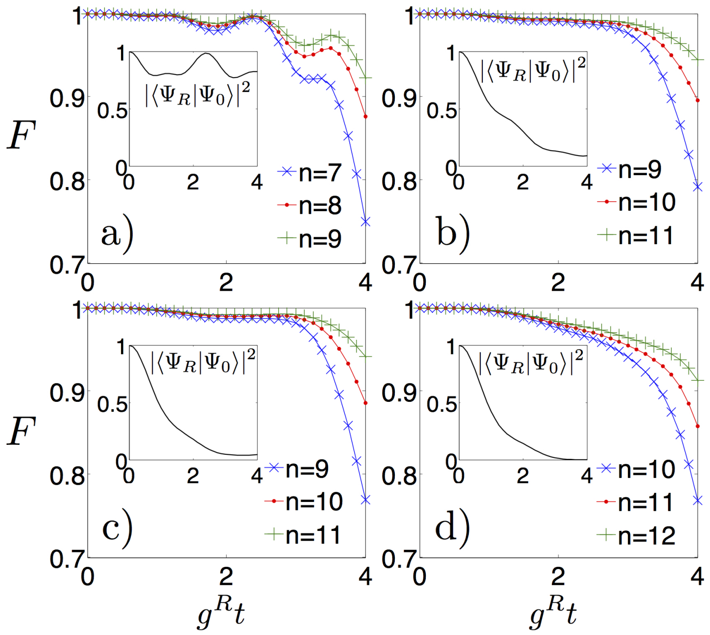

FIGURE 8.3: Time evolution of the fidelity $F = |\langle\Psi_S|\Psi_R\rangle|^2$ of state $|\Psi_S\rangle$ evolving according to the digitized protocol, to the ideal state $|\Psi_R\rangle$ evolving according to the quantum Rabi dynamics, with a) $g^R = \omega_r^R/2 = \omega_q^R/2$, b) $g^R = \omega_r^R = \omega_q^R$, c) $g^R = 2\omega_r^R = \omega_q^R$, and d) $g^R = 2\omega_r^R = 1.5\omega_q^R$. The simulation is performed for different number n of Trotter steps. Black curves in the insets show the overlap of the ideal evolved state with the one at time $t = 0$, $|\langle\Psi_R|\Psi_0\rangle|^2$, initialized with a fully excited qubit and the resonator in the vacuum state.

single-qubit flip pulses. We consider $\dot{\rho} = -i[H,\rho] + \kappa L(a)\rho + \Gamma_\phi L(\sigma^z)\rho + \Gamma_- L(\sigma^-)\rho$, with Jaynes-Cummings terms $\tilde{H} = \tilde{\Delta}_r a^\dagger a + \tilde{\Delta}_q \sigma^z + g(a^\dagger\sigma^- + a\sigma^+)$, alternated with qubit-flip operations $H_f = f(t)\sigma^x$, where $f(t)$ is a smooth function such that $\int_0^{T_f} f(t)dt = \pi/2$, T_f being the qubit bit-flip time. The quantum dynamics is affected by Lindblad superoperators $\Gamma_\phi L(\sigma^z)\rho$, $\Gamma_- L(\sigma^-)\rho$, and $\kappa L(a)\rho$ modelling qubit dephasing, qubit relaxation and resonator losses. We have defined $L(A)\rho = (2A\rho A^\dagger - A^\dagger A\rho - \rho A^\dagger A)/2$. We set a resonator-qubit coupling of $g/2\pi = 80$ MHz, and a frame rotating at the qubit frequency, $\tilde{\Delta}_q = 0$, $\tilde{\Delta}_r/2\pi = 40$ MHz. We consider $\Gamma_-/2\pi = 30$ kHz, $\Gamma_\phi/2\pi = 60$ kHz, and $\kappa/2\pi = 100$ kHz. The inset of Fig. 8.2 shows collapses and revivals of both the photon and spin dynamics, which are typical signatures of the regimes of the quantum Rabi dynamics dominated by the coupling strength. We consider prototypical DSC dynamics, with $\omega_q^R = 0$, and $g^R = \omega_r^R$. Notice that to encode the dynamics corresponding to a certain simulated time t, one needs the quantum simulator to run for a simulating time $\tilde{t}$, that depends on the specific gate times of the experiment. We choose to set the simulation at the time marked by the black arrow, close to the photon population peak in the inset. A simulation with 15 digital steps is then performed. The time for a single qubit flip pulse is set to $T_f = 10$ ns. Periodic collapses and revivals of the bosonic population of the quantum Rabi model $\langle a^\dagger a\rangle_R$ are shown as a function of time, in the inset. The ideal spin and bosonic populations $\langle\sigma_z\rangle_R$ and $\langle a^\dagger a\rangle_R$, evolving according to the quantum Rabi Hamiltonian, are shown to be in good agreement with the simulated ones, $\langle \sigma_z \rangle$ and $\langle a^\dagger a \rangle$, at the final simulated time. In fact, during the Jaynes-Cummings interaction parts, photons are pumped into the resonator. Afterwards, before the photon population starts to decrease due to excitation exchanges with the transmon qubit, a qubit flip further enhances the photon production.

The simulation protocol can be performed for every time of the dynamics, with the number of digital steps tuned to reach a satisfactory simulation fidelity. We plot in Fig. 8.3 the fidelity $F = |\langle \Psi_S | \Psi_R \rangle|^2$ as a function of time of the simulated wavefunction Ψ_S, including resonator and spin degrees of freedom, versus the ideal one Ψ_R, evolving according to H_R, as defined in Eq. (8.2). The fidelity is plotted for different parameters and iteration steps. Increasing the number of steps, the fidelity grows as expected from standard Suzuki-Lie-Trotter expansions [40]. In principle, the whole protocol can accurately access non-analytical regimes of these models, including USC and DSC regimes.

8.5 Dicke model and furher developments

By adding several transmon qubits to the architecture, the presented method can be extended to simulate the Dicke Hamiltonian

$$H_D = \omega_r^R a^\dagger a + \sum_{j=1}^{N} \frac{\omega_q^R}{2} \sigma_j^z + \sum_{j=1}^{N} g^R \sigma_j^x (a^\dagger + a). \tag{8.6}$$

This simulation can be efficiently implemented by means of collective qubit rotations. In fact, only collective Tavis-Cummings interactions and global qubit rotations are involved. In this way, the total time for the simulation does not scale with the size of the system N. The Dicke model can be investigated provided enough coherence and low-enough gate errors. Notice that this kind of quantum simulation is well suited for superconducting circuits, since simultaneous single-qubit addressing is possible. Making use of the results in Ref. [80], we demonstrate that the quantum resources needed to approximate the Dicke Hamiltonian with an error less than ϵ scale efficiently with the number of spins N and of excitations allowed in the bosonic mode M. In a Dicke model simulation, one can bound the number of gates N_ϵ necessary to achieve a certain error ϵ in a time t by

$$N_\epsilon \leq \frac{2 \cdot 5^{2k} \left\{ 2t[\omega_r^R M + N(\omega_q^R + 2|g^R|\sqrt{M+1})] \right\}^{1+1/2k}}{\epsilon^{1/2k}}. \tag{8.7}$$

Here, we have used an upper bound for the norm of the Dicke Hamiltonian, $||H_R|| \leq \omega_r^R M + N(\omega_q^R + 2|g^R|\sqrt{M+1})$, where M is a truncation on the number of bosonic excitations involved in the dynamics. The fractal depth is set to $k = 1$ in the standard Trotter approximations. Using higher orders of fractal decompositions would be a more involved task for implementation of digital approximations in realistic devices, due to the sign inversion that appears [40]. Nevertheless, unitary approximants with arbitrarily high fidelity can be obtained even when $k = 1$. The formula in Eq. (8.7) gives an upper bound to the scaling of quantum resources and experimental errors in a simulation involving several qubits. In fact, if one considers a small error for each gate, the accumulated gate error grows linearly with the number of gates.

Notice that the quantum dynamics of the Dirac Hamiltonian emerges as a specific case of the quantum Rabi dynamics. For the 1+1 dimensional case the algebra of the Dirac spinors $|\Psi\rangle$ corresponds to that of Pauli matrices, and the Dirac equation in the standard representation can be written

$$i\frac{d}{dt}\left|\Psi\right\rangle = \left(mc^2\sigma_z + cp\sigma_x\right)\left|\Psi\right\rangle , \tag{8.8}$$

where m is the mass of the particle, c is the speed of light and $p \propto (a - a^\dagger)/i$ is the one-dimensional momentum operator. The Dirac Hamiltonian in Eq. (8.8), $H_{\mathrm{D}} = mc^2\sigma_z + cp\sigma_x$, shows the same mathematical structure as the quantum Rabi Hamiltonian, Eq. (8.2), when $\omega_r^R = 0$. This condition can be achieved by choosing $\tilde{\omega} = \omega_r$. The analogy is complete by relating mc^2 to $\omega_q^R/2$, c to g^R, and the momentum to the quadrature of the microwave field, which can be measured with current microwave technology. Choosing an initial state with components in both positive and negative parts of the Dirac spectrum will allow the measurement of the *Zitterbewegung* [19]. By retrieving different quadratures of the microwave field, one can detect this oscillatory motion of the simulated particle in the absence of forces, and the Klein paradox, where a relativistic particle can tunnel through high-energy barriers. To detect such effects, one will be interested in measuring either the position or the momentum of the particle, standing for different quadratures of the microwave field.

Part III

Quantum simulations of complex classical systems

Chapter 9

A quantum simulator for fluid dynamics

9.1 Introduction

The quantum simulation of classical dynamics is a rather unexplored field. Encoding a classical dynamics into a quantum one is a non-trivial task. In this Chapter, we approach the simulation of fluid dynamics using a quantum simulator, by proposing a quantum simulator based on pseudospin-boson quantum systems, which is suitable for encoding fluid dynamics problems within a lattice kinetic formalism. This quantum simulator is obtained by exploiting the analogies between Dirac and lattice Boltzmann equations. It is shown that both the streaming and collision processes of lattice Boltzmann dynamics can be implemented with controlled quantum operations, using a heralded quantum protocol to encode non-unitary scattering processes. The proposed simulator is amenable to realization in controlled quantum platforms, such as ion-trap quantum computers or circuit quantum electrodynamics processors.

Transport phenomena in fluid flows play a crucial role for many applications in science and engineering. Indeed, a large variety of natural and industrial processes depend critically on the transport of mass, momentum and energy of chemical species by means of fluid flows across material media of assorted nature [156]. The numerical simulation of such transport phenomena still presents a major challenge to modern computational fluid dynamics. Among the reasons for this complexity stand out the presence of strong heterogeneities and huge scale separation in the basic mechanisms, namely advection, diffusion and chemical reactions [157, 158]. In the last two decades, a novel concept for the solution of transport phenomena in fluid flows has emerged in the form of a minimal lattice Boltzmann (LB) kinetic equation. This approach is based on the statistical viewpoint typical of kinetic theory [159, 160]. LB is currently used across a broad range of problems in fluid dynamics, from fully developed turbulence in complex geometries to micro and nanofluidics [161], all the way down to quark-gluon applications [162].

Recent improvements in ion trap and superconducting circuit experiments make these platforms ideal for challenging quantum information and simulation tasks. On the one hand, trapped-ion experiments have demonstrated quantum information and simulation capabilities [25, 163, 164], including the quantum simulation of highly correlated fermionic systems [60], fermionic-bosonic models [71] and lattice gauge theories [165]. On the other hand, circuit quantum electrodynamics (QED) setups can host nowadays top-end quantum information protocols, such as quantum teleportation [166] and topological phase transitions [167]. These quantum devices are approaching the complexity required to simulate both classical and quantum nontrivial problems, as proposed by Feynman some decades ago [2]. Efforts in designing quantum algorithms for the implementation of fluid dynamics make use of quantum computer networks [168, 169]. In contrast, systems described by pseudospins coupled to bosonic modes, such as the aforementioned ion-trap and circuit QED platforms, have advantages with respect to pure-qubit quantum computers in simulating fluids.

We propose a quantum simulation of lattice Boltzmann dynamics, using coupled pseudospin-boson quantum platforms. Based on previously established analogies between Dirac and LB equations, we define here a full quantum mapping of transport equations in fluid flows. The LB dynamics is simulated sequentially by performing particle streaming and collision steps. The non-unitary collision process can be implemented with an heralded protocol, by sequential collapses of an ancillary qubit. The proposed mapping is amenable to realization in trapped-ion and circuit QED platforms.

9.2 Lattice Boltzmann equation

The lattice Boltzmann equation is a minimally discretized version of the original Boltzmann's kinetic equation, in which the fluid is modeled as an ensemble of particles that move and collide within a uniform lattice. The lattice Boltzmann dynamics is described by the equation

$$(\partial_t + v_i^b \nabla_b) f_i(\vec{x}, t) = -A_{ij}[f_j(\vec{x}, t) - f_j^{eq}(\vec{x}, t)]. \tag{9.1}$$

Here, $f_i(\vec{x}, t)$ is the ith component of the particle fluid density associated with the lattice site $\vec{x}$ at the time t, and with discrete velocity $\vec{v}_i$. The macroscopic fluid density at the site $\vec{x}$ is retrieved as $\rho(\vec{x}, t) = \sum_i f_i(\vec{x}, t)$, while the fluid velocity is defined as

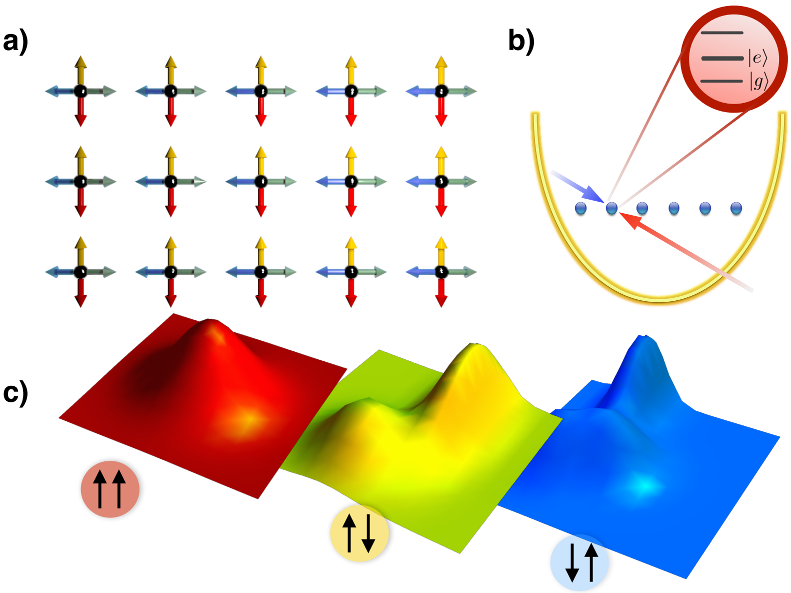

FIGURE 9.1: (a) The distribution of the fluid density on a 2-dimensional lattice can be simulated, for example, via normal motional modes and internal levels of a set of trapped ions (b). (c) Superposition of two motional modes entangled with pseudo spin states can encode velocity distributions in different lattice directions.

the weighted sum of the discrete velocities, $\vec{u}(\vec{x},t) = 1/\rho\sum_i f_i(\vec{x},t)\vec{v}_i$. The velocity components $f_i\vec{v}_i$, with $i = 1, 2, ...Q$, satisfy mass-momentum-energy conservation laws and rotational symmetry. Typical lattices are *D2Q9* or *D3Q15* models, for the case of two dimensions with 9 speeds, and three dimensions with 15 speeds, respectively [170].

Collisional properties are here expressed in scattering-relaxation form, making use of the local equilibrium distribution $f_i^{eq}(\vec{x},t)$. The LB approach to compute the dynamics associated with Eq. (9.1) uses sequential computational steps. One initially performs a displacement (free-streaming) of each distribution component $f_i(\vec{x})$ towards the nearest-neighbor lattice site pointed at by the discrete velocity $\vec{v}_i$. From there, the equilibrium distribution function $f_i^{eq}(\vec{x},t)$ is computed and the outcome of the collisional process is retrieved. Further iterations of these calculations allow the propagation of the lattice dynamics in time. We address the question of whether all these steps can be performed in a quantum simulator with practical quantum computing protocols.

The formal analogy between the Dirac and LB equations was first highlighted in [159, 171], where the velocity distribution of the particle is treated in a similar fashion as a relativistic spinor. This analogy is further exploited in the Majorana representation of the Dirac equation, by using real spinors [172]. The Dirac (Majorana) equation reads ($\hbar = 1$ here and in the following)

$$i(\partial_t + \alpha_{ij}^b \nabla_b)\Psi_i = \beta_{ij}\Psi_i, \tag{9.2}$$

where we have defined the Dirac (Majorana) streaming matrices α_{ij}^{b}, mass term β_{ij}, and the imaginary prefactor i proper of quantum and mechanical evolution.

Notice that the streaming matrices of the LB equation are diagonal, while the α_{ij}, which generate a Clifford algebra, cannot be simultaneously diagonalized. Additionally, the mass matrix β_{ij} is Hermitian, while standard collision matrices come in real symmetric form in the LB equation. Therefore, a complete codification of the LB scheme in quantum language requires the implementation of diagonal streaming matrices and of purely imaginary symmetric scattering matrices.

The components of the fluid density distribution function $f_i(\vec{x}, t)$ can be encoded in a set of quantum states $|\Psi_i\rangle$ defined on a proper Fock space. For example, in two dimensions, the distribution of the fluid density over the two coordinates can be described by a real quantum wavefunction that encodes the state of two bosonic modes, as depicted in Fig. 9.1. In the x-quadrature representation, it reads $|\Psi_i\rangle = \int dx_1 dx_2 f_i(x_1, x_2) |x_1\rangle |x_2\rangle$, where $f_i(x_1, x_2)$ is a real distribution and $|x_{1(2)}\rangle$ the eigenstate of the quadrature of the first (second) bosonic mode. Several quantum distributions $|\Psi_i\rangle$ can be used by entangling the bosonic state to a multi-level system, such as a set of pseudospins, therefore the state of the complete system is given by $|\Psi\rangle = \sum_i \eta_i |i\rangle \otimes |\Psi_i\rangle$. The sole use of dynamics, generated by purely imaginary interaction matrices, guarantees that $|\Psi\rangle$ holds real and it can therefore be identified with a fluid density distribution function.

9.3 Streaming and collision dynamics in a quantum simulator

The quantum simulation of the Dirac equation was originally proposed [19] and afterwards realized in a trapped-ion experiment [20]. In general, streaming interactions involving matrices in the Dirac or Majorana representation $\alpha_{ij}^{b}\nabla_b$ can be implemented by using a pair of pseudospins coupled to one or more bosonic modes. In terms of creation and annihilation operators $a_b(a_b^\dagger)$ for the bth bosonic mode, one can then consider $p_b = i\nabla_b = i(a_b - a_b^\dagger)$ and write Eq. (9.2) on the pseudospin-bosonic Hilbert space of $|\Psi\rangle$,

$$i\partial_t |\Psi(t)\rangle = K_b \alpha^b i(a_b - a_b^\dagger) |\Psi(t)\rangle + \beta |\Psi(t)\rangle , \tag{9.3}$$

where K_b stands for the pseudospin-boson coupling and α^b act upon the pseudospin degrees of freedom.

Thus, the three streaming matrices α_{ij}^{b} are written in the Dirac representation as $\alpha^b = -\sigma_1^x \otimes \sigma_2^b$, in a pseudospin representation and the diagonal mass term as $\beta = \sigma_1^z \mathbb{I}_2$.

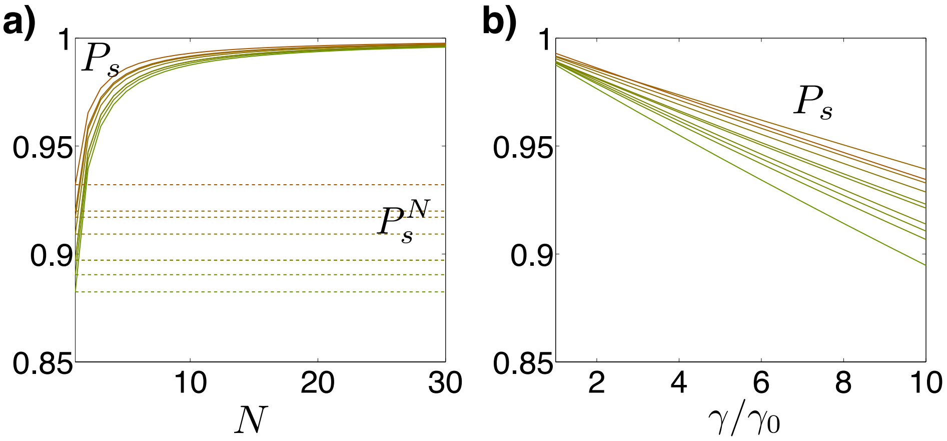

FIGURE 9.2: (a) Probability of success P_s per time step of simulating real symmetric random matrices as a function of the number of ancillary measurements N (solid lines), together with accumulated probabilities for the whole protocol (dashed lines) (b) Probability of succes of a single step as a function of γ/γ_0, when $N = 10$.

These streaming matrices are diagonalized via the operators $S_b = 1/\sqrt{2}(\beta + \alpha^b)$ [172], which have to be physically implemented as quantum gates. Defining $S_b = \exp(-iH_b t)$, the associated generators read $H_b = A\sigma_1^z \otimes \mathbb{I}_2 + B\sigma_1^x \otimes \sigma_2^b$, with $A = \frac{\sqrt{2}\pi}{4}$ and $B = \frac{\pi}{2\sqrt{2}}$. In this way, a purely imaginary streaming step $i\beta\nabla_b$ can be built, which mimics the diagonal streaming of the LB equation. The total wavefunction after the streaming steps can be retrieved with a sequential implementation, following the operator splitting method [171]. For example, in a 2-dimensional lattice, one has

$$|\Psi(t_{n+1})\rangle = (S_y^{-1} D_y S_y)(S_x^{-1} D_x S_x) C\, |\Psi(t_n)\rangle\,. \tag{9.4}$$

The last collision step C, which scrambles particle distributions in different directions, is discussed below.

Standard collision operators in LB theory are represented by real symmetric matrices associated with non-unitary evolution operators. On the other hand, typical controlled quantum mechanics experiments produce unitary dynamics. Nevertheless, one can probabilistically encode non-unitary dynamics in a quantum device with a heralded protocol. We consider a purely imaginary symmetric scattering matrix Ω, whose quantum evolution equation reads $i\partial_t \Psi_i = \Omega_{ij}\Psi_j$, providing a non-unitary evolution operator that describes lattice collisions $C = \exp(-i\Omega\Delta t)$.

The collision operator can be decomposed in a weighted sum of two commuting unitary operators, $C = U_\alpha + \gamma U_\beta$, with the constraint $||C|| \leq 1 + \gamma$, assuming without loss of generality that $\gamma > 0$. Given a specific diagonalizable collision operator C and weight γ, one can then find its decomposition in terms of unitaries. In order to find a decomposition in terms of unitaries, C must first be diagonalized as $C = VDV^\dagger$.

This reduces the problem of finding U_α and U_β down to an eigenvalue equation, $\delta_i = \alpha_i + \gamma\beta_i$, with δ_i, α_i and β_i being the ith eigenvalues of the collision and unitary operators respectively. Notice that, due to the properties of the scattering matrix, $\delta_i \in \mathbb{R}^+$. Taking into account the normalization conditions, one has the system of equations

$$\begin{cases} \delta_i = \alpha_i + \gamma\beta_i \\ |\alpha_i| = 1 \\ |\beta_i| = 1. \end{cases} \tag{9.5}$$

The eigenvalues α_i, β_i can now be written as a function of the initial collision operator and weight γ,

$$\begin{aligned} \mathrm{Re}(\alpha_i) &= \frac{\delta_i^2 - \gamma^2 + 1}{2\delta_i} \\ \mathrm{Im}(\alpha_i) &= \frac{\sqrt{-\delta_i^4 + 2\delta_i^2\left(\gamma^2+1\right) - \left(\gamma^2-1\right)^2}}{2\delta_i} \\ \mathrm{Re}(\beta_i) &= \frac{\delta_i^2 + \gamma^2 - 1}{2\delta_i\gamma} \\ \mathrm{Im}(\beta_i) &= -\frac{\sqrt{-\delta_i^4 + 2\delta_i^2\left(\gamma^2+1\right) - \left(\gamma^2-1\right)^2}}{2\delta_i\gamma}. \end{aligned} \tag{9.6}$$

The unitary operators $U_{\alpha(\beta)}$ are reconstructed via $\left(U_{\alpha(\beta)}\right)_{ij} = V^\dagger_{in}\alpha_n(\beta_n)V_{nj}$. The real domain of Eqs. (9.6) provides the range of validity of the method developed here. Simple algebra leads to the set of inequalities

$$|-1+\delta_i| \leq \gamma \leq 1+\delta_i, \quad \forall i. \tag{9.7}$$

By defining δ_M and δ_m as the maximal and minimal eigenvalues of the spectrum of C, the system of inequalities in Eq. (9.7) can be reduced to one of the two inequalities $|-1+\delta_m| \leq \gamma \leq 1+\delta_m$ or $|-1+\delta_M| \leq \gamma \leq 1+\delta_m$, respectively when $|-1+\delta_m| \leq |-1+\delta_M|$ or $|-1+\delta_m| \geq |-1+\delta_M|$. If longer evolution times t are considered, the spectral range of C changes accordingly. The weighted γ-sum derived here can be implemented with quantum computing algorithms, using ancillary qubits and controlled U_α and U_β gates [173]. By measuring the ancilla state, one can determine whether the desired operation has been performed or not. The success of the protocol depends on the weighted sum of unitary operators, with a failure probability $P_f = \gamma||U_\alpha - U_\beta||^2/(\gamma+1)^2$.

As P_f is an increasing function of γ, choosing $\gamma_0 = \min\{|-1+\delta_m|, |-1+\delta_M|\}$ maximizes the probability of success. This directly connects the simulation time of the scattering process C with the best choice for γ. To propagate the dynamics of a given collision process C, one can split the step time Δt into N time intervals $\Delta t/N$ and perform the heralded protocol at each step, such that $C = \exp(-i\Omega_{ij}\Delta t/N)^N$. At each step, one has a collision operator $\exp(-i\Omega_{ij}\Delta t/N)$, with an optimal γ_0. In this way, as the step size gets smaller, the success probabilities for each step increase, while the total success probability accumulates single success rates from the individual steps. In Fig. 9.2a, we plot the success probability $P_s(N) = 1 - P_f(N)$ of the simulation of the single step, as a function of N, for random symmetric purely imaginary matrices. As expected, the success probability per step increases as the size for the single time step gets smaller. The success of the whole protocol P_s^N is constant and does not depend on N. In Fig. 9.2b is shown that the optimal protocol is performed at $\gamma = \gamma_0$.

9.4 Four-speed lattice

The scheme proposed can be adapted to a variety of transport fluid problems. As an example, we consider the implementation of an advection-diffusion process in two spatial dimensions. The dynamics of the transported species, e.g. pollutants or bacteria, is described by the equation

$$\partial_t \rho + \nabla \cdot (\rho \vec{U}) = D\Delta\rho, \tag{9.8}$$

where $\rho = \sum_{i=1}^{4} f_i$ is the scalar field transported by a fluid with space-dependent velocity $\vec{U} = (U_x, U_y)$ and constant diffusivity D.

The problem in Eq. (9.8) can be recast in LB form, as in Eq. (9.1). The corresponding equilibrium distribution function is defined as

$$f_i^{eq} = w_i \left[\rho + \frac{\rho \vec{U} \cdot \vec{c}_i}{c_s^2} \right], \tag{9.9}$$

with $w_i = 1/4$, $c_s^2 = 1/2$. The scattering matrix reads $A_{ij} = \sum_{k=1}^{4} A_i^{(k)} \omega_k A_j^{(k)}$, where $A_i^{(1)} = 1_i \equiv (1,1,1,1)$, $A_i^{(2)} = c_{ix} \equiv (1,0,-1,0)$, $A_i^{(3)} = c_{iy} \equiv (0,1,0,-1)$ and $A_i^{(4)} = c_{ix}^2 - c_s^2 \equiv (1/2, 0, 1/2, 0)$ are the four eigenvectors.

The first three corresponding eigenvalues are given by

$$\omega_1 = 0, \quad \omega_2 = \omega_3 = \frac{1}{1/2 + D/c_s^2}, \tag{9.10}$$

which follows from mass conservation and the expression of the diffusion constant $D = c_s^2(1/\omega - 1/2)$, respectively. By choosing different values for ω_2 and ω_3, one can implement anisotropic diffusivities along the x and y directions. Finally, ω_4 has no direct bearing on the macroscopic limit and can be chosen as $\omega_4 = 1$ for convenience. The relative scattering matrix Ω_{ij} is defined by $-A_{ij}[f_j(\vec{x};t) - f_j^{eq}(\vec{x};t)] = \Omega_{ij} f_j(\vec{x}, t)$. By choosing

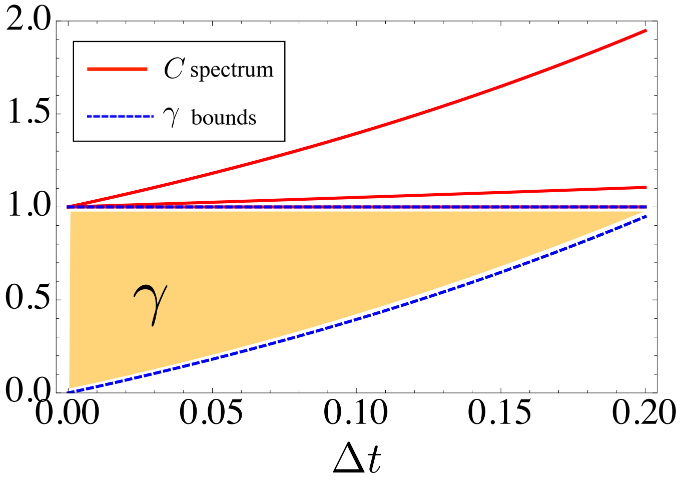

FIGURE 9.3: Spectrum of a collision operator (solid red line) for advection-diffusion process of a four-speed lattice as a function of the evolution time step Δt, in units of $1/\omega_4$. The allowed region for γ is bounded by dashed blue lines using Eq. (9.7) and shadowed in the picture.

a Couette flow, e.g. $U = U_0/L(y, 0)$, where L is the typical size of the domain, one has $f_i^{eq} = w_i\rho(1 + u_i)$, with $u_1 = -u_3 = U_0 y/c_s^2$ and $u_2 = u_4 = 0$. Here, velocities are numbered $1 \div 4$ counterclockwise starting from the $+x$ direction.

The latter defines the quantum scattering matrix as composed of three contributions, namely $i\Omega_{ij} f_j = -iA_{ij}[f_j + w_j\rho + w_j\rho u_j]$, where $y \equiv a_2 + a_2^\dagger$ stands for the position quadrature of the bosonic mode associated with the y direction. The three contributions to the scattering matrix represent classical linear wave propagation and damping, mass conservation and macroscopic advection, respectively. They can be implemented with the quantum simulation protocol previously introduced. The bounds to γ can be obtained, e.g., for the first contribution to the scattering matrix $-A_{ij}$, by computing the spectrum of $C = e^{-A\Delta t}$ for different time steps Δt, for $D = 0.05$, in units of $1/\omega_4$. The result is shown in Fig. 9.3.

Natural quantum platforms for prospective implementation of the proposed scheme could be ions trapped in linear Paul traps or circuit QED setups, in which the sequential streaming and collision steps in Eq. (9.4) can be realized. The pseudospin-bosonic state can be encoded, in the case of ion traps, in the internal level and motion modes of the ions [14], while in a circuit QED implementation, one can use the first levels of charge-like qubits, e.g. transmon qubits, and microwave resonators [34]. One may consider opening similar avenues in other quantum technologies as is the case of quantum photonics [174] and Bose-Einstein condensates [175].

Note that the above scheme readily extends to the case of reactive flow, by augmenting the collision operator with a local source term proportional to the chemical reaction rate. Such kind of advection-diffusion-reaction phenomena in complex geometries, say catalytic reactors, represents a very active area of applications of the LB scheme. Further developments may include the implementation of hydrodynamic non-linearities to model the Navier-Stokes fluid dynamic equations. This requires the inclusion of quadratic terms in the LB equilibrium distribution. Such nonlinear behavior can be provided in a quantum mechanical experiment by preparing multiple copies of the system [176], feedback mechanisms [177], or non-unitary operations induced by measurements.

We have developed a protocol to reproduce the dynamics of fluid transport phenomena in a quantum mechanical experiment, by using pseudospins coupled to bosonic modes that can be implemented in different quantum platforms. This proposal paves the way to quantum simulation and retrieval of complex classical fluid dynamics in controlled quantum systems.

Part IV

Conclusions

Conclusions

In this Thesis, we have proposed a variety of quantum information protocols, analyzing their implementation with quantum platforms, mainly trapped-ion and superconducting circuit architectures. We believe that the results here obtained will serve to strengthen the connection between theoretical and experimental physics oriented to quantum information, when it comes to practical implementations. The work done here will hopefully contribute, in the near future, to bring new knowledge in the fields of condensed matter, high-energy physics, quantum chemistry and classical fluid dynamics, as the available quantum platforms scale up in terms of size and control.

In Chapter 2, we have shown that trapped-ion chains can host a parity-based protected qubit [44], based on a dual representation of a topological fermionic Kitaev chain. We have predicted that this qubit can outperform the usual ionic qubit coherence time by more than one order of magnitude, yielding an efficient quantum memory. Logical local rotations upon the qubit can be performed by means of global and local laser-ion interactions. Moreover, a quantum interface with photonic states can be realized, allowing for the realization of two-qubit gates among several of such parity qubits. These parity qubits represent a practical instance, realizable with minimal quantum resources, of a logical qubit.

In Chapter 3, 4 and 5, we have developed a framework for the digital quantum simulation of fermionic and coupled fermionic-bosonic dynamics in trapped-ion systems. This framework has been first applied to the simulation of fermionic models [60]. We have proposed that collective interactions between a set of many ions can implement high-order and long range fermionic interactions. These collective gates also account for increased efficiency in the simulation of two and three-dimensional fermionic systems, when compared to simulation protocols based on local two-qubit gates. The total dynamics of the fermionic model is then recovered by means of a digitization and Jordan-Wigner mapping. With current ion-trap technology, more than 100 gates have been realized in a single experiment [25]. Indeed, without error correction, one would expect the realization of hundreds of gates in times shorter than the decoherence time of 30 ms. The rate at which ion-trap systems actually improve [4], combined with the increased efficiency of our proposal, make these results look relevant, e.g., for quantum simulations of condensed-matter systems, or for probing high-energy physics in nonperturbative regimes.

In Chapter 4, we have extended the simulation protocol presented in Chapter 3 to coupled bosonic-fermionic systems, explaining in detail how it can be realized for the Holstein model [71]. The simulation of these systems has an increased complexity with respect to purely fermionic systems, due to the fast-growing Hilbert space, following the growth of the bosonic population. It is noteworthy to mention that our proposed digital quantum simulation will already overcome the limits of classical computers with 10 ions and 5 phonons per ion. This will allow to study the formation of small polarons under these conditions. Future experiments involving 20 to 30 ions will permit to address the study of more complex dynamics, including electron-electron correlations mediated by phonons. In Chapter 5, using the framework developed for the fermionic systems, we have proposed a hybrid quantum simulation protocol for quantum chemistry with trapped ions [178]. This paradigm in quantum simulations has several advantages: an efficient electronic simulation, the possibility of interacting electronic and vibrational degrees of freedom, and the increasing scalability provided by trapped-ion systems. This approach for solving quantum chemistry problems aims to combine the best of classical and quantum computation, for the sake of computational efficiency.

In Chapters 6, 7 and 8, we have dealt with superconducting circuit systems. In Chapter 6, we have proposed a digital quantum simulation of spin chain models in superconducting circuits [130]. We have considered prototypical models as the Heisenberg and frustrated Ising interactions. Furthermore, we have shown the feasibility of the simulation with state-of-the-art technology of transmon qubits coupled to microwave resonators. The proposed models have been realized by the Quantum Device Lab of Prof. Andreas Wallraff at ETH Zürich. These protocols may be extended to many-qubit spin models, paving the way towards universal quantum simulation of spin dynamics in cQED setups. In Chapter 7, we have shown that a setup made out of several superconducting three-island devices, provided with tunable coupling to a coplanar waveguide resonator, can realize collective gates and many-body interactions among superconducting qubits [179]. These interactions, similar to the ones analyzed in Chapter 3 for ion-trap systems, can be used to implement topological codes and efficiently simulate fermionic dynamics in cQED setups. Finally, in Chapter 8, we have shown that the dynamics of the quantum Rabi and Dicke models can be encoded in a cQED setup using an digital-analog approach [131]. These quantum simulations will contribute to the observation of quantum dynamics not accessible in current experiments.

In the last part of this Thesis we have analyzed quantum simulations for classical systems. In Chapter 9, we have developed a protocol to reproduce the dynamics of fluid transport phenomena in a quantum mechanical experiment, by using pseudospins coupled to bosonic modes that can be implemented in different quantum platforms [180]. This proposal paves the way to quantum simulation and retrieval of complex classical fluid dynamics in controlled quantum systems. Further developments to this work will include the possibility of simulating nonlinear behavior, and extending the proposal to more complex fluid dynamics models.

In the Appendix, we present complementary material to the Parts and Chapters, which helps for a better understanding of the results shown in this Thesis.

We believe that the scientific results presented in this Thesis represent an important contribution to the success and development of quantum technology in the near future.

Part V

Appendices

Appendix A

An upper bound for the norm of the Holstein Hamiltonian

In this Appendix, we give an upper bound for the the norm of the Holstein Hamiltonian in Chapter 4, in order to bound the error one makes with a Suzuki-Lie-Trotter expansion [40]. Consequently, we bound the number of gates one needs for achieving a given fidelity on the simulated quantum state. The norm is bounded by the sum of the norms of each term appearing in H. The computation of single norms amounts to finding the largest eigenvalue of the single terms

$$\begin{aligned} ||H|| \leq |h| \cdot \sum_{i=1}^{N-1} \left\|(\sigma_i^+\sigma_{i+1}^- + h.c.)\right\| + \\ +|g| \sum_{i=1}^{N} \left\|(b_i + b_i^\dagger)\frac{(\sigma_i^z + 1)}{2}\right\| + \omega_0 \sum_{i=1}^{N} \left\|b_i^\dagger b_i\right\| . \end{aligned} \tag{A.1}$$

The term expressed by $|h| \sum_{i=1}^{N-1} \left\|(-\sigma_i^+\sigma_{i+1}^- + h.c.)\right\| = |h/2| \sum_{i=1}^{N-1} \left\|(\sigma_i^x\sigma_{i+1}^x + \sigma_i^y\sigma_{i+1}^y)\right\|$ represents a sum of $2(N-1)$ tensor products of Pauli matrices, with norm 1. Therefore, $|h| \sum_{i=1}^{N-1} \left\|(-\sigma_i^+\sigma_{i+1}^- + h.c.)\right\| \leq |h|(N-1)$. The norm $\left\|b_i^\dagger b_i\right\|$ is bounded by the truncation in the number of bosons in the mode i , as is clear by the standard Fock representation

$$b_i^\dagger b_i \rightarrow \begin{pmatrix} 0 & & & \\ & 1 & & \\ & & \ddots & \\ & & & M \end{pmatrix}, \quad \left\|b_i^\dagger b_i\right\| = M. \tag{A.2}$$

Therefore $\sum_{i=1}^{N} \left\|b_i^\dagger b_i\right\| = \sum_{i=1}^{N} M = NM$.

The norm $\sum_{i=1}^{N}\left\|(b_i+b_i^\dagger)\frac{(\sigma_i^z+1)}{2}\right\|$ is equivalent to $\sum_{i=1}^{N}\left\|(b_i+b_i^\dagger)\right\|$, given that $\left\|\frac{(\sigma_i^z+1)}{2}\right\| = 1$. The term $(b_i+b_i^\dagger)$ in the Fock basis reads

$$(b_i+b_i^\dagger) \rightarrow \begin{pmatrix} 0 & 1 & & & & \\ 1 & 0 & \sqrt{2} & & & \\ & \sqrt{2} & 0 & & & \\ & & & \ddots & & \\ & & & & 0 & \sqrt{M} \\ & & & & \sqrt{M} & 0 \end{pmatrix}. \tag{A.3}$$

The characteristic polynomial of the matrix for the truncation to M bosons is given in a recursively way,

$$\begin{aligned} D_0(\lambda) = 1,\ D_1(\lambda) = -\lambda \\ D_n(\lambda) = -\lambda D_{n-1}(\lambda) - (n-1)D_{n-2}(\lambda). \end{aligned} \tag{A.4}$$

The $D_n(\lambda)$ are a $\sqrt{2}$ rescaled version of the Hermite polynomials. A simple bound for the largest zero of $D_M(\lambda)$ (i.e. the norm of the bosonic displacement operator) is given by the expression $2\sqrt{M-1}$ (see for example Ref. [181]). Summarizing, the norm for the Holstein Hamiltonian is upper bounded by

$$\|H\| \leq |h|(N-1) + 2|g|N\sqrt{M-1} + \omega_0 NM. \tag{A.5}$$

Appendix B

Estimation of non-nearest-neighbor coupling strenght

In this Appendix, we give an estimation of the NNN couplings that appear when one wants to generate the NN Ising interaction with the parameters that we use in Chapter 4. We propose to address pairs of NN ions with independent counterpropagating couples of lasers detuned close to different modes, i.e. a different mode is assigned to a specifiic couple of NN ions. This gives rise to NNN coupling between distant ions, which we show being negligible for specific detunings and gate times. For a 3+1 ion configuration, for example, the total Hamiltonian is

$$H = H_1 + H_2 = \sum_m \sin(\delta_1 t) \left(a_m e^{-i\nu_m t} + a_m^\dagger e^{i\nu_m t} \right) \sum_{i=1}^{2} \Omega_i \eta_{i,m} \sigma_i^x + \tag{B.1}$$
$$\sum_m \sin(\delta_2 t) \left(a_m e^{-i\nu_m t} + a_m^\dagger e^{i\nu_m t} \right) \sum_{i=2}^{3} \Omega_i \eta_{i,m} \sigma_i^x ,$$

obtained by driving the first two ions with two pairs of counterpropagating lasers detuned to $\pm\delta_1$ [65], while the lasers driving the second and the third ion are detuned to $\pm\delta_2$. Therefore a second order Magnus expansion of the Hamiltonian in Eq.(B.1) leads to unwanted NNN terms in the evolution operator of the form

$$\left(\int_0^t dt' \int_0^{t'} dt'' [H_1(t'), H_2(t'')] \; + \int_0^t dt' \int_0^{t'} dt'' [H_2(t'), H_1(t'')] \right) = \tag{B.2}$$
$$\sum_m \left(Z_{1,m}(t) + Z_{2,m}(t) \right) S_{1,m} S_{2,m}, \tag{B.3}$$

where we have defined $S_{1,m} = \sum_{i=1}^{2} \Omega_i \eta_{i,m} \sigma_i^x$, $S_{2,m} = \sum_{i=2}^{3} \Omega_i \eta_{i,m} \sigma_i^x$. Some straightforward algebra leads to

$$Z_{1,m}(t) = \frac{i}{2(\delta_1^2 - \nu_m^2)} \Big(\delta_1 \frac{\sin(\delta_2 - \nu_m)t}{(\delta_2 - \nu_m)} - \delta_1 \frac{\sin(\delta_2 + \nu_m)t}{(\delta_2 + \nu_m)} + \tag{B.4}$$

$$\nu_m \frac{\sin(\delta_2 - \delta_1)t}{(\delta_2 - \delta_1)} - \nu_m \frac{\sin(\delta_2 + \delta_1)t}{(\delta_2 + \delta_1)} \Big), \tag{B.5}$$

$$Z_{2,m}(t) = \frac{i}{2(\delta_2^2 - \nu_m^2)} \Big(\delta_2 \frac{\sin(\delta_1 - \nu_m)t}{(\delta_1 - \nu_m)} - \delta_2 \frac{\sin(\delta_1 + \nu_m)t}{(\delta_1 + \nu_m)} + \tag{B.6}$$

$$\nu_m \frac{\sin(\delta_1 - \delta_2)t}{(\delta_1 - \delta_2)} - \nu_m \frac{\sin(\delta_1 + \delta_2)t}{(\delta_1 + \delta_2)} \Big). \tag{B.7}$$

These contributions are negligible for the parameters that we use, i.e. first detuning close to the first mode and second detuning close to the second one, $|\nu_1 - \delta_1| \ll \nu_1$, $|\nu_2 - \delta_2| \ll \nu_2$. For example, taking the strongest resonant term from the series in Eq. (B.2), $m = 2$ for $Z_{2,2}(t)$, the first term on the right side in Eq. (B.6) reads

$$\frac{\delta_2 \sin(\delta_1 - \nu_2)t}{2(\delta_2^2 - \nu_2^2)(\delta_1 - \nu_2)} = \frac{\delta_2 \sin(\delta_1 - \nu_2)t}{2(\delta_2 + \nu_2)(\delta_2 - \nu_2)(\delta_1 - \nu_2)}. \tag{B.8}$$

Since $\Omega_i \eta_{i,m} \cong \Omega_j \eta_{j,n}$, the term is negligible in comparison to the desired NN terms, whose couplings goes like $-\frac{i\nu_2 t}{2(\delta_2^2 - \nu_2^2)}$, $-\frac{i\nu_1 t}{2(\delta_1^2 - \nu_1^2)}$, for sufficient large times,

$$\left| \frac{\nu_2 t}{(\delta_2 + \nu_2)(\delta_2 - \nu_2)} \right| \gg \left| \frac{\delta_2}{(\delta_2 - \nu_2)(\delta_2 + \nu_2)(\delta_1 - \nu_2)} \right|, \tag{B.9}$$

$$t \gg \left| \frac{\delta_2}{\nu_2} \frac{1}{(\delta_1 - \nu_2)} \right|. \tag{B.10}$$

For realistic parameters the critical time is $t \sim 1/\nu_1$. Since our gates are obtained at times $\tau \sim 100/\nu_1$, these NNN terms can be neglected. We stress again that in the protocol some of the frequencies ν_i have to be shifted, we have left the original frequencies to avoid a heavy notation. Same kind of considerations are valid for the other terms in the right side of Eq. (B.6) and Eq. (B.4). This also extends in a straightforward way to couplings between any two NNN ions in a configuration with an arbitrary number of ions, as long as conditions like Eq. (B.10) are satisfied.

Appendix C

Derivation of effective models for collective gates

In this Appendix, we show in detail how to derive the effective collective entangling Hamiltonian between N tunable-coupling transmon qubits (TCQs) presented in Chapter 7. We start from the interaction between the resonator and several TCQs capacitively coupled to it,

$$\tilde{H}_I = \sum_{j=1}^{N} \sum_{\pm} g_{\pm}(t)(\tilde{b}^{\dagger}_{\pm j} - \tilde{b}_{\pm j})(a^{\dagger} - a). \tag{C.1}$$

According to what is discussed in Chapter 7, one can design proper magnetic fluxes, threading the SQUIDs in each TCQ, in order to modulate $g_+(t) = g^s_+ + g^d_+[\cos(\omega_g t) + \cos(\omega'_g t)]$, where one has defined the two detuned sideband frequencies $\omega_g = \omega_r + \tilde{\omega}_+ - \delta$ and $\omega'_g = \omega_r - \tilde{\omega}_+ - \delta$. As a consequence, also the transition element to the third level of the devices $g_-(t)$ will undergo fast oscillations. One can numerically obtain its time dependence, and expand the signal in its Fourier components $g_-(t) = \sum_n g_n \exp(i\omega_n t)$, with $\omega_n = 2\pi n/T$, where $n \in \mathbb{Z}$, and T is much larger than the timescale of the dynamics considered. The interaction Hamiltonian in a many qubit setup then becomes

$$\begin{aligned}\tilde{H}_I = \quad & \sum_{j=1}^{N} \left[g^s_+ + g^d_+ \left(\cos(\omega_g t) + \cos(\omega'_g t)\right)\right] (\tilde{b}^{\dagger}_{+j} - \tilde{b}_{+j})(a - a^{\dagger}) \\ & + \sum_{j=1}^{N} \left[\sum_n g_n \exp(i\omega_n t)\right] (\tilde{b}^{\dagger}_{-j} - \tilde{b}_{-j})(a - a^{\dagger}).\end{aligned} \tag{C.2}$$

One can identify three contributions to the dynamics, $\tilde{H}_I = \tilde{H}_{I_{\mathrm{JC}}} + \tilde{H}_{I_+} + \tilde{H}_{I_-}$. There are two terms representing standard Jaynes-Cummings interactions, due to the static contributions of the couplings,

$$\tilde{H}_{I_{\rm JC}} = -\sum_{j=1}^{N}\sum_{\pm} g^s_{\pm}(\tilde{b}^\dagger_{\pm j}a + \tilde{b}_{\pm j}a^\dagger), \tag{C.3}$$

where we have defined $g^s_- \equiv g_0$. The other contributions to the dynamics are given by the time-dependent part of the interaction. Namely,

$$\begin{aligned}\tilde{H}_{I_+} &= \sum_{j=1}^{N} g^d_+\left[\cos(\omega_g t) + \cos(\omega'_g t)\right](\tilde{b}^\dagger_{+j} - \tilde{b}_{+j})(a - a^\dagger),\\ \tilde{H}_{I_-} &= \sum_{j=1}^{N}\left[{\sum_n}' g_n \exp(i\omega_n t)\right](\tilde{b}^\dagger_{-j} - \tilde{b}_{-j})(a - a^\dagger),\end{aligned} \tag{C.4}$$

where the prime symbol excludes the zeroth addend from the series. One can define an interaction picture with respect to $\tilde{H}_0$, and neglect the $\tilde{H}_{I_-}$ contribution, if there is no large component g_n of the Fourier decomposition, whose frequency ω_n is close to the resonator-third level sidebands. This is shown to be the case in Fig. 3 in Chapter 7. Due to sufficient level anharmonicity, that one can assume being preserved during the dynamics, only the two lowest levels for each anharmonic oscillator are populated. One is thus allowed to consider a two-level Pauli algebra to model qubit excitations, $\tilde{b}_{\pm j} \equiv \sigma^-_{\pm j}$(equivalently $\tilde{b}^\dagger_{\pm j} \equiv \sigma^+_{\pm j}$), and the interaction Hamiltonian, in the rotated frame, becomes

$$\tilde{H}_I \approx \sum_{j=1}^{N}\left[g^s_+ + g^d_+\left(\cos(\omega_g t) + \cos(\omega'_g t)\right)\right](\sigma^+_{+j}e^{i\tilde{\omega}_+ t} - \sigma^-_{+j}e^{-i\tilde{\omega}_+ t})(ae^{-i\omega_r t} - a^\dagger e^{i\omega_r t}). \tag{C.5}$$

Under the condition $|(g^s_+)^2/\Delta_+| \ll |(g^d_+)^2/4\delta|$, the biggest contribution to the dynamics come from the terms rotating at the smallest frequency δ,

$$\tilde{H}_I = \sum_{j=1}^{N}\frac{g^d_+}{2}\left\{(\sigma^+_{+j} - \sigma^-_{+j})(a^\dagger e^{i\delta t} - ae^{-i\delta t})\right\} = -i\frac{g^d_+}{2}S^y(a^\dagger e^{i\delta t} - ae^{-i\delta t}), \tag{C.6}$$

where $S^y = \sum_{j=1}^{N}\sigma^y_{+j}$. The evolution operator associated with Hamiltonian in Eq. (C.6) can be computed exactly at second order in $g^d_+/2$, obtaining

$$\tilde{U}_I(t) = \exp\left\{\frac{g^d_+ S^y}{2\delta}\left[(e^{i\delta t} - 1)a^\dagger - {\rm H.c.}\right]\right\}\exp\left\{i\left(\frac{g^d_+}{2\delta}S^y\right)^2\left[\sin(\delta t) - \delta t\right]\right\}. \tag{C.7}$$

At times $\tau = 2\pi n/\delta$, with integer n, the above evolution operator can be associated with the effective unitary $\tilde{U}_I(t) = \exp\left[i\sum_{ij}(g^d_+)^2/4\delta\sigma^y_{+i}\sigma^y_{+j}\right]$. By choosing appropriate initial phases in Eq. (C.1), one can obtain the generic effective interaction (here $\alpha = \{x, y\}$)

$$H_{I_{\text{eff}}} = -\sum_{ij} \frac{(g_+^d)^2}{4\delta} \sigma_{+i}^{\alpha} \sigma_{+j}^{\alpha}. \tag{C.8}$$

Appendix D

Many-body operators

In this Appendix, we show explicitly how to obtain an effective many-body interaction of N qubits, along the lines of Refs. [56, 70]. We consider a combination of direct and inverse collective gates and a local rotation on one of the qubits (e.g. the first one). In other words, we consider the gate sequence $U_{\rm S}(t) = \exp(-iH_{I_{\rm eff}}\tau)\exp(igt\sigma_1^z)\exp(iH_{I_{\rm eff}}\tau)$, where $\tau = \phi 2\delta/(g_+^d)^2$, that explicitly reads

$$U_{\rm S}(t,\phi) = e^{i\phi/2\sum_{j=2}\sigma_i^\alpha\sigma_j^\alpha}e^{igt\sigma_1^z}e^{-i\phi/2\sum_{j=2}\sigma_i^\alpha\sigma_j^\alpha}. \tag{D.1}$$

One can expand the local rotation and write the equivalent expression

$$U_{\rm S}(t,\phi) = e^{i\phi/2\sigma_1^\alpha\sum_{j=2}\sigma_j^\alpha}\left(\cos(gt) + i\sin(gt)\sigma_1^z\right)e^{-i\phi/2\sigma_1^\alpha\sum_{j=2}\sigma_j^\alpha}. \tag{D.2}$$

Taking into account that $\sigma_1^z e^{i\phi/2\sigma_1^\alpha\sum_{j=2}\sigma_j^\alpha} = e^{-i\phi/2\sigma_1^\alpha\sum_{j=2}\sigma_j^\alpha}\sigma_1^z$, one has that

$$U_{\rm S}(t,\phi) = \cos(gt) + i\sin(gt)\sigma_1^z e^{-i\phi\sigma_1^\alpha\sum_{j=2}\sigma_j^\alpha}. \tag{D.3}$$

Considering that $\left(\sigma_1^z e^{-i\phi/2\sigma_1^\alpha\sum_{j=2}\sigma_j^\alpha}\right)^n = \{1, \sigma_1^z e^{-i\phi/2\sigma_1^\alpha\sum_{j=2}\sigma_j^\alpha}\}$ for $n = \{\text{even,odd}\}$, Eq. (D.3) can be rewritten,

$$U_S(t,\phi) = \exp\left(igt\sigma_1^z\prod_{j=2}\left(\cos(\phi) - i\sigma_1^\alpha\sigma_j^\alpha\sin(\phi)\right)\right). \tag{D.4}$$

Choosing $\phi = \pi/2$, one has

$$U_{\rm S}(t,\pi/2) = \exp\left(igt\sigma_1^z\prod_{j=2}\left(-i\sigma_1^\alpha\sigma_j^\alpha\right)\right). \tag{D.5}$$

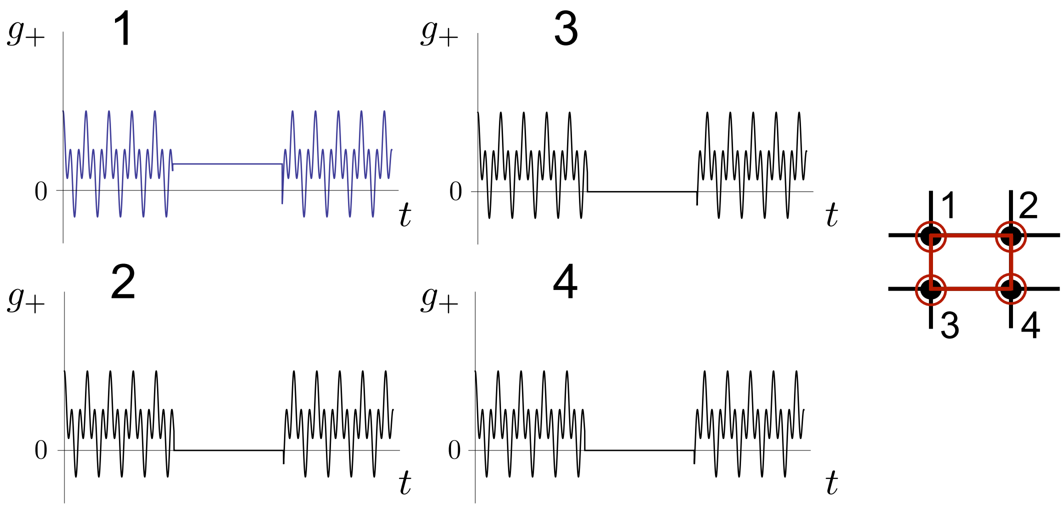

FIGURE D.1: a) Scheme of the generation of many-particle operator among four TCQs. The coupling of the four qubits to the resonator is shown as a function of time. Collective gates as in Eq. (C.8) are performed in the initial and final time regions, while a standard phase gate is performed upon the first qubit between the two collective operations. The effective interaction can be mapped on an arbitrary stabilizer operator on a spin lattice with generic topology, due to the non-local nature of the quantum bus. With an additional ancillary qubit, the system state can be mapped on the ground states of topological codes, via stabilizer pumping.

The resulting gate, as a function of the total number of qubits N, reads

$$\begin{aligned} &\exp\left(-igt\sigma_1^z\sigma_2^\alpha\cdots\sigma_N^\alpha\right), N=4n-1, \\ &\exp\left(igt\sigma_1^z\sigma_1^\alpha\cdots\sigma_N^\alpha\right), N=4n+1, \\ &\exp\left(igt\sigma_1^\beta\sigma_2^\alpha\cdots\sigma_N^\alpha\right), N=4n, \\ &\exp\left(-igt\sigma_1^\beta\sigma_2^\alpha\cdots\sigma_N^\alpha\right), N=4n-2, \end{aligned} \tag{D.6}$$

where $\sigma_1^\beta=-\sigma_1^y(\sigma_1^x)$ for $\alpha=x(y), N=4n$, and $\sigma_1^\beta=\sigma_1^y(-\sigma_1^x)$ for $\alpha=x(y), N=4n-2$. All these interactions are equivalent to an arbitrary stabilizer many-body operator, up to local rotations. Summarizing, the physical realization of the multiqubit interaction can be schematized as in Fig. D.1. Magnetic fluxes drive the collective gates at the beginning and the end of the protocol, while in the central time interval the coupling with the resonator of all the qubits is turned off, except for the TCQ that undergoes a standard phase shift gate (qubit 1 in the figure). By adding an auxiliary ancilla qubit one can guide the ground state of the system to the one of topological states [140], via the stabilizer pumping protocol described in [56]. Sequences of collective operators as in Eq. (D.6) can be used to simulate correlated fermionic Hamiltonians in spin systems, with a constant overhead of the quantum resources, according to the protocols presented in [60, 71].

Bibliography

[1] R. P. Feynman, Caltech Engineering and Science **23:5**, 22 (1960).

[2] R. P. Feynman, Int. J. Theor. Phys. **21**, 467 (1982).

[3] R. P. Feynman, Optics News **11**, 11 (1982).

[4] R. Blatt and C. F. Roos, Nature Phys. **8**, 277 (2012).

[5] I. Bloch, J. Dalibard, and S. Nascimbène, Nat. Phys. **8**, 267 (2012).

[6] A. Aspuru-Guzik and P. Walther, Nat. Phys. **8**, 285 (2012).

[7] A. A. Houck, H. E. Türeci, and J. Koch, Nat. Phys. **8**, 292 (2012).

[8] D. Leibfried, R. Blatt, C. Monroe, and D. J. Wineland, Rev. Mod. Phys. **75**, 281 (2003).

[9] W. Nagourney, J. Sandberg, and H. Dehmelt, Phys. Rev. Lett. **56**, 2797 (1986).

[10] F. Diedrich, J. C. Bergquist, W. M. Itano, and D. J. Wineland, Phys. Rev. Lett. **62**, 403 (1989).

[11] C. Monroe, D. M. Meekhof, B. E. King, S. R. Jefferts, W. M. Itano, and D. J. Wineland, Phys. Rev. Lett. **75**, 4011 (1995).

[12] J. I. Cirac and P. Zoller, Phys. Rev. Lett. **74**, 20 (1995).

[13] K. Mølmer and A. Sørensen, Phys. Rev. Lett. **82**, 9 (1999).

[14] H. Häffner, C. F. Roos, and R. Blatt, Physics Reports **469**, 155 (2008).

[15] P. Schindler, D. Nigg, T. Monz, J. T. Barreiro, E. Martinez, S. X. Wang, S. Quint, M. F. Brandl, V. Nebendahl, C. F. Roos, et al., New. J. Phys. **15**, 123012 (2013).

[16] K. Kim, M.-S. Chang, S. Korenblit, R. Islam, E. E. Edwards, J. K. Freericks, G. D. Lin, L. M. Duan, and C. Monroe, Nature **456**, 590 (2010).

[17] J. W. Britton, B. C. Sawyer, A. C. Keith, C.-C. J. Wang, J. K. Freericks, H. Uys, M. J. Biercuk, and J. J. Bollinger, Nature **463**, 68 (2010).

[18] F. Barahona, Journal of Physics A: Mathematical and General **15**, 3241 (1982).

[19] L. Lamata, J. León, T. Schätz, and E. Solano, Phys. Rev. Lett. **98**, 253005 (2007).

[20] R. Gerritsma, G. Kirchmair, F. Zähringer, E. Solano, R. Blatt, and C. F. Roos, Nature **463**, 68 (2010).

[21] L. Lamata, J. Casanova, R. Gerritsma, C. F. Roos, J. J. García-Ripoll, and E. Solano, New. J. Phys. **13**, 095003 (2011).

[22] J. Casanova, J. J. García-Ripoll, R. Gerritsma, C. F. Roos, and E. Solano, Phys. Rev. A **82**, 020101(R) (2010).

[23] R. Gerritsma, B. P. Lanyon, G. Kirchmair, F. Zähringer, C. Hempel, J. Casanova, J. J. García-Ripoll, E. Solano, R. Blatt, and C. Roos, Phys. Rev. Lett. **106**, 060503 (2011).

[24] S. Lloyd, Science **2073**, 1073 (1996).

[25] B. P. Lanyon, C. Hempel, D. Nigg, M. Müller, R. Gerritsma, F. Zähringer, P. Schindler, J. T. Barreiro, M. Rambach, G. Kirchmair, M. Hennrich, P. Zoller, R. Blatt and C. F. Roos, Science **334**, 57 (2011).

[26] V. Bouchiat, D. Vion, P. Joyez, D. Esteve, and M. H. Devoret, Phys. Scr. **1998**, 165 (1998).

[27] Y. Nakamura, Y. A. Pashkin, and J. S. Tsai, Nature **398**, 786 (1999).

[28] J. E. Mooij, T. P. Orlando, L. Levitov, L. Tian, C. H. van der Wal, and S. Lloyd, Science **285**, 1036 (1999).

[29] J. M. Martinis, S. Nam, J. Aumentado, and C. Urbina, Phys. Rev. Lett. **89**, 117901 (2002).

[30] J. Koch, T. M. Yu, J. Gambetta, A. A. Houck, D. I. Schuster, J. Majer, A. Blais, M. H. Devoret, S. M. Girvin, and R. J. Schoelkopf, Phys. Rev. A **76**, 042319 (2007).

[31] A. Wallraff, D. I. Schuster, A. Blais, L. Frunzio, R.-S. Huang, J. Majer, S. Kumar, S. M. Girvin, and R. J. Schoelkopf, Nature **431**, 162 (2004).

[32] A. Blais, R. S. Huang, A. Wallraff, S. M. Girvin, and R. J. Schoelkopf, Phys. Rev. A **69**, 062320 (2004).

[33] R. Barends, L. Lamata, J. Kelly, L. García-Álvarez, A. G. Fowler, A. Megrant, E. Jeffrey, T. C. White, D. Sank, J. Y. Mutus, et al., e-print arXiv:1501.07836 (2015).

[34] M. H. Devoret and R. Schoelkopf, Science **339**, 1169 (2013).

[35] M. P. A. Fisher, P. B. Weichman, G. Grinstein, and D. S. Fisher, Phys. Rev. B **40**, 546 (1989).

[36] I. M. Georgescu, S. Ashab, and F. Nori, Rev. Mod. Phys. **86**, 154 (2014).

[37] M. Greiner, O. Mandel, T. Esslinger, T. W. Hänsch, and I. Bloch, Nature **415**, 39 (2002).

[38] I. Bloch, J. Dalibard, and W. Zwerger, Rev. Mod. Phys. **80**, 885 (2008).

[39] S. Trotzky, Y.-A. Chen, A. Flesch, I. P. McCulloch, U. Schollwöck, J. Eisert, and I. Bloch, Nat. Phys. **8**, 325 (2012).

[40] M. Suzuki, Phys. Lett. A **146**, 319 (1990).

[41] H. F. Trotter, Proc. Am. Math. Soc. **10**, 545 (1959).

[42] A. Daskin and S. Kais, J. Chem. Phys. **134**, 144112 (2011).

[43] Y. Salathé, M. Mondal, M. Oppliger, J. Heinsoo, P. Kurpiers, A. Potoĉnik, A. Mezzacapo, U. Las Heras, L. Lamata, E. Solano, S. Filipp, and A. Wallraff, e-print arXiv:1502.06778 (2015).

[44] A. Mezzacapo, J. Casanova, L. Lamata, and E. Solano, New J. Phys. **15**, 033005 (2012).

[45] C. Nayak, S. H. Simon, A. Stern, M. Freedman, and S. D. Sarma, Rev. Mod. Phys. **80**, 1083 (2008).

[46] A. Y. Kitaev, Physics-Uspekhi **44**, 131 (2001).

[47] J. Alicea, Y. Oreg, G. Refael, F. von Oppen, and M. P. A. Fisher, Nature Phys. p. 412 (2011).

[48] R. M. L. J. D. Sau and S. D. Sarma, Phys. Rev. Lett. **105**, 077001 (2010).

[49] Y. Oreg, G. Refael, and F. von Oppen, Phys. Rev. Lett. **105**, 177002 (2010).

[50] L. Jiang, T. Kitagawa, J. Alicea, A. R. Akhmerov, D. Pekker, G. Refael, J. I. Cirac, E. Demler, M. D. Lukin, and P. Zoller, Phys. Rev. Lett. **106**, 220402 (2011).

[51] S. Diehl, E. Rico, M. A. Baranov, and P. Zoller, Nature Phys. **7**, 971 (2011).

[52] V. Mourik, K. Zuo, S. M. Frolov, S. R. Plissard, E. P. A. M. Bakkers, and L. P. Kouwenhoven, Science **336**, 1003 (2012).

[53] D. Porras and J. I. Cirac, Phys. Rev. Lett. **92**, 207901 (2004).

[54] A. Friedenauer, H. Schmitz, J. T. Glueckert, D. Porras, and T. Schätz, Nat. Phys. **4**, 757 (2008).

[55] J. Welzel, A. Bautista-Salvador, C. Abarbanel, V. Wineman-Fisher, C. Wunderlich, R. Folman, and F. Schmidt-Kaler, Eur. Phys. J. D **65**, 285 (2011).

[56] J. T. Barreiro, M. Müller, P. Schindler, D. Nigg, T. Monz, M. Chwalla, M. Hennrich, C. F. Roos, P. Zoller, and R. Blatt, Nature **470**, 486 (2011).

[57] J. Casanova, L. Lamata, I. L. Egusquiza, R. Gerritsma, C. F. Roos, J. J. García-Ripoll, and E. Solano, Phys. Rev. Lett. **107**, 260501 (2011).

[58] J. Casanova, L. Lamata, I. L. Egusquiza, R. Gerritsma, C. F. Roos, J. J. García-Ripoll, and E. Solano, Phys. Rev. Lett. **107**, 260501 (2011).

[59] S. P. Jordan, K. S. M. Lee, and J. Preskill, Science **336**, 1130 (2011).

[60] J. Casanova, A. Mezzacapo, L. Lamata, and E. Solano, Phys. Rev. Lett. **108**, 190502 (2012).

[61] R. Schmied, J. H. Wesenberg, and D. Leibfried, New J. Phys. **13**, 115011 (2011).

[62] P. Milman, W. Maineult, S. Guibal, L. Guidoni, B. Douçot, L. Ioffe, and T. Coudreau, Phys. Rev. Lett. **99**, 020503 (2007).

[63] P. Jordan and E. Wigner, Z. Phys. **47**, 631 (1928).

[64] A. Kitaev and C. Laumann, e-print arXiv:0904.2771 (2009).

[65] K. Kim, M.-S. Chang, R. Islam, S. Korenblit, L.-M. Duan, and C. Monroe, Phys. Rev. Lett **103**, 120502 (2009).

[66] E. Farhi, J. Goldstone, S. Gutmann, and M. Sipser, e-print arXiv:quant-ph/0001106 (2000).

[67] M. Tavis and F. W. Cummings, Phys. Rev. **170**, 379 (1968).

[68] R. Schmied, J. H. Wesenberg, and D. Leibfried, Phys. Rev. Lett. **102**, 233002 (2009).

[69] L. Lamata, D. R. Leibrandt, I. L. Chuang, J. I. Cirac, M. D. Lukin, V. Vuletić, and S. F. Yelin, Phys. Rev. Lett. **107**, 030501 (2011).

[70] M. Müller, K. Hammerer, Y. L. Zhou, C. F. Roos, and P. Zoller, New. J. Phys. **13**, 085007 (2011).

[71] A. Mezzacapo, J. Casanova, L. Lamata, and E. Solano, Phys. Rev. Lett. **109**, 200501 (2012).

[72] D. S. Abrams and S. Lloyd, Phys. Rev. Lett. **79**, 2586 (1997).

[73] M. Troyer and U. J. Wiese, Phys. Rev. Lett. **94**, 170201 (2005).

[74] E. Y. L. Jr, J. E. Gubernatis, R. T. Scalettar, S. R. White, D. J. Scalapino, and R. L. Sugar, Phys. Rev. B **41**, 9301 (1990).

[75] A. C. Hewson, *The Kondo Problem to Heavy Fermions* (Cambridge University Press, Cambridge, U.K., 1997).

[76] R. C. Albers, N. E. Christensen, and A. Svane, J. Phys. Condens. Matter **21**, 343201 (2009).

[77] G. D. Mahan, *Many Particle Physics* (Springer, New York, 2000).

[78] F. Schwabl, *Advanced Quantum Mechanics* (Springer, New York, 2005).

[79] M. A. Nielsen and I. L. Chuang, *Quantum Computation and Quantum Information* (Cambridge University Press, Cambridge, U.K., 2000).

[80] D. W. Berry, G. Ahokas, R. Cleve, , and B. C. Sanders, Commun. Math. Phys. **270**, 359 (2006).

[81] F. Verstraete and J. I. Cirac, J. Stat. Mech. **P09012** (2005).

[82] J. Kondo, Prog. Theor. Phys. **32**, 37 (1964).

[83] G. L. Goodvin, A. S. Mishchenko, and M. Berciu, Phys. Rev. Lett. **107**, 076403 (2003).

[84] R. Blatt (private communication).

[85] R. Gerritsma, G. Kirchmair, F. Zähringer, E. Solano, R. Blatt, and C. F. Roos, Nature **463**, 68 (2010).

[86] M. Suzuki, Proc. Japan Acad. B **69**, 161 (1993).

[87] M. Suzuki, Phys. Lett. **146**, 319 (1990).

[88] M. Suzuki, J. Math. Phys. **32**, 400 (1991).

[89] Alexandrov, *Polarons in advanced materials* (Springer, 2007).

[90] O. Gunnarsson, Rev. Mod. Phys. **69**, 575 (1997).

[91] A. Lanzara, P. V. Bogdanov, X. J. Zhou, S. A. Kellar, D. L. Feng, E. D. Lu, T. Yoshida, H. Eisaki, A. Fujimori, K. Kishio, et al., Nature **412**, 510 (2001).

[92] N. Bulut and D. J. Scalapino, Phys. Rev. B **54**, 14971 (1996).

[93] A. H. Romero, D. W. Brown, and K. Lindenberg, Phys. Rev. B **60**, 4618 (1999).

[94] T. Holstein, Ann. Phys. **8**, 325 (1959).

[95] H. Fehske, G. Wellein, and A. R. Bishop, Phys. Rev. B **83**, 075104 (2011).

[96] S. Longhi and G. D. Valle, Phys. Rev. B **84**, 155101 (2011).

[97] I. Lang and Y. A. Firsov, Sov. Phys. - JETP **16**, 1301 (1963).

[98] L.-C. Ku, S. A. Trugman, and J. Bona, Phys. Rev. B **65**, 174306 (2002).

[99] E. Jané, G. Vidal, W. Dür, P. Zoller, and J. I. Cirac, Quant. Inf. and Comp. **3**, 15 (2003).

[100] H. Weimer, M. Müller, I. Lesanovsky, P. Zoller, and H. P. Büchler, Nature Phys. **6**, 382 (2010).

[101] M. Johanning, A. F. Varón, and C. Wunderlich, J. Phys. B **42**, 154009 (2009).

[102] D. James, Appl. Phys. B **66**, 181 (1998).

[103] P. A. M. Dirac, Proceedings of the Royal Society A: Mathematical, Physical and Engineering Sciences **123**, 714 (1929).

[104] P. J. Love, Advances in Chem. Phys. **154**, 39 (2012).

[105] M. Head-London and E. Artacho, Physics Today **61**, 58 (2008).

[106] I. Kassal, J. D. Whitfield, A. Perdomo-Ortiz, M. H. Yung, and A. ASpuru-Guzik, Ann. Re. Phys. Chem. **62**, 185 (2011).

[107] M. H. Yung, J. D. Whitfield, S. Boixo, D. G. Tempel, and A. Aspuru-Guzik, Advances in Chem. Phys. **154**, 67 (2014).

[108] D. Abrams and S. Lloyd, Phys. Rev. Lett. **83**, 5162 (1999).

[109] A. Aspuru-Guzik, A. D. Dutoi, P. J. Love, and M. Head-Gordon, Science **309**, 1704 (2005).

[110] D. Poulin and P. Wocjan, Phys. Rev. Lett. **102**, 130503 (2009).

[111] B. P. Lanyon, J. D. Whitfield, G. G. Gillett, M. E. Goggin, M. P. Almeida, I. Kassal, J. D. Biamonte, M. Mohseni, B. J. Powell, M. Barbieri, et al., Nat. Chem. **2**, 106 (2010).

[112] Z. Li, Z. Li, M. H. Yung, H. Chen, D. Lu, J. D. Whitfield, X. Peng, A. Aspuru-Guzik, and J. Du, Sci. Rep. **1**, 88 (2011).

[113] J. S. Xu, M. H. Yung, X. Xu, S. Boixo, Z. W. Zhou, C. F. Li, A. Aspuru-Guzik, and G. C. Guo, Nat. Phot. **8**, 113 (2014).

[114] L. A. Wu, M. Byrd, and D. Lidar, Phys. Rev. Lett. **89**, 057904 (2002).

[115] I. Kassal, S. P. Jordan, P. J. Love, M. Mohseni, and A. Aspuru-Guzik, PNAS **105**, 18681 (2008).

[116] P. Wocjan, C. F. Chiang, D. Nagaj, and A. Abeyesinghe, Phys. Rev. A **80**, 022340 (2009).

[117] A. G. Taube and R. J. Bartlett, Int. J. Quant. Chem. **106**, 3393 (2006).

[118] A. Leggett, S. Chakravarty, A. T. Dorsey, M. P. A. Fisher, A. Garg, and W. Zwerger, Rev. Mod. Phys. **59**, 1 (1987).

[119] G. Ortiz, J. Gubernatis, E. Knill, and R. Laflamme, Phys. Rev. A **64**, 022319 (2001).

[120] A. Peruzzo, J. McClean, P. Shadbolt, M. H. Yung, X. Q. Zhou, P. J. Love, A. Aspuru-Guzik, and J. L. O'Brien, Nat. Comm. **5**, 4213 (2013).

[121] P. Kaye, R. Laflamme, and M. Mosca, *An Introduction to Quantum Computing* (Oxford University Press, USA, 2007).

[122] A. Fedorov, L. Steffen, M. Baur, M. P. da Silva, and A. Wallraff, Nature **481**, 170 (2012).

[123] A. A. Abdumalikov, J. M. Fink, K. Juliusson, M. Perchal, S. Berger, A. Wallraff, and S. Filipp, Nature **496**, 482 (2013).

[124] S. Chen, L. Wang, S.-J. Gu, , and Y. Wang, Phys. Rev. E **76**, 061108 (2007).

[125] L. F. Santos, F. Borgonovi, , and F. M. Izrailev, Phys. Rev. Lett. **108**, 094102 (2012).

[126] P. W. Anderson, Science **235**, 1196 (1987)).

[127] C. Rigetti, J. M. Gambetta, S. Poletto, B. L. T. Plourde, J. M. Chow, A. D. Córcoles, J. A. Smolin, S. T. Merkel, J. R. Rozen, G. A. Keefe, et al., Phys. Rev. B **86**, 100506(R) (2012).

[128] K. Kim, M.-S. Chang, S. Korenblit, R. Islam, E. E. Edwards, J. K. Freericks, G.-D. Lin, L.-M. Duan, and C. Monroe, Nature (London) **465**, 590 (2010).

[129] M. D. Reed, L. DiCarlo, S. E. Nigg, L. Sun, L. Frunzio, S. M. Girvin, and R. J. Schoelkopf, Nature **482**, 382 (2012).

[130] U. L. Heras, A. Mezzacapo, L. Lamata, S. Filipp, A. Wallraff, and E. Solano, Phys. Rev. Lett. **112**, 200501 (2014).

[131] A. Mezzacapo, U. L. Heras, J. S. Pedernales, L. DiCarlo, E. Solano, and L. Lamata, Sci. Rep. **4**, 7482 (2014).

[132] L. S. Bishop, L. Tornberg, D. Price, E. Ginossar, A. Nunnenkamp, A. A. Houck, J. M. Gambetta, J. Koch, G. Johansson, S. M. Girvin, et al., New J. Phys. **11**, 073040 (2009).

[133] M. Neeley, R. C. Bialczak, M. Lenander, E. Lucero, M. Mariantoni, A. D. OConnell, D. Sank, H. Wang, M. Weides, J. Wenner, et al., Nature **467**, 570 (2010).

[134] L. DiCarlo, M. D. Reed, L. Sun, B. R. Johnson, J. M. Chow, J. M. Gambetta, L. Frunzio, S. M. Girvin, M. H. Devoret, and R. J. Schoelkopf, Nature **467**, 574 (2010).

[135] T. Monz, P. Schindler, J. T. Barreiro, M. Chwalla, D. Nigg, W. A. Coish, M. Harlander, W. Hänsel, M. Hennrich, and R. Blatt, Phys. Rev. Lett. **106**, 130506 (2011).

[136] A. Wallraff, D. I. Schuster, A. Blais, J. M. Gambetta, J. Schreier, L. Frunzio, M. H. Devoret, S. M. Girvin, and R. J. Schoelkopf, Phys. Rev. Lett. **99**, 050501 (2007).

[137] P. J. Leek, S. Filipp, P. Maurer, M. Baur, R. Bianchetti, J. M. Fink, M. Göppl, L. Steffen, and A. Wallraff, Phys. Rev. B **79**, 180511(R) (2009).

[138] J. D. Strand, M. Ware, F. Beaudoin, T. A. Ohki, B. R. Johnson, A. Blais, and B. L. T. Plourde, Phys. Rev. B **87**, 220505(R) (2013).

[139] S. E. Nigg and S. M. Girvin, Phys. Rev. Lett. **110**, 243604 (2013).

[140] A. Y. Kitaev, Ann. Phys. **303**, 2 (2003).

[141] J. M. Gambetta, A. A. Houck, and A. Blais, Phys. Rev. Lett. **106**, 030502 (2011).

[142] S. J. Srinivasan, A. J. Hoffman, J. M. Gambetta, and A. A. Houck, Phys. Rev. Lett. **106**, 083601 (2011).

[143] I. I. Rabi, Phys. Rev. **49**, 324 (1936).

[144] R. H. Dicke, Phys. Rev. **93**, 99 (1954).

[145] E. T. Jaynes and F. W. Cummings, Proc. IEEE **51**, 89 (1963).

[146] M. Tavis and F. W. Cummings, Phys. Rev. **170**, 379 (1968).

[147] D. Braak, Phys. Rev. Lett. **107**, 100401 (2011).

[148] D. Braak, J. Phys. B **46**, 224007 (2013).

[149] A. Günter, A. A. Anappara, J. Hees, A. Sell, G. Biasiol, L. Sorba, S. D. Liberato, C. Ciuti, A. Tredicucci, A. Leitenstorfer, et al., Nature **458**, 178 (2009).

[150] T. Niemczyk, F. Deppe, H. Huebl, E. P. Menzel, F. Hocke, M. J. Schwarz, J. J. García-Ripoll, D. Zueco, T. Hümmer, E. Solano, et al., Nat. Phys. **6**, 772 (2010).

[151] P. Forn-Diaz, J. Lisenfeld, D. Marcos, J. J. Garcia-Ripoll, E. Solano, C. J. P. M. Harmans, and J. E. Mooij, Phys. Rev. Lett. **105**, 237001 (2010).

[152] J. Casanova, G. Romero, I. Lizuain, J. J. García-Ripoll, and E. Solano, Phys. Rev. Lett **105**, 263206 (2010).

[153] K. Hepp and E. H. Lieb, Ann. Phys. NY **76**, 360 (1973).

[154] Y. K. Wang and F. T. Hioe, Phys. Rev. A **7**, 831 (1973).

[155] H. J. Carmichael, C. W. Gardiner, and D. F. Walls, Phys. Lett. A **46**, 47 (1973).

[156] A. Majda, P. Kramer, R. Bird, W. Stewart, and E. Lightfoot, *Transport Phenomena, 2nd edition* (John Wiley, New York, 2002).

[157] A. Majda and P. Kramer, Phys. Rep. **314**, 237 (1999).

[158] S. Succi, O. Filippova, G. Smith, and E. Kaxiras, Comput. Sci. Eng. **3**, 26 (2001).

[159] R. Benzi, S. Succi, and M. Vergassola, Phys. Rep. **222**, 145 (1992).

[160] C. K. Aidun and J. R. Clauser, Annual Review of Fluid Mechanics **42**, 439 (2010).

[161] S. Succi, Europ. Phys. J. B **64**, 471 (2008).

[162] M. Mendoza, B. M. Boghosian, H. J. Herrmann, and S. Succi, Phys. Rev. Lett. **105**, 104502 (2010).

[163] B. P. Lanyon, M. Zwerger, P. Jurcevic, C. Hempel, W. Dür, H. J. Briegel, R. Blatt, and C. F. Roos, Phys. Rev. Lett. **112**, 100403 (2014).

[164] D. Nigg, M. Müller, E. A. Martinez, P. Schindler, M. Hennrich, T. Monz, M. A. Martin-Delgado, and R. Blatt, Science **345**, 302 (2014).

[165] P. Hauke, D. Marcos, M. Dalmonte, and P. Zoller, Phys. Rev. X **3**, 041018 (2013).

[166] L. Steffen, Y. Salathe, M. Oppliger, P. Kurpiers, M. Baur, C. Lang, C. Eichler, G. Puebla-Hellmann, A. Fedorov, and A. Wallraff, Nature **500**, 319 (2013).

[167] P. Roushan, C. Neill, Y. Chen, M. Kolodrubetz, C. Quintana, N. Leung, M. Fang, R. Barends, B. Campbell, Z. Chen, et al., Nature **515**, 241 (2014).

[168] J. Yepez, Phys. Rev. E **63**, 046702 (2001).

[169] M. A. Pravia, Z. Chen, J. Yepez, and D. G. Cory, Quant. Inf. Process. **2**, 97 (2003).

[170] H. Qian, D. d'Humieres, and P. Lallemand, Europhys. Lett. **17**, 479 (1992).

[171] S. Succi and R. Benzi, Physica D **69**, 327 (1993).

[172] F. Fillion-Gourdeau, H. J. Herrmann, M. Mendoza, S. Palpacelli, and S. Succi, Phys. Rev. Lett. **111**, 160602 (2013).

[173] A. M. Childs and N. Wiebe, Quant. Inf. and Comp. **12**, 901 (2012).

[174] F. Dreisow, M. Heinrich, R. Keil, A. Tünnermann, S. Nolte, S. Longhi, and A. Szameit, Phys. Rev. Lett. **105**, 143902 (2010).

[175] T. Salger, C. Grossert, S. Kling, and M. Weitz, Phys. Rev. Lett. **107**, 240401 (2011).

[176] S. K. Leyton and T. J. Osborne, e-print arXiv:0812.4423 (2008).

[177] M. Ringbauer, M. A. Broome, C. R. Myers, A. G. White, and T. C. Ralph, Nat. Comm. **5**, 4145 (2014).

[178] M. H. Yung, J. Casanova, A. Mezzacapo, J. McClean, L. Lamata, A. Aspuru-Guzik, and E. Solano, Sci. Rep. **4**, 3589 (2014).

[179] A. Mezzacapo, L. Lamata, S. Filipp, and E. Solano, Phys. Rev. Lett. **113**, 050501 (2014).

[180] A. Mezzacapo, M. Sanz, L. Lamata, I. L. Egusquiza, S. Succi, and E. Solano, e-print arXiv:1502.00515 (2015).

[181] I. Area, D. K. Dimitrov, E. Godoy, and A. Ronveaux, Math. Comp. **73**, 1937 (2004).